Search for the Standard Model Higgs Boson in the $WH \rightarrow \ell\nu b\bar{b}$ Channel in 1.96-TeV Proton-Antiproton Collisions

Yoshikazu NAGAI

February 2010

Search for the Standard Model Higgs Boson in the $WH \rightarrow \ell\nu b\bar{b}$ Channel in 1.96-TeV Proton-Antiproton Collisions

Yoshikazu NAGAI
(Doctoral Program in Physics)

Submitted to the Graduate School of Pure and Applied Sciences in Partial Fulfillment of the Requirements for the Degree of Doctor of Philosophy in Science

at the
University of Tsukuba

Abstract

We have searched for the Standard Model Higgs boson in the $WH \rightarrow \ell\nu b\bar{b}$ channel in 1.96 TeV $p\bar{p}$ collisions at CDF. This search is based on the data collected by March 2009, corresponding to an integrated luminosity of 4.3 fb^{-1}. The WH channel is one of the most promising channels for the Higgs boson search at Tevatron in the low Higgs boson mass region, where the Higgs boson predominantly decays into $b\bar{b}$ ($m_H < 135\ \mathrm{GeV}/c^2$).

Experimentally we select events with a high-p_T lepton, large missing transverse energy and two b-quark jets. This signature is the same as for the W + jets background which has a huge cross section. To reduce the W + jets background, we apply b-jet identification algorithms to jets and require at least one b-tagged jet.

After selecting the events, we employ sophisticated techniques to further improve the analysis sensitivity. One technique is the Neural Network jet energy correction which is developed to improve the invariant mass resolution of the di-jet system, the most powerful kinematics to separate the signal from background. Another technique is Bayesian Neural Network (BNN) discriminant technique which distinguishes the signal events from the residual backgrounds.

Since we do not observe any significant excess of events in the data compared to both the Standard Model background expectation and the BNN output distributions, we set a 95% confidence level upper limit on the WH production cross section times the branching ratio of the Higgs decaying into a $b\bar{b}$ pair. The observed (expected) upper limit ranges 3.98 (2.78) to 37.6 (33.7) times the Standard Model expectation for Higgs boson masses spanning from 100 to 150 GeV/c^2.

Acknowledgments

I would like to express my gratefulness to all people who supported and encouraged me during the course of my Ph.D programs.

First of all, I would like to thank my adviser, Prof. Shinhong Kim. He gave me a chance to study high energy physics at the Fermilab and gave me a constructive advice on my studies.

I would also like to thank all the members of the WH groups. I would like to thank the leader of the WH analysis group, Prof. Weiming Yao. He always encouraged me with very useful comments. I learnt many things from him. I would also like to thank other WH analysis group members, Prof. Jay Dittmann, Dr. Nils Krumnack, Dr. Benjamin Kilminster, Prof. Anyes Taffard, Prof. Andreas Warburton, Prof. Richard Hughes, Prof. Kevin Lannon, Prof. Brian Winer, Dr. Homer Wolfe, Prof. Evelyn Thomson, and Prof. Christopher Neu. They helped my WH analysis progress through very useful advices and discussions. I also thank you to the members of $WHME$ group. I could polish this NN analysis through the discussion with them. I would like to thank Jason Slaunwhite, Martin Frank, Timo Aaltonen, Adrian Buzatu, and Justin Keung. I enjoyed discussion with them and was impressive their attitude toward high energy physics. They encouraged me many times.

I would like to thank CDF-Japan group staff members, Prof. Fumihiko Ukegawa, Prof. Kazuhiko Hara, Prof. Yuji Takeuchi, Prof. Koji Sato, Dr. Tomonobu Tomura, Dr. Hideki Miyake, Dr. Masakazu Kurata, and Dr. Junji Naganoma. They gave me useful advices and I could polish up this study. And, I would also like to thank to Fermilab colleagues and friends, Dr. Masato Aoki, Dr. Yuji Enari, Dr. Koji Nakamura, Dr. Takayuki Wakisaka, and Atsunari Hamaguchi. I shared good times at the Fermilab with them.

Finally, I would like to thank my parents. They supported me everytime. I can not thank you enough.

Contents

List of Figures

List of Tables

Chapter 1

Introduction

$$What\,is\,this\,world\,made\,of?$$

The ancient Greeks considered the world to be made from the four fundamental elements: earth, air, fire, and water. Then, the effort to answer this question is changed to find the elementary particle, which is the smallest indivisible particle of matter. Historically, the whole atoms (such as a hydrogen atom) or the hadrons (such as a proton and neutron) were regarded as elementary particles. Over the centuries, our knowledge has advanced and we now know they have substructure.

Our current best knowledge on elementary particles is given by a theoretical framework called the "Standard Model". The Standard Model of particle physics is a description of the fundamental particles, the quarks and leptons, and the forces between them. It also describes the origin of mass through the Higgs mechanism, which predicts the existence of the Higgs boson, the last undetected particle in the Standard Model.

This thesis presents a search for Higgs boson production in proton-antiproton collisions using the $WH \rightarrow \ell\nu b\bar{b}$ channel. This chapter describes a short summary of the Standard Model, the Higgs mechanism, and the current constraint on the Higgs boson. Chapter 2 describes the experimental apparatus, the Tevatron and the Collider Detector at Fermilab (CDF). In chapter 3, the event reconstruction from the detector information is discussed. Chapter 4 presents the event selection to select the $WH \rightarrow \ell\nu b\bar{b}$ candidate events. Chapter 5 presents the background modeling and discusses their estimation. Chapter 6 introduces the advanced techniques to further improve the analysis sensitivity. Chapter 7 discusses the signal acceptance and its systematic uncertainty. Then, chapter 8 describes the final results of this analysis and the latest results of the Higgs boson searches at the Tevatron. An alternative approach, which is to seek a dynamical mechanism for the symmetry breaking instead of the Higgs mechanism known as "technicolor", is discussed in appendix A.

1.1 The Standard Model

The Standard Model is a quantum field theory that is based on the gauge symmetry group:

$$SU(3)_C \otimes SU(2)_L \otimes U(1)_Y \tag{1.1}$$

where $SU(3)_C$ represents the symmetry group of the strong interactions of quantum chromodynamics (QCD) [1, 2], $SU(2)_L \otimes U(1)_Y$ represents the symmetry group of the electroweak interactions. A subgroup of $SU(2)_L \otimes U(1)_Y$ is a unified group of the weak and electromagnetic interaction, proposed by Glashow, Salam and Weinberg [3–5].

1.1.1 Fundamental Particles

There are two types of particles: spin $s = \frac{1}{2}$ fermions which are the constituents of normal matter, and spin $s = 1$ bosons which mediate the force between fermions.

Fermions

Spin $s = \frac{1}{2}$ fermions are classified into quarks and leptons. There are six types of quarks: up (u), down (d), charm (c), strange (s), top (t), and bottom (b). Similarly, there are six types of leptons: electron (e), muon (μ), tau (τ), and their respective neutrinos (ν_e, ν_μ, ν_τ).

These fermions are classified into the three generations of left-handed and right-handed quarks and leptons. The left-handed fermions are in weak isospin doublets, while the right-handed fermions are in weak isospin singlets:

1st generation: $L_e = \begin{pmatrix} \nu_e \\ e^- \end{pmatrix}_L,\ R_e = e^-_R,\ L_q^{(1)} = \begin{pmatrix} u \\ d' \end{pmatrix}_L,\ R_u^{(1)} = u_R,\ R_d^{(1)} = d_R$

2nd generation: $L_\mu = \begin{pmatrix} \nu_\mu \\ \mu^- \end{pmatrix}_L,\ R_\mu = \mu^-_R,\ L_q^{(2)} = \begin{pmatrix} c \\ s' \end{pmatrix}_L,\ R_u^{(2)} = c_R,\ R_d^{(2)} = s_R$

3rd generation: $L_\tau = \begin{pmatrix} \nu_\tau \\ \tau^- \end{pmatrix}_L,\ R_\tau = \tau^-_R,\ L_q^{(3)} = \begin{pmatrix} t \\ b' \end{pmatrix}_L,\ R_u^{(3)} = t_R,\ R_d^{(3)} = b_R$

These fermions are characterized with weak isospin (I) and weak hypercharge (Y) through the relation $Q = I_3 + \frac{1}{2}Y$, where Q is the electric charge. The mass eigenstates of the left-handed down-type quarks (d', s', b') are related to flavor eigenstates (d, s, b) through the Cabibbo-Kobayashi-Maskawa matrix [6, 7]:

$$\begin{pmatrix} d' \\ s' \\ b' \end{pmatrix} = \begin{pmatrix} V_{ud} & V_{us} & V_{ub} \\ V_{cd} & V_{cs} & V_{cb} \\ V_{td} & V_{ts} & V_{tb} \end{pmatrix} \begin{pmatrix} d \\ s \\ b \end{pmatrix} \tag{1.2}$$

The fundamental properties of fermions are summarized in Table 1.1.

Quarks have an additional quantum number called color charge, which is three types (r, g, and b). Color charge is not seen in nature and therefore the colorless composite particles can only exist. The colorless composite particles can be made with two ways: bound state of three quarks called baryons such as a proton ($u_r u_g d_b$), or bound state of one quark and one antiquark called mesons such as a pion ($u_r \bar{d}_r$).

Bosons

The interaction between fermions is mediated by $s = 1$ bosons. The photon (γ), $W^\pm$, and Z carry the electroweak force, and the gluons (g) carry the strong force. The photon is massless, while the $W^\pm$, and Z are massive particles. In the Standard Model, the $W^\pm$, and Z acquire the mass as a result of the electroweak symmetry breaking through the Higgs mechanism which is discussed in Section 1.1.3. The gluon is the massless bi-colored particle and influences only quarks. The properties of bosons are summarized in Table 1.2.

	Particle	Electric charge Q	Hyper charge Y	Mass
Quarks	u_L	+2/3	1/3	1.5–3.3 MeV/c^2
	u_R		4/3	
	d_L	−1/3	1/3	3.5–6.0 MeV/c^2
	d_R		−2/3	
	c_L	+2/3	1/3	1.27±0.02 GeV/c^2
	c_R		4/3	
	s_L	−1/3	1/3	70–130 MeV/c^2
	s_R		−2/3	
	t_L	+2/3	1/3	173.1±1.3 GeV/c^2
	t_R		4/3	
	b_L	−1/3	1/3	4.20±0.03 GeV/c^2
	b_R		−2/3	
Leptons	ν_e	0	−1	< 2 eV/c^2
	e_L	−1	−1	0.511 MeV/c^2
	e_R		−2	
	ν_μ	0	−1	< 0.19 MeV/c^2
	μ_L	−1	−1	106 MeV/c^2
	μ_R		−2	
	ν_τ	0	−1	< 18.2 MeV/c^2
	τ_L	−1	−1	1.78 GeV/c^2
	τ_R		−2	

Table 1.1: Fundamental properties of fermions.

Particle	Electric charge Q	Hyper charge Y	Mass
γ	0	0	0
W^- (W^+)	−1 (+1)	−1 (+1)	80.420 GeV/c^2
Z	0	0	91.188 GeV/c^2
g	0	0	0

Table 1.2: Fundamental properties of bosons.

1.1.2 Electroweak Interactions

The electroweak interaction of quarks and leptons is described by the $SU(2)_L \otimes U(1)_Y$ gauge group. In the electroweak sector, there are two fields: B_μ which corresponds to the generator Y of the $U(1)_Y$ group and W^i_μ which corresponds to the generator T_i ($i = 1, 2, 3$) of the $SU(2)_L$ group. These generator T_i are defined as

$$T_i = \frac{\sigma_i}{2},\ \sigma_1 = \begin{pmatrix} 0 & 1 \\ 1 & 0 \end{pmatrix},\ \sigma_2 = \begin{pmatrix} 0 & -i \\ i & 0 \end{pmatrix},\ \sigma_3 = \begin{pmatrix} 1 & 0 \\ 0 & -1 \end{pmatrix} \tag{1.3}$$

where σ_i is the 2×2 Pauli matrices. The commutation relations for the total group are:

$$[T_i, T_j] = i\epsilon_{ijk} T_k,\ [T_i, Y] = 0 \tag{1.4}$$

The Lagrangian of the electroweak interaction is summarized

$$\mathcal{L} = \mathcal{L}_{\text{gauge}} + \mathcal{L}_{\text{fermions}} \tag{1.5}$$

with

$$\mathcal{L}_{\text{gauge}} = -\frac{1}{4} W^i_{\mu\nu} W_i^{\mu\nu} - \frac{1}{4} B_{\mu\nu} B^{\mu\nu} \tag{1.6}$$

and

$$\mathcal{L}_{\text{fermions}} = \sum_{j=L,R} i\bar{\psi}_j \gamma^\mu D_{\mu,j} \psi_j \tag{1.7}$$

Here, the covariant derivative is

$$D_{\mu L}\psi_L = (\partial_\mu - igT_i W^i_\mu + i\frac{g'}{2} Y B_\mu)\psi_L,\ D_{\mu R}\psi_R = (\partial_\mu + i\frac{g'}{2} Y B_\mu)\psi_R \tag{1.8}$$

where g is the coupling constant corresponding to $SU(2)_L$, and g' is the coupling constant corresponding to $U(1)_Y$. $B_{\mu\nu}$ is given by

$$B_{\mu\nu} = \partial_\mu B_\nu - \partial_\nu B_\mu \tag{1.9}$$

and $W^i_{\mu\nu}$ is given by

$$W^i_{\mu\nu} = \partial_\mu W^i_\nu - \partial_\nu W^i_\mu - g\epsilon_{ijk} W^j_\mu W^k_\nu \tag{1.10}$$

This Lagrangian is invariant under the local $SU(2)_L \otimes U(1)_Y$ gauge transformations for fermion and gauge fields:

$$\begin{aligned}
\psi_L(x) &\rightarrow \psi'_L(x) = e^{iT^i\theta(x)} e^{i\frac{Y}{2}\phi(x)} \psi_L(x) \\
\psi_R(x) &\rightarrow \psi'_R(x) = e^{i\frac{Y}{2}\phi(x)} \psi_R(x) \\
B_\mu(x) &\rightarrow B_\mu(x) - \frac{1}{g'}\partial_\mu \phi(x) \\
\boldsymbol{W}_\mu(x) &\rightarrow \boldsymbol{W}_\mu(x) - \frac{1}{g}\partial_\mu \boldsymbol{\theta}(x) - \boldsymbol{\theta}(x) \times \boldsymbol{W}_\mu(x)
\end{aligned}$$

The physical gauge bosons observed experimentally are obtained from the electroweak interaction eigenstates by the following expressions,

$$\begin{aligned}
W^\pm_\mu &= \frac{1}{\sqrt{2}}(W^1_\mu \mp i W^2_\mu) \\
Z_\mu &= \cos\theta_W W^3_\mu - \sin\theta_W B_\mu \\
A_\mu &= \sin\theta_W W^3_\mu + \cos\theta_W B_\mu
\end{aligned} \tag{1.11}$$

where $W^\pm_\mu$, Z_μ, and A_μ represent the W bosons, Z boson, and the photon fields, respectively. The mixing angle θ_W is called the Weinberg angle [5].

1.1.3 Electroweak Symmetry Breaking and the Higgs Mechanism

The fermion and gauge fields described in Eq. 1.5 are still massless, so it is not matched to the experimental fact that the W and Z bosons are massive. If we add a mass term for the weak gauge boson such as $\frac{1}{2}M_W^2 W_\mu W^\mu$, the Lagrangian will not be invariant under the local $SU(2)_L \otimes U(1)_Y$ gauge transformations. Similarly, a fermion mass term $-m_f \bar{\psi}_f \psi_f$ is not invariant since the left-handed and right-handed fields transform differently such as:

$$-m_f \bar{\psi}_f \psi_f = -m_f \bar{\psi}_f \Big(\frac{1}{2}(1-\gamma^5) + \frac{1}{2}(1+\gamma^5)\Big)\psi_f = -m_f(\bar{\psi}_R \psi_L + \bar{\psi}_L \psi_R) \tag{1.12}$$

To give a mass to the weak gauge bosons and fermions, we can employ the same methodology as the Meissner effect[†], called the Higgs mechanism [8, 9]. The Higgs mechanism has been fully incorporated into the Standard Model and is responsible for the gauge bosons and fermions mass. This mechanism not only gives rise to particle masses, but also predicts a new spin 0 scalar boson, called the Higgs boson.

In order to give the weak gauge bosons mass, a scalar field ϕ (the Higgs field) and potential term is added into the Lagrangian Eq. 1.5 as:

$$\mathcal{L}_\phi = (D_\mu \phi(x))^\dagger (D^\mu \phi(x)) - V(\phi) \text{ with } V(\phi) = \mu^2 \phi^\dagger \phi + \lambda(\phi^\dagger \phi)^2 \tag{1.13}$$

where λ is a self coupling of the Higgs field, and ϕ is defined as

$$\phi = \begin{pmatrix} \phi^+ \\ \phi^0 \end{pmatrix} = \frac{1}{\sqrt{2}} \begin{pmatrix} \phi_1 + i\phi_2 \\ \phi_3 + i\phi_4 \end{pmatrix} \tag{1.14}$$

If $\mu^2 > 0$, the potential $V(\phi)$ is symmetric with its minimum at 0 (Figure 1.1, left). In this case, this describes the QED Lagrangian for a charged scalar particle of mass μ and ϕ_4 self-interactions. On the other hand, if $\mu^2 < 0$, the minimum of the potential $V(\phi)$ is given at non-zero point as shown in Figure 1.1 (right). Once one of the vacuum state is selected, the electroweak symmetry is spontaneously broken.

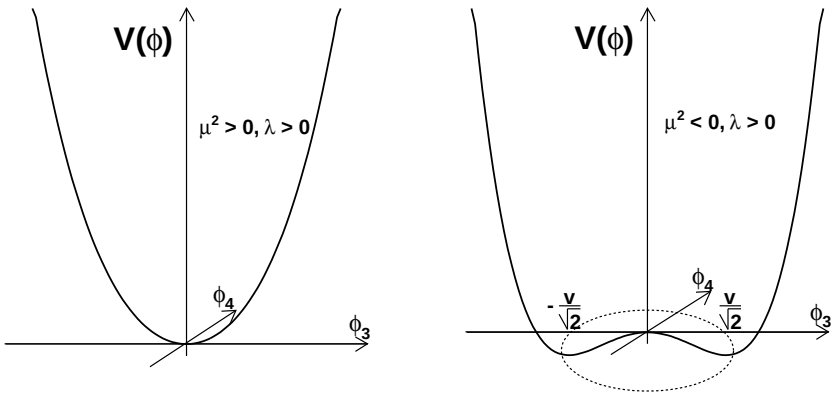

Figure 1.1: Potential $V(\phi)$ with $\mu^2 > 0$ and $\lambda > 0$ (left), and with $\mu^2 < 0$ and $\lambda > 0$ (right).

[†]The Meissner effect is the exclusion of a magnetic field from a superconductor during its transition, which corresponds to the photon acting as a non-zero mass particle.

Then, we expand the field around this vacuum state as:

$$\phi_3(x) = v + \eta_3(x),\ \phi_4 = \eta_4(x) \tag{1.15}$$

where η is the quantum fluctuation. The Lagrangian expresses the appearance of a neutral scalar boson, ϕ_3, and three massless Nambu-Goldstone bosons, ϕ_1, ϕ_2 and ϕ_4. These massless bosons are not expected in nature, but we can remove them by choosing proper gauge, called the unitary gauge. Here, we choose: $\phi_3 = v$, $\phi_1 = \phi_2 = \phi_4 = 0$. By choosing the unitary gauge, the weak gauge fields acquire the mass with the real scalar field:

$$\phi(x) = \frac{1}{\sqrt{2}} \begin{pmatrix} 0 \\ v + H(x) \end{pmatrix} \tag{1.16}$$

This mechanism is called the Higgs mechanism. The Lagrangian $\mathcal{L}_\phi$ (Eq. 1.13) becomes

$$\begin{aligned} \mathcal{L}_\phi &= \frac{1}{2}(\partial_\mu H)^2 + \frac{1}{4}g^2 W_\mu W^\mu (v+H)^2 \\ &+ \frac{1}{8}\left(v\sqrt{g^2+g'^2}\right)^2 Z_\mu Z^\mu (v+H)^2 - V\left(\frac{1}{2}(v+H)^2\right) \end{aligned} \tag{1.17}$$

The second and third terms of this Lagrangian can be identified as the W and Z bosons mass terms. Finally, the mass of the W and Z bosons are given by

$$m_W = \frac{1}{2}gv,\ m_Z = \frac{1}{2}v\sqrt{g^2+g'^2} \tag{1.18}$$

This Lagrangian also has a mass term coming from the potential V. It can be identified as the Higgs boson mass term. The Higgs boson mass is given by

$$m_H = \sqrt{2\lambda}v \tag{1.19}$$

1.1.4 Higgs Boson Production and Decay

The next-to-leading-order (NLO) Higgs boson production cross section at the Tevatron is shown in Figure 1.2. Gluon fusion Higgs boson production ($gg \to H$) has about 10 times larger cross section than production in association with a W boson (WH), and the cross section of WH process is about twice as much as ZH production.

The Higgs boson decay branching ratio is calculated by HDECAY [10], which can treat NLO effect, and shown in Figure 1.3. At the low mass region ($M_H < 135\ \mathrm{GeV}/c^2$), Higgs boson decay is dominated by $H \to b\bar{b}$, while $H \to W^+W^-$ decay mode is dominant at the high mass region ($M_H > 135\ \mathrm{GeV}/c^2$). At the low mass region, $gg \to H \to b\bar{b}$ is the predominant channel, however, this channel suffers from huge QCD multi-jet backgrounds. As a result, $WH \to \ell\nu b\bar{b}$ is one of the most sensitive channels for the low mass Higgs searches, since this process has a second largest cross section and can reduce QCD background by requiring a lepton. Our Standard Model Higgs boson search will focus on $WH \to \ell\nu b\bar{b}$. Figure 1.4 shows WH production and decay to a $\ell\nu b\bar{b}$ final state.

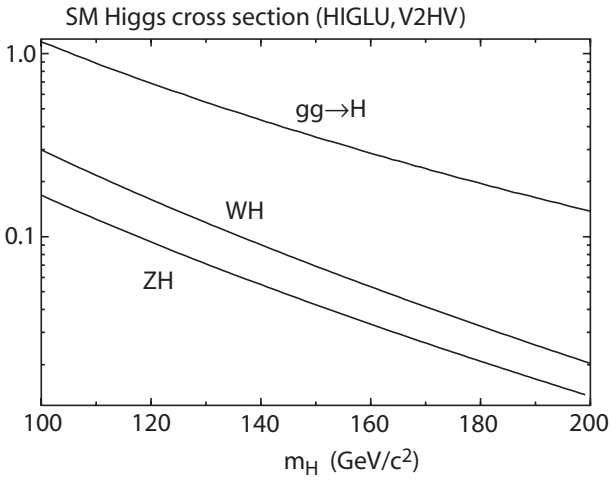

Figure 1.2: The NLO Higgs boson production cross section in pb at the Tevatron ($p\bar{p}$ collision at $\sqrt{s}$ =1.96 TeV).

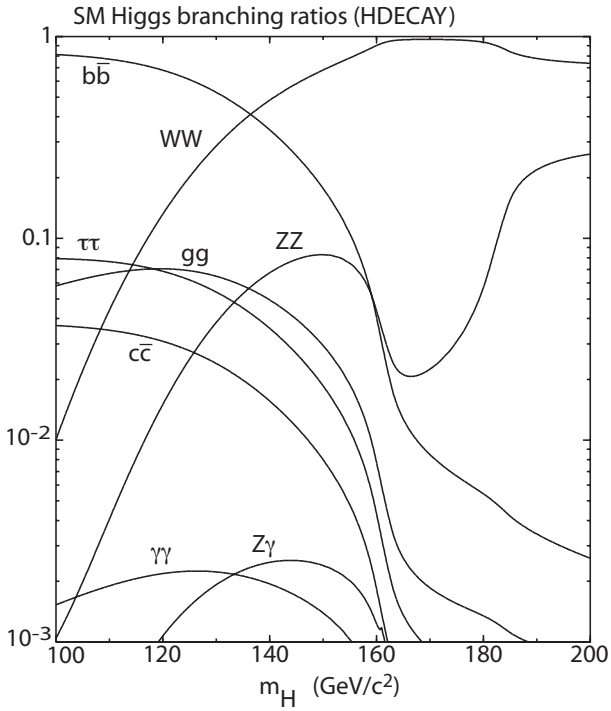

Figure 1.3: The branching ratio for each Higgs boson decay mode as a function of Higgs boson mass.

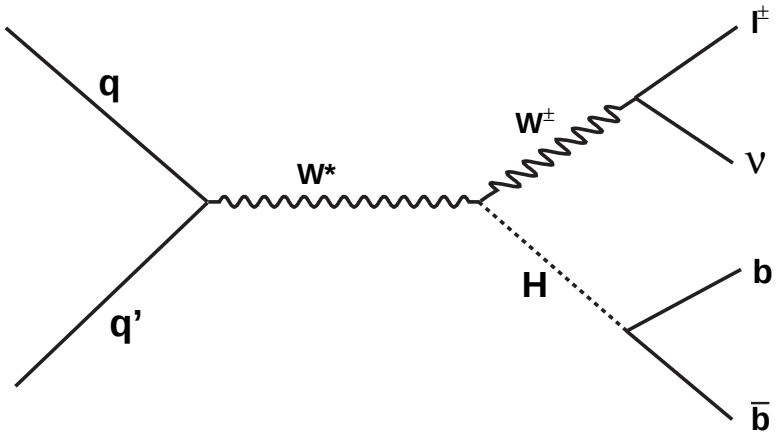

Figure 1.4: Feynman diagram of the $WH \rightarrow \ell\nu b\bar{b}$ channel.

1.2 Previous Higgs Boson Searches

1.2.1 Direct Searches

Searches at LEP

The experiments at the Large Electron Positron Collider (LEP) performed a search for the Standard Model Higgs boson in e^+e^- collisions at a center-of-mass energies of 189–209 GeV [11]. The main search channel at LEP is $e^+e^- \rightarrow ZH$ with $Z \rightarrow$ all and $H \rightarrow b\bar{b}$. Using the full data accumulated at four experiments (ALEPH, DELPHI, L3, and OPAL), the Higgs boson mass below 114.4 GeV/c^2 has been excluded at 95% confidence level (C.L.) (Figure 1.5).

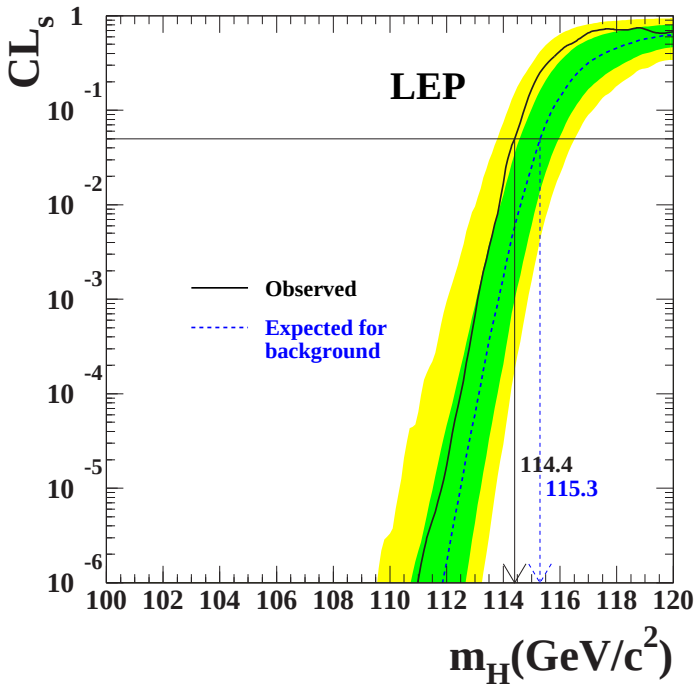

Figure 1.5: The ratio $CL_s = CL_{s+b}/CL_b$ for the signal plus background hypothesis as a function of the Higgs mass. Solid line: observed result; dashed line: median expectation. The green and yellow shaded bands around the median expected curve correspond to the 1σ and 2σ probability bands.

Searches at the Tevatron

The following searches are performed at the Tevatron:

1. The low mass Higgs boson searches (mainly $M_H < 135$ GeV/c^2) with $H \rightarrow b\bar{b}$, $\tau^+\tau^-$, or $\gamma\gamma$ decays.

   - $\ell^{\pm}\nu b\bar{b}$ channel: The Higgs boson is produced in association with a $W^{\pm}$ boson. This has a relatively large effective cross section. The final state includes a high-p_T lepton, large missing transverse energy, and two b-jets (CDF [12], D0 [13]).

- $\ell^+\ell^- b\bar{b}$ channel: The Higgs boson is produced in association with a Z boson. The final state includes two high-p_T leptons with the Z mass resonance, and two b-jets. This channel provides the cleanest signal among the low mass Higgs boson searches (CDF [14], D0 [15]).
- $\nu\nu b\bar{b}$ channel: The Higgs boson is produced in association with a $W^{\pm}$ or Z boson. The main acceptance of this channel comes from the $Z \to \nu\nu$ decay, but also comes from the case that a charged lepton is not detected in the $W \to \ell\nu$ decay (CDF [16], D0 [17]).
- $q\bar{q}b\bar{b}$ channel: The Higgs boson is produced in association with a $W^{\pm}$ or Z boson, or also produced through the weak vector boson fusion process. Due to the large branching fraction of W or $Z \to q\bar{q}$, this channel has the largest effective cross section among the low mass Higgs boson searches. However, it is one of the most difficult channels to analyze since the final state contains only jets and it suffers from the enormous QCD backgrounds (CDF [18]).
- $\tau^+\tau^-+$ jets channel: The Higgs boson is produced through three processes: gluon fusion, associated with a W or Z boson, or weak vector boson fusion. The lower branching fraction of $H \to \tau^+\tau^-$ can be recovered with using multiple production processes. (CDF [19], D0 [20]).
- $\gamma\gamma$ channel: The Higgs boson is produced through the gluon fusion process and decays into two photons. Due to the very small branching fraction of $H \to \gamma\gamma$, this channel has a very small effective cross section (D0 [21]).

2. The high mass Higgs boson searches (mainly $M_H > 135\ \mathrm{GeV}/c^2$) with $H \to W^+W^-$ decays.

   - $\ell^+\ell^-$ channel: The Higgs boson is mainly produced through the gluon fusion process. It is the most sensitive channel for the high mass Higgs boson searches (CDF [22], D0 [23]).
   - $W^{\pm}W^+W^-$ channel: The Higgs boson is produced in association with a $W^{\pm}$ boson. It is based on like-sign dilepton identification with very small background but also small effective cross section (CDF [24], D0 [25]).

Figure 1.6 shows the summary of the CDF combined 95% upper limit on the Higgs boson production cross section normalized to the Standard Model expectation. The contribution of each channel is also shown. Figure 1.7 shows the summary of the Tevatron combined 95% upper limit. The mass range between 160 and 170 GeV/c^2 is excluded at 95% confidence level. The exclusion cross section at the Higgs mass 115 GeV/c^2 is about 3 times higher compared to the Standard Model expectation.

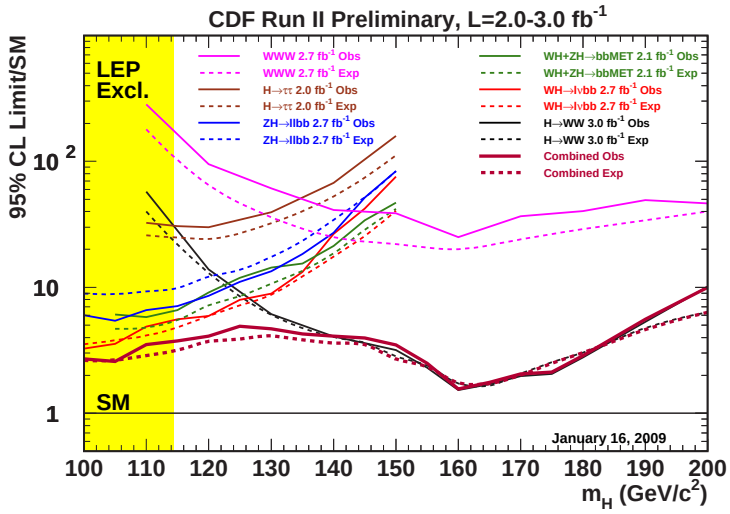

Figure 1.6: The summary of the CDF combined 95% upper limit on the Higgs boson production cross section normalized to the Standard Model expectation. The contribution of each channels are also shown.

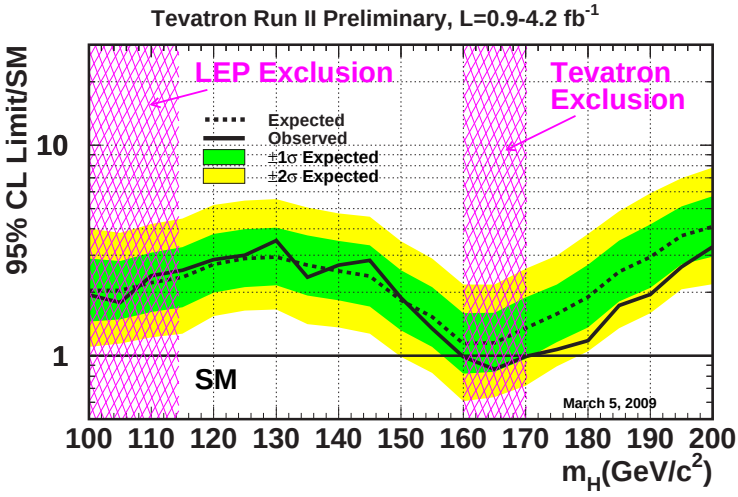

Figure 1.7: The summary of the Tevatron combined 95% upper limit on the Higgs boson search. The mass range between 160 and 170 GeV/c^2 was excluded.

1.2.2 Indirect Searches

The Higgs boson mass is not theoretically predicted, but it is possible to estimate using theoretical considerations and precision electroweak parameter measurements. The Higgs boson contributes to the propagator of the W and Z bosons through loop-effects. The corrections to the W and Z masses are logarithmic functions of the Higgs mass leading to limited conclusions:

$$\Delta_r = \frac{3G_F}{8\pi^2\sqrt{2}}m_t^2 + \frac{\sqrt{2}G_F}{16\pi^2}m_t^2\left[\frac{11}{3}\ln\left(\frac{m_h^2}{m_W^2}\right) + \cdots\right] + \cdots \tag{1.20}$$

where the radiative corrections Δ_r is defined as:

$$\frac{m_W^2}{m_Z^2} + \sin^2\theta_W \equiv 1 + \Delta r \tag{1.21}$$

As above equation shown, the constraint on the Higgs mass is strongly related with the top quark and the W boson mass. The Electroweak working group [26] has been performing global fits to the electroweak data, with the current most precision measurement of $m_t = 173.1 \pm 1.3\mathrm{GeV}/c^2$ [27] and $m_W = 80.420 \pm 0.031\mathrm{GeV}/c^2$ [28]. Figure 1.8 shows the $\Delta\chi^2$ curve as a function of the m_H derived from global fits. The preferred Higgs mass from this fit corresponding to the minimum of the curve is

$$m_H = 87^{+35}_{-26}\,\mathrm{GeV}/c^2 \tag{1.22}$$

and the 95% confidence level upper limit is

$$m_H = 157\,\mathrm{GeV}/c^2 \tag{1.23}$$

The upper limit increases to 186 GeV/c^2 when including the LEP direct search limit of 114.4 GeV/c^2. The recent combined result at the Tevatron (CDF and D0) excludes the mass range between 160 and 170 GeV/c^2 at 95% confidence level, which is also shown in yellow.

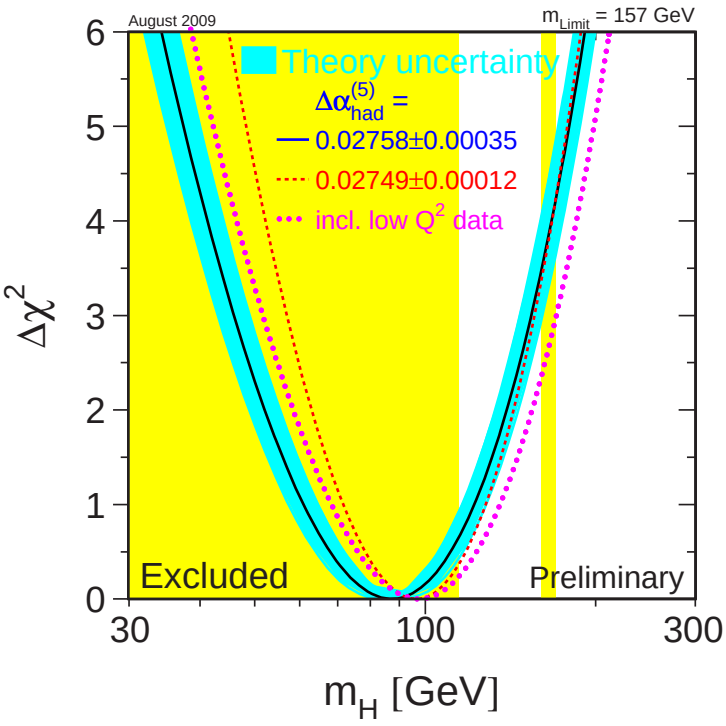

Figure 1.8: The $\Delta\chi^2$ distribution as a function of the Higgs mass. This electroweak global fit is based on the precision measurement at LEP, SLD, Tevatron, and NuTev.

Chapter 2

Experimental Apparatus

This chapter describes the Fermilab accelerator complex including the Tevatron collider, CDF II detector components, trigger and data acquisition (DAQ) system.

2.1 The Fermilab Accelerator Complex

A collider's design is vastly simplified if it collides particles with their antiparticles because the particles can travel opposite directions in the same beam-pipe and be bent by the same set of magnets. The Tevatron collides protons and antiprotons. Although electron-positron collisions are easier to analyze (because electrons are single point-like particles, unlike the composite protons), the large synchrotron radiation of electrons prohibits their use at high energies in circular accelerators. Because synchrotron radiation increases as the inverse of the fourth power of a particle's mass, protons, which have roughly 2000 times the mass of electrons, radiate much less. Protons and antiprotons are currently the only viable alternative to electrons and positrons.

Protons are abundant and readily available in nature; antiprotons must be produced and stored. In addition, a single accelerator cannot bring particles from rest to very high energies because no magnets have the dynamic range necessary. Consideration of these requirements led to the design of a chain of accelerators at Fermilab.

The Tevatron is the last in a chain of accelerators that gradually increase the energy of protons and antiprotons. An overview of the entire complex is shown in Figure 2.1. The Tevatron's first physics run, referred to as Run I, occurred from 1992-1996. After a series of upgrades, it began running again, referred to as Run II, in 2002 and is currently still running.

Proton Source

The protons used in the Tevatron are originally extracted from very pure hydrogen gas. For ease of insertion into the Booster, the particles accelerated are actually H^- ions instead of protons. Hydrogen gas is moved between two electrodes and a spark ionizes the hydrogen into electrons and H^+ ions. The positive ions strike a cathode made of cesium, which has a low work function and thus releases electrons easily, and occasionally pick up two electrons and form H^- ions. An electrostatic extractor sends them to the preaccelerator.

Preaccelerator

The preaccelerator is a Cockcroft-Walton-style [29] electrostatic accelerator. Ions from the proton source are subjected to a potential of $-750\,\mathrm{KeV}$, thus producing beams of H^- ions with an energy

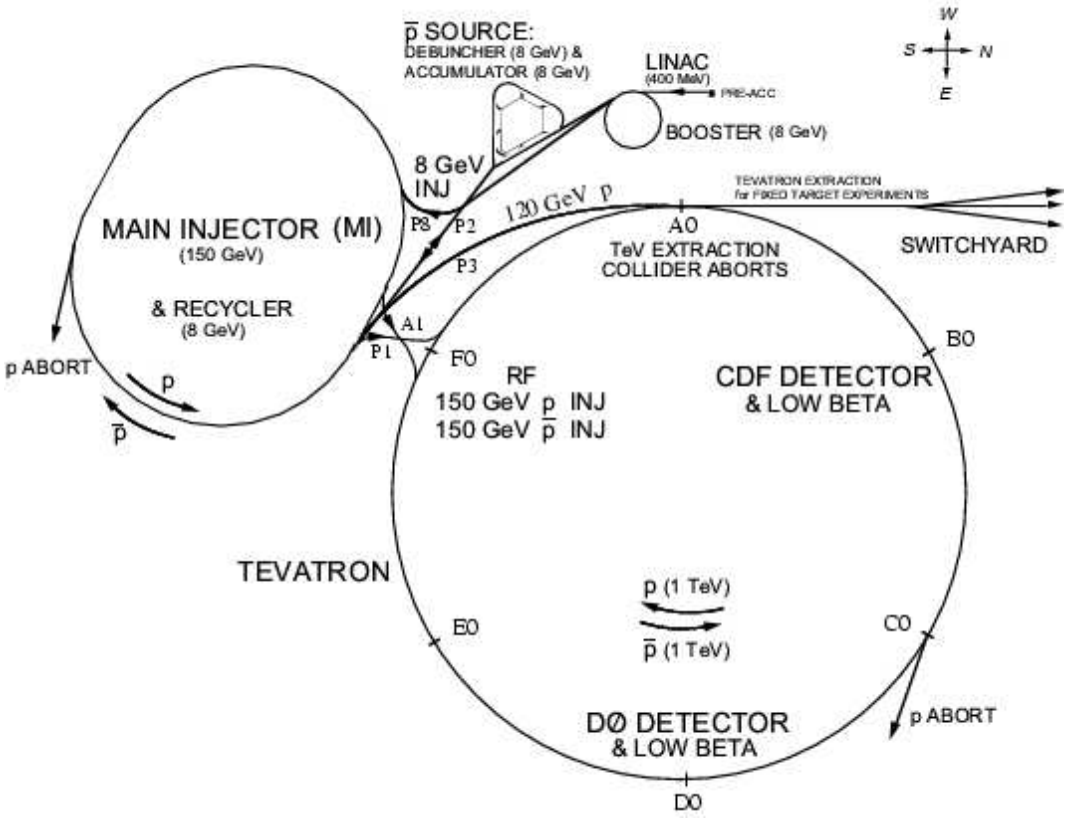

Figure 2.1: A diagram of the Fermilab accelerator chain.

of $750\,\mathrm{KeV}$. The H^- ions are steered and focused by magnets down a transfer line to the Linac.

Linac

The next stage of acceleration is a linear accelerator, abbreviated Linac, built in two sections. The older section consists of five drift tubes, modeled after Luis Alvarez' original proton linear accelerator, that accelerate the ion beam to $117\,\mathrm{MeV}$. The newer section added in 1993, has seven side-coupled cavity modules that accelerate the H^- ions to $400\,\mathrm{MeV}$.

At the far end of the Linac is a chopper, that electrostatically selects a portion of the Linac beam to be sent along a transfer line to the Booster. The Linac completes fifteen acceleration cycles per second.

Booster

The Booster is a proton synchrotron, approximately 150 m in diameter, that accelerates protons to 8 GeV. It has the same duty cycle as the Linac, 15 Hz. The acceleration is accomplished by eighteen ferrite-tuned RF cavities located around the ring. Ninety-six conventional magnets with a maximum field of 0.7 T bend the beam into a circular orbit. The Booster is able to hold multiple batches of particles from the Linac at once to increase beam intensities, often storing eleven or twelve batches in its ring.

A special set of magnets handles the injection of incoming H^- ions from the Linac. Magnets

bend the circulating protons and the injected H^- ions into a single beam that points through a sheet of foil. The foil strips the electrons from the H^- ions, leaving behind only protons. A similar set of magnets steers the beam back into the Booster orbit while removing any leftover H^- ions.

A set of fast kicker magnets extracts the proton beam from the Booster. The protons go into a transfer line that leads to the Main Injector.

Main Injector

The Main Injector is a large proton synchrotron with a diameter of about 1 km. It has two main functions involving the Tevatron: accelerating protons and antiprotons to 150 GeV for injection into the Tevatron, and accelerating protons to 120 GeV to be sent to the antiproton source.

The Main Injector uses 344 dipole magnets and 208 focusing quadrupole magnets, all conventional water-cooled electromagnets, to steer the proton beam. It can accelerate protons to 150 GeV in two seconds.

Antiproton Source

The antiproton source produces antiprotons for use in Tevatron collisions. The Main Injector sends 120 GeV protons down a transfer line to a nickel target. (Nickel was chosen because it can absorb more heat without melting than other metals.) Antiprotons are among the products resulting from this collision; they are selected by an electromagnetic selector and focused down a transfer line to the Debuncher. Studies have shown that 120 GeV is the optimal energy for antiproton production; at this energy, approximately one antiproton is collected per 10^5 protons sent to the antiproton source. The resultant antiprotons have an average energy of about 8 GeV.

Debuncher

The Debuncher is not an accelerator but a triangular storage ring. Its main purpose is to "debunch" the particle beam, removing its RF bunch structure. Magnets in the Debuncher decrease the momentum spread of the antiprotons by rotating them in phase space, trading momentum spread for time spread. This results in a beam of particles that have no RF bunch structure but have roughly uniform momentum. Antiprotons remain in the Debuncher until the next batch of protons is sent to the antiproton target, at which point the antiprotons are sent to the Accumulator.

Accumulator

The Accumulator lies in the same tunnel as the Debuncher. It is a long term antiproton storage ring, designed to store antiprotons with minimal losses for days. Antiprotons from the Debuncher are manipulated by RF systems in the Accumulator to fill a stable region of phase space, known as the core. The core is kept as small as possible to minimize the momentum spread of the antiprotons; a smaller beam gives a higher luminosity upon injection into the Tevatron.

While the antiprotons stay in the Accumulator, they are reduced in transverse momentum through a process called stochastic cooling [30]. This procedure measures the momentum spread of a group of antiprotons and sends a signal across the ring to corrector magnets, which adjust their fields for each group of particles to reduce the momentum spread of those particles. This results in denser antiproton beams injected into the Tevatron, increasing the resulting luminosity.

Extraction from the Accumulator requires the antiprotons to be collected into bunches again. Adiabatic activation of RF stations causes a portion of the beam to be collected into bunches,

which are then transferred back to the Main Injector, decelerated to 8 GeV, and injected into the Recycler.

Recycler

When the Accumulator reaches its maximum optimal capacity, its antiprotons are passed into the Recycler, a ring of permanent magnets in the same tunnel as the Main Injector. This storage ring keeps antiprotons at 8 GeV, collecting them until the Tevatron is ready for injection. In the Recycler, antiprotons are cooled further using a process called electron cooling [31], in which a beam of electrons is accelerated to the same energy as the antiprotons and runs alongside them. Transverse momentum from the antiproton beam is passed to the much lighter electrons, causing the antiprotons to lose transverse momentum, making the beam smaller. Antiprotons are injected from the Recycler to the Main Injector, which accelerates them to 150 GeV for injection into the Tevatron.

Tevatron

The Tevatron is a large synchrotron, 1 km in radius, that accelerates particles from 150 GeV to 980 GeV. It keeps both protons and antiprotons in the same beampipe, revolving in opposite directions. Electrostatic separators produce a strong electric field that keeps the two beams from touching except at the collision point. The beam is steered by 774 superconducting dipole magnets and 240 quadrupole magnets with a maximum magnetic field of 4.2 T. They are cooled by liquid helium to 4.2 K, at which point the niobium-titanium alloy in the magnets becomes superconducting.

The Tevatron holds 36 bunches each of protons and antiprotons. The process of injecting particles into the machine, accelerating them, and initiating collisions, referred to as a shot, starts with injection of protons, one bunch at a time, at 150 GeV from the Main Injector. The antiprotons are injected four bunches at a time from the Recycler through the Main Injector. RF cavities accelerate the beams to 980 GeV, and then some electrostatic separators switch polarity to cause the beams to collide at two points. Each collision point lies at the heart of a particle detector: one named D0 and the other named the Collider Detector at Fermilab (CDF).

2.2 The CDF II Detector

The CDF II detector is a general purpose detector designed to study $p\bar{p}$ collisions at the Tevatron. It was commissioned in the beginning of Run II in 2001, and still continues taking data. The detector components are arranged in cylindrical shape. The position of the sub-detectors are described in cylindrical coordinates (r, ϕ, z) with fixing the origin to the geometric center of the detector. The $\phi = 0$ is parallel to the ground and points out of the Tevatron ring. The z-axis points along the beam in the direction of the protons.

The outgoing particles are described in spherical coordinates. The z-axis is replaced by the polar angle θ. In the event reconstruction, the transverse momentum of particles $p_T = |\boldsymbol{p}|sin\theta$ is measured in the transverse plane, and their direction is given by the pseudorapidity η. The pseudo-rapidity is defined as

$$\eta = -\ln \tan(\frac{\theta}{2}) \tag{2.1}$$

which is a good approximation at high energies ($p_T \gg m$) to the rapidity

$$y = \frac{1}{2}\ln(\frac{E+p_z}{E-p_z}) \tag{2.2}$$

where E is the particle's energy and p_z is its momentum along the z-axis.

A solid cutaway view of the CDF II detector is shown in Fig. 2.2. In the center of the detector, the charged particle tracking system is enclosed by a superconducting solenoid. Outside the solenoid is the calorimeter system which is surrounded by the muon detectors.

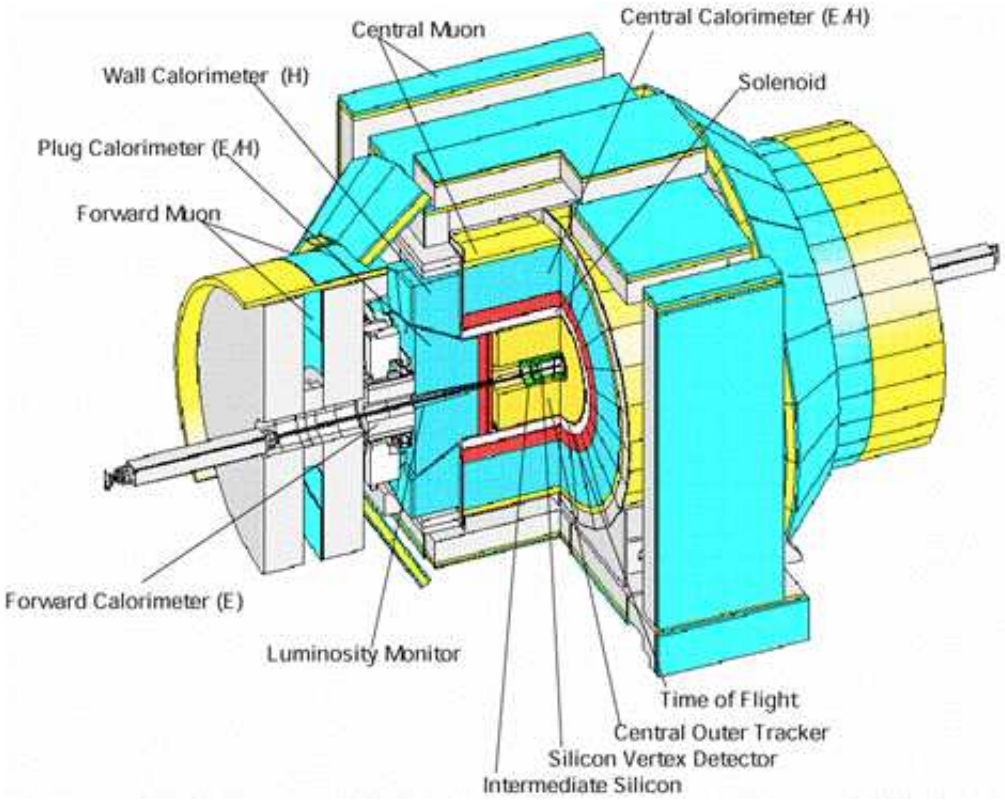

Figure 2.2: Isometric view of the CDF II detector.

2.2.1 Tracking System

The innermost part of the CDF II detector is the tracking system which is composed of multilayer silicon microstrip detectors, an open-cell wire drift chamber, and a superconducting solenoid magnet. The coverage of these detectors are illustrated in Figure 2.3. It is used to reconstruct trajectories of charged particles and precisely measure their momenta. The reconstructed particle trajectories are called tracks. Good resolution is required to detect displaced secondary vertices, which is a key to detect B hadrons.

Silicon Detectors

The silicon detector consists of three parts: Layer 00 (L00) [32], the Silicon Vertex Detector (SVXII) [33], and the Intermediate Silicon Layers (ISL) [34], as shown in Figure 2.4. The detector offers full tracking coverage for $|\eta| < 2.0$ as shown in Figure 2.4 (left).

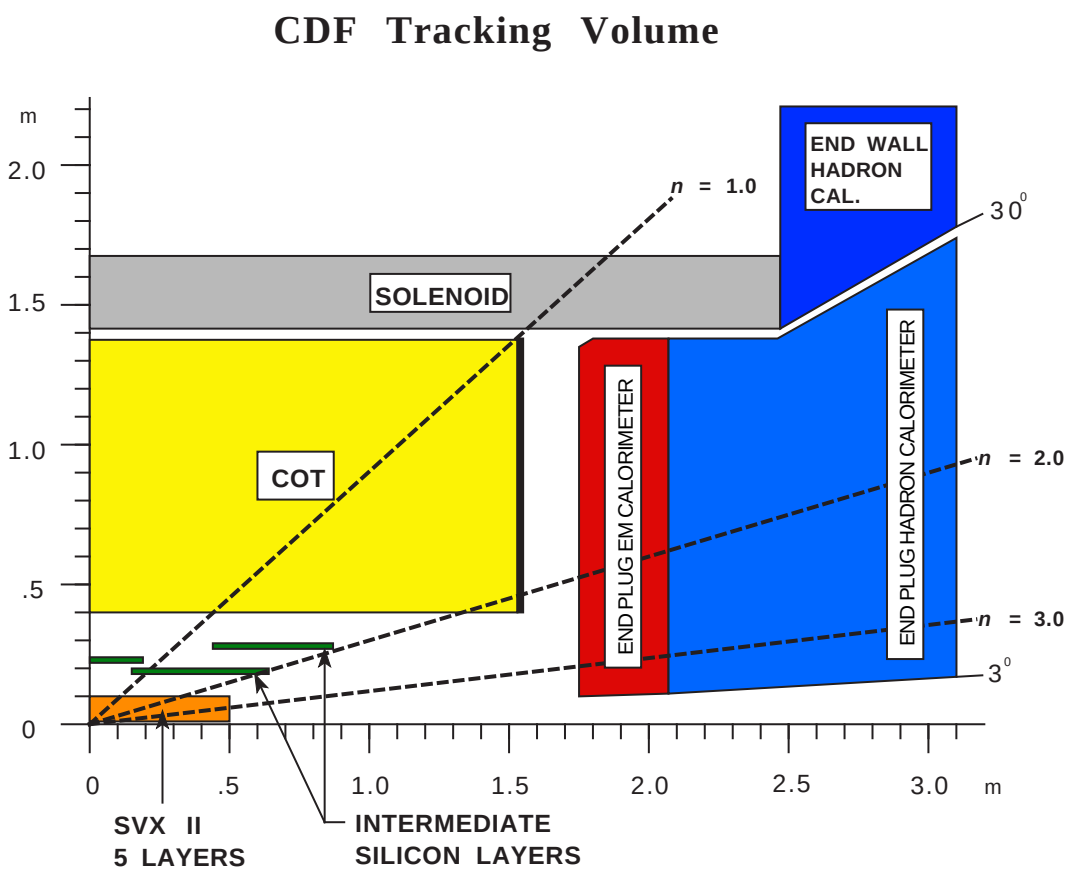

Figure 2.3: The CDF tracking system.

All the three sub-detectors are constructed from wafers of n-type silicon with thin strips ($\sim$10 μm) doped with p-type silicon (n-type in addition for SVXII sensors). The reverse bias voltage extends the depletion region from the p-n junction. When a charged particle passes through the depleted region, it ionizes the silicon wafer creating electron and hole pairs. The voltage moves electrons to one side of the sensor, the holes to the other side. Then, collected charge is read out by ASIC chips mounted at the end of the sensors. The spacial resolution is varying depending on each silicon sub-detector, since pitches are ranging from 25 μm to more than 100 μm.

L00: The L00, the innermost silicon detector, consists of one layer of single-sided silicon attached directly to the beampipe, only at $\sim$1.5 cm radius. Its purpose is to improve the resolution of the track impact parameter and position of secondary vertices.

SVXII: The SVXII is the main part of the silicon detector, which consists of five concentric layers of double-sided silicon. These layers are placed at radii from 2.4 cm to 10.7 cm. The hit information of the SVXII provides high resolution tracking information and is especially useful for reconstructing displaced secondary vertices.

ISL: The ISL is the outermost silicon detector, which consists of a single layer at $|\eta| < 1.0$ (at a radius of 22 cm) and two layers at $1.0 \leq |\eta| \leq 2.0$ (at a radius of 20 cm and 29 cm). This detector helps the connection of tracks between the Central Outer Tracker and the SVXII. This improves the track resolution and the performance of forward tracking in $|\eta| \leq 2.0$.

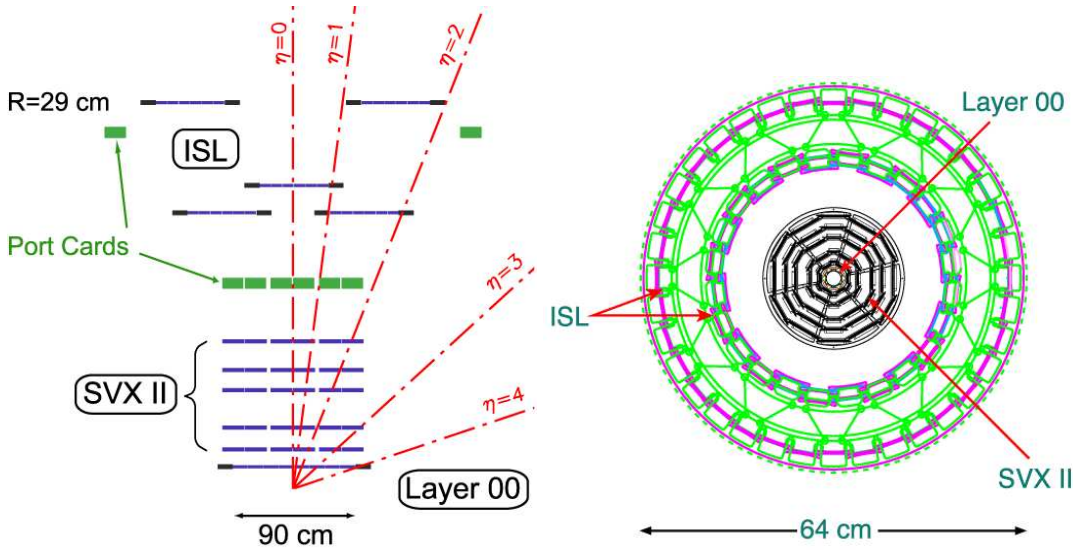

Figure 2.4: The CDF silicon detector. Left: the coverage of the silicon detector in r-z plane. Right: Configuration of the silicon detector in r-ϕ plane.

Central Outer Tracker (COT)

The COT is a cylindrical drift chamber that sits directly outside of the silicon detectors in the central region ($|\eta| < 1.0$) [35]. The chamber consists of eight cylindrical radial sections ("superlayers") of 310 cm long cells at radii between 40 and 132 cm from the detector center. The eight superlayers are placed in alternating axial and stereo sections: wires in axial superlayers run parallel to the z-axis, while wires in stereo superlayers are strung at $\pm$ 2 degree angles with respect to the z-axis. The number of cells in the superlayer increases radially outwards, the innermost superlayer consists of 168 cells and the outermost one consists of 480 cells. Each cell contains twelve sense wires and thirteen potential wires placed alternately. The chambers are filled with a mixture of argon and ethane gasses, which is chosen to have a uniform drift velocity across the cell volume.

Along a charged particle passing through the chamber, the gasses in the chamber are ionized. The electrons are drifted forward the sense wire by the electric field, and then they create an avalanche of charges which induce a pulse onto the sense wire. The position resolution of the COT is about 140 μm per cell, and the transverse momentum resolution is $\frac{\sigma_{p_T}}{p_T^2} = 0.0015\,[\mathrm{GeV}/c]^{-1}$.

Time-of-Flight System (TOF)

The TOF detector [36] is incorporated into the CDF detector in order to identify particles up to 1.5 GeV/c. By measuring the time it takes for a collision product to reach the TOF, we can separate particles which have different masses, such as $\pi^{\pm}$ and $K^{\pm}$. This detector is located between the COT and the superconducting solenoid at a radius of 140 cm with a coverage in $|\eta| \leq 1.0$. In this analysis, we do not use for particles discrimination but use for the event veto coming from cosmic rays.

Superconducting Solenoid

The superconducting solenoid operated at a current of about 4650 A produces an uniform magnetic field of 1.4 T parallel to the z-axis. The conductor is made of Al-stabilized NbTi. This strong magnetic field bends the trajectory of high-p_T charged particles, allowing us to reconstruct their momentum using the tracking system.

2.2.2 Calorimeters

The CDF calorimeters measure the energy of both charged and neutral particles. They are sampling scintillator calorimeters segmented into towers having a geometry projected to the detector center. The calorimeter system consists of electromagnetic (EM) and hadronic calorimeters, covering 2π in azimuth over the range $|\eta| < 3.6$. The cross section of the CDF calorimeter system is shown in Figure 2.5.

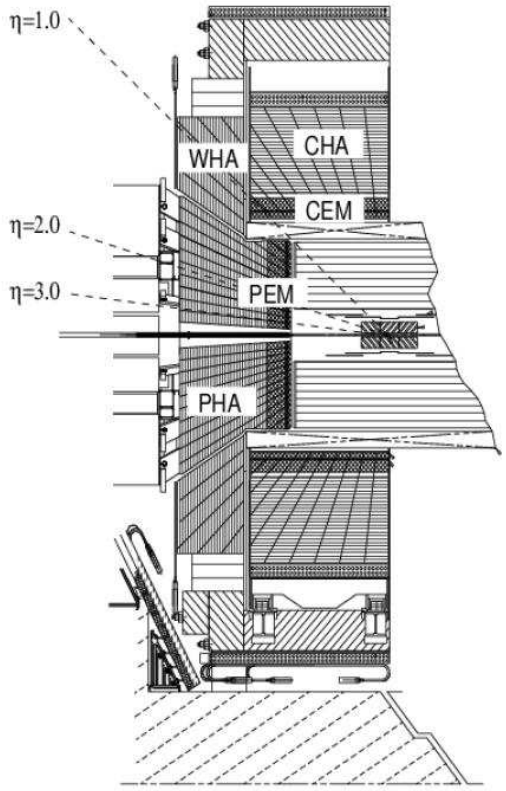

Figure 2.5: The CDF calorimeter system.

The EM calorimeter system consists of two sections: the central EM calorimeter [37] ($|\eta| < 1.1$) and the plug EM calorimeter [38] ($1.1 < |\eta| < 3.6$). Both sections include the main calorimeter, which mainly measures the energy of particles, and the shower maximum detector, which helps to improve the position resolution of the calorimeter clusters. The hadronic calorimeter system consists of three sections: the central hadronic calorimeter ($|\eta| < 0.9$), the wall hadronic calorimeter ($0.7 < |\eta| < 1.3$), and the plug hadronic calorimeter ($1.3 < |\eta| < 3.6$).

Central Electromagnetic Calorimeter (CEM)

The CEM is segmented into 24 towers in ϕ and 10 towers in η. The single CEM wedge is shown in Figure 2.6. It is a lead-scintillator sampling calorimeter having a radiation length (X_0) 18 X_0. The energy resolution of the CEM is

$$\frac{\sigma_E}{E} = \frac{13.5\%}{\sqrt{E\,(\mathrm{GeV})}} \oplus 2\% \tag{2.3}$$

where the notation $\oplus$ sums the constant and stochastic term in quadrature.

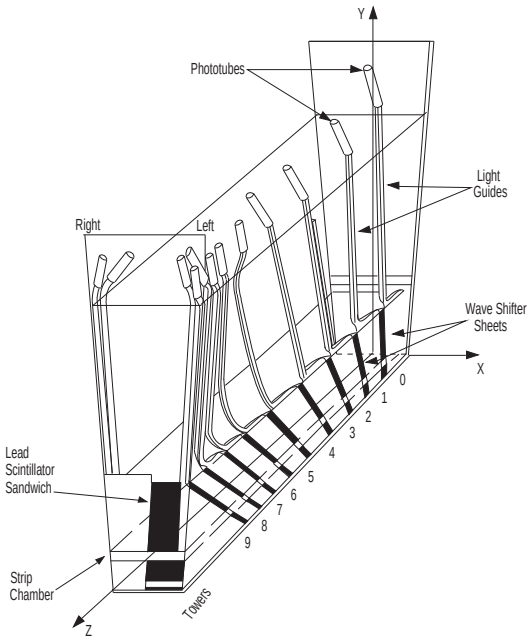

Figure 2.6: The single CEM wedge.

Central Electromagnetic Shower Maximum Detector (CES)

The CES is a proportional chamber with wire and strip readout which improves the position resolution of the calorimeter clusters. The CES is placed at a position at which the shower for electrons and photons has the maximum number of particles, called the shower maximum. Its position corresponds to a depth of 6 X_0 of the EM calorimeter. The position resolution is 0.2 cm at 50 GeV.

Plug Electromagnetic Calorimeter (PEM)

The PEM is segmented into 12 towers in η and 24 (48) towers in ϕ for the inner (outer) groups. It is a lead-scintillator sampling calorimeter having a total thickness is 21 X_0. The energy resolution of the PEM is:

$$\frac{\sigma_E}{E} = \frac{14.4\%}{\sqrt{E\,(\mathrm{GeV})}} \oplus 0.7\% \tag{2.4}$$

Plug Electromagnetic Shower Maximum Detector (PES)

The PES [39] measures the shower maximum position similar to the CES. It is located at 6 X_0 depth and is made of two layers of 5 mm wide scintillator strips, with each layer having a 45° crossing angle relative to the other.

Central Hadronic Calorimeter (CHA)

The CHA, a iron-scintillator sampling calorimeters, is segmented into 24 towers in ϕ and 8 towers in η [40]. It is located directly outside of the CEM with 32 layers per tower, which corresponds to 4.7 interaction lengths (λ_I) thick. The energy resolution of the CHA is:

$$\frac{\sigma_E}{E} = \frac{50\%}{\sqrt{E\,(\mathrm{GeV})}} \oplus 3\% \tag{2.5}$$

Wall Hadronic Calorimeter (WHA)

The WHA extends the CHA coverage to fill the gap between the central and plug regions [40]. It is made of 15 layers of iron (5.0 cm) and scintillator (1.0 cm). The energy resolution of the WHA is:

$$\frac{\sigma_E}{E} = \frac{75\%}{\sqrt{E\,(\mathrm{GeV})}} \oplus 4\% \tag{2.6}$$

Plug Hadronic Calorimeter (PHA)

The PHA is made of 23 layers of alternating iron and scintillator. The energy resolution of the PHA is:

$$\frac{\sigma_E}{E} = \frac{80\%}{\sqrt{E\,(\mathrm{GeV})}} \oplus 5\% \tag{2.7}$$

2.2.3 Muon Detectors

The energy of high-p_T muons are not measurable with the calorimeter, since they pass through the detector materials by depositing only minimum ionizing energy. The CDF muon detectors consist of four systems and are located outside of the calorimeters. The muon system coverage is shown in Figure 2.7. A cross section view of a muon chamber is shown in Figure 2.8. When a muon passes through the muon system, the drift time in each layer is registered. We define a muon "stub" which requires a hit in three of the four layers of drift chambers.

Central Muon Detector (CMU)

The CMU [41] consists of four layers of planar drift chambers located outside of the CHA. It covers the central region of $|\eta| < 0.6$ and can detect muons with $p_T > 1.4\ \mathrm{GeV}/c$.

Central Muon Upgrade (CMP)

The CMP consists of four layers of planar drift chambers located outermost of the CDF for walls or behind the magnet return yokes. The CMP covers $|\eta| < 0.6$ and can detect muons with $p_T > 2.0\ \mathrm{GeV}/c$.

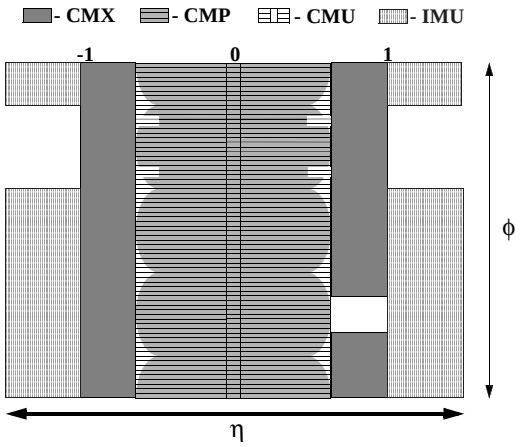

Figure 2.7: CDF muon coverage for the CMU, CMP, CMX, and BMU detectors. The BMU is referred as the IMU.

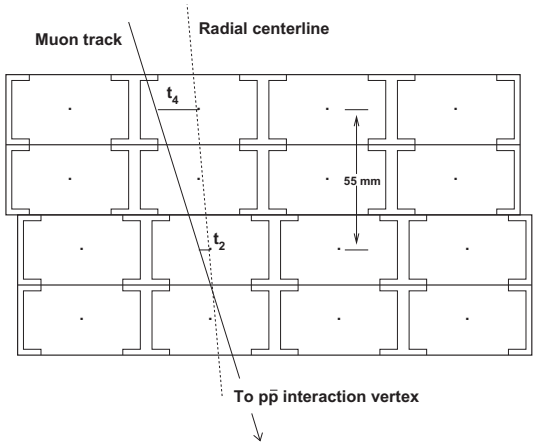

Figure 2.8: A cross section view of a CMU muon chamber.

Central Muon Extension (CMX)

The CMX consists of four to eight layers of drift chambers depending on the polar angle. It provides muon detection in the region $0.6 < |\eta| < 1.0$ and can detect muons with $p_T > 1.4\ \mathrm{GeV}/c$. The scintillator tiles (CSX) is also placed on the inside and outside of the CMX, used for improved triggering.

Barrel Muon Detector (BMU)

The BMU extends the muon detector coverage to $1.0 < |\eta| < 1.5$. Drift chambers and scintillators are atatached surrounding the forward toroid magnets.

2.2.4 Luminosity Monitor

Luminosity

The collision rate of protons and antiprotons is quantified by the instantaneous luminosity. The luminosity is calculated with the following formula:

$$\mathcal{L} = \frac{f_r N_B N_p N_{\bar{p}}}{2\pi(\sigma_p^2 + \sigma_{\bar{p}}^2)} F\Big(\frac{\sigma_l}{\beta^*}\Big) \tag{2.8}$$

where f_r is the revolution frequency, N_B is the number of bunches, N_p and $N_{\bar{p}}$ are the number of protons or antiprotons per bunch, σ_p and $\sigma_{\bar{p}}$ are the beam sizes at the interaction point, F is a form factor which corrects for the bunch shape and depends on the ratio of the bunch length σ_l to the beta function β^* at the interaction point. β^* is a measure of the beam spreads, which are given by $\sqrt{\beta^* \epsilon}$ with ϵ being the beam emittance.

There is a continuous effort to maximize the peak luminosity which directly results in increasing the amount of data delivered by the Tevatron. The amount of data collected through Run II is expressed by the integrated luminosity ($\int \mathcal{L}$dt) which is measured in units of b^{-1}, where 1 b^{-1} is 10^{24} cm^{-2}. Figure 2.9 shows the integrated luminosity delivered by the Tevatron and recorded by the CDF.

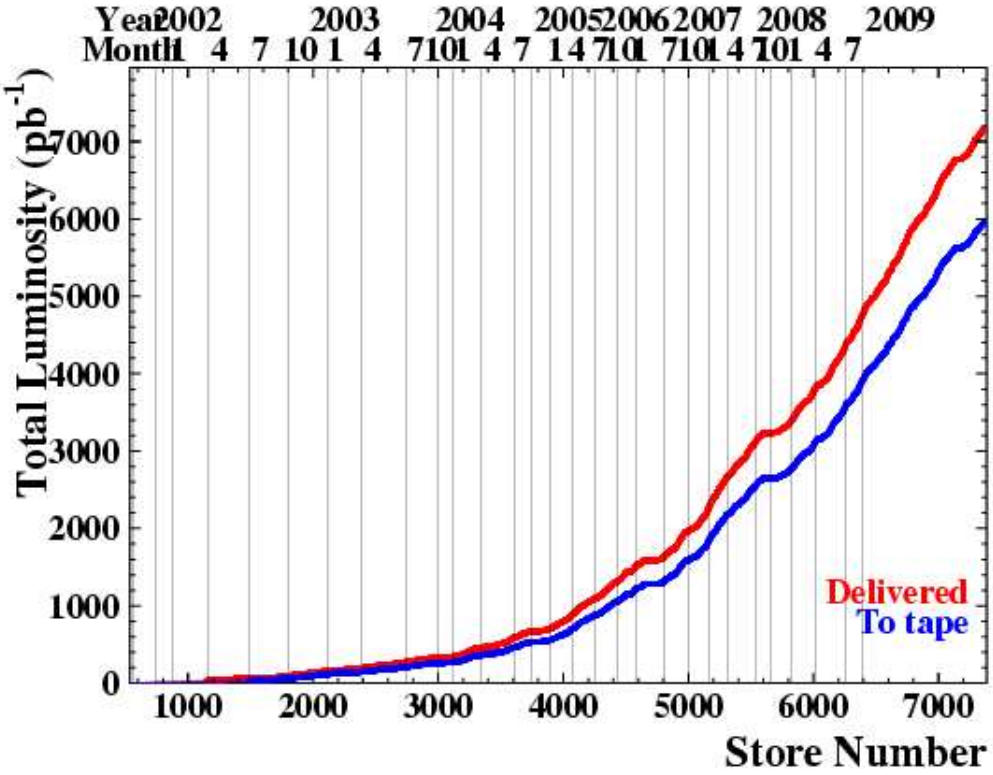

Figure 2.9: Total integrated luminosity delivered by the Tevatron and recorded by the CDF.

Cherenkov Luminosity Counters (CLC)

The beam luminosity is measured by using the CLC detector [42] located in the forward region ($3.7 < |\eta| < 4.7$) of the CDF detector on both sides. The CLC consists of long conical gaseous Cherenkov counters that monitor the average rate of inelastic $p\bar{p}$ collisions per bunch crossing ($R_{p\bar{p}}$). The instantaneous luminosity ($\mathcal{L}_{inst}$) is calculated from the next expression:

$$\mu \cdot f_{BC} = \sigma_i \cdot \mathcal{L}_{inst} \cdot \epsilon \tag{2.9}$$

where μ is the number of interactions per bunch crossing counted by the CLC detector, f_{BC} is the bunch crossing frequency (2.5 MHz for 36×36 bunch operations), ϵ is the CLC acceptance for a single $p\bar{p}$ interaction, and σ_i is the inelastic $p\bar{p}$ cross section at the Tevatron (60.7 $\pm$ 2.4 mb).

2.2.5 Data Acquisition System

The bunch crossing rate of the Tevatron is 2.5 MHz for 36×36 bunch operations which corresponds to 396 ns separation. The actual interaction rate is bit lower, about 1.7 MHz. Since this rate is too high to record every event into disk, we need to discard the most events while interesting ones must be identified. The selection of events is performed by the fast online electronics, called the trigger system. The CDF trigger system has a three level architecture (called Level 1, Level 2, and Level 3) and is designed to reduce the data rate by identifying the physically interesting events. Once an event is accepted by the Level 3 trigger, then the data are sent to the Consumer Sever/Logger (CSL) that is the final component in the CDF data acquisition system. The data flow in the CDF trigger system is shown in Figure 2.10.

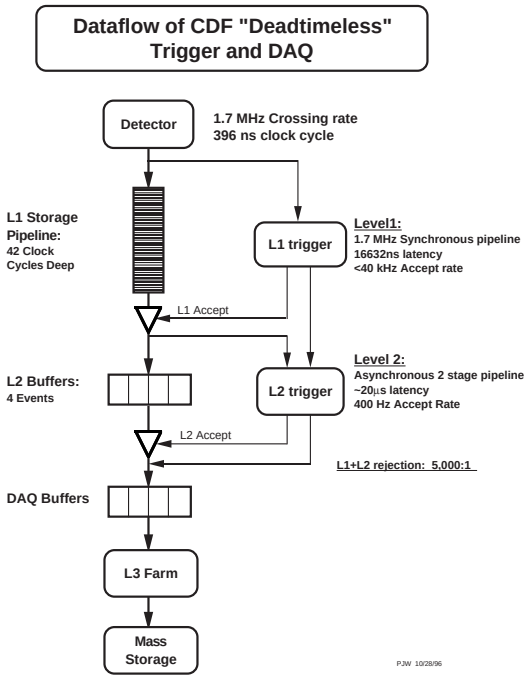

Figure 2.10: Data flow in the CDF data acquisition system.

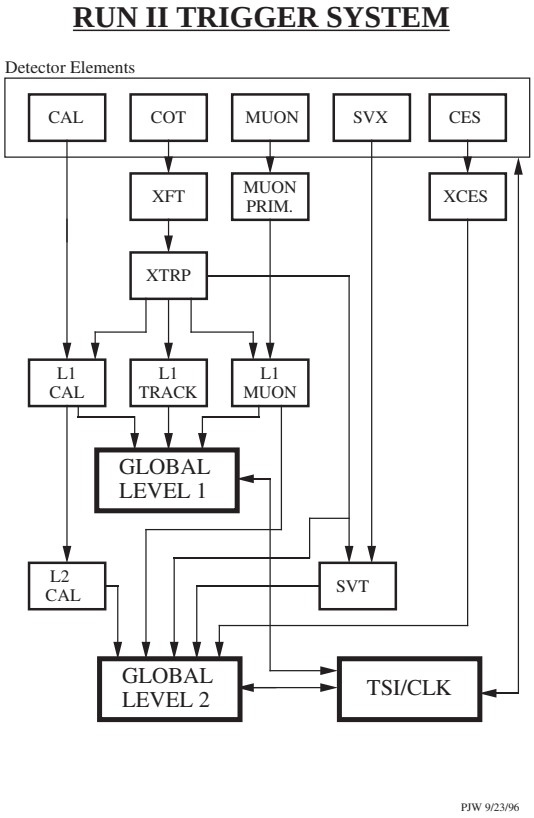

Figure 2.11: Block diagram of the Level 1 and Level 2 trigger path.

Level 1

The Level 1 trigger (L1) discards about 97% of the events, resulting in the acceptace rate to about 40 kHz. Figure 2.11 shows the trigger path from the Level 1 to the Level 2. The L1 CAL can make its decision based on clusters of energy in the calorimeters, missing energy from the energy conservation, or the sum of calorimeter energy. A system called Extremely Fast Tracker (XFT) [43] reconstructs tracks using the COT information, and the tracks found by the XFT are used for the L1 trigger decision. The CMU can also provide L1 trigger for muon candidates.

Level 2

The Level 2 trigger (L2) reduces the event rate to about 400 Hz. The L2 system consists of several asynchronous subsystems which provide input to programmable L2 processors. The L2 decisions are made based on the following:

- L2 cluster finder (L2CAL): The L2CAL combines adjacent calorimeter towers over 1 GeV threshold starting from a seed tower of minimum 3 GeV.
- CES information: The shower maximum detector information provides the position resolution for electron and photon showers with better than the cluster location. It is also used to match with the tracking information.
- Silicon Vertex Tracker (SVT) [44]: The SVXII information is combined with the L1 XFT

track information by the SVT, a system that rapidly analyzes the silicon data to look for a displaced vertex.

- Muon information: The muon trigger combines information from the muon detector and from the L1 XFT track.

Level 3

The Level 3 trigger (L3) consists of a few hundred of computers. The L3 computer farm reconstructs the event in software and filter the event rate to about 100 Hz. Events that pass L3 decision are written to disk.

Consumer Server/Logger

Once an event is accepted by the L3 trigger, it sends to the Consumer Server/Logger (CSL) system. The CSL is responsible for categorizing events by the trigger path, writing them to the disk, and sending a fraction of events to online processors for real time monitoring of data quality.

Chapter 3

Event Reconstruction

We search for the Higgs boson in events with $WH \rightarrow \ell\nu b\bar{b}$, which include a lepton, missing energy, and two jets as the final observables. Definition and description of the relevant observables for high level detector objects and the event reconstruction are discussed in this chapter.

3.1 High Level Detector Object

The detector raw outputs are primarily used to reconstruct high level detector object, which includes tracks, sequences of hits left by charged particles as they pass through the tracking detectors, and calorimeter clusters, collections of towers in which energy from particles is deposited. Associating these together, with applying quality cuts, we reconstruct electrons, muons, jets and missing transverse energy.

3.1.1 Tracking

The tracking system of the CDF II detector is described in Section 2.2.1. It detects trajectories of charged particles. This information is used in primary vertex reconstruction, lepton identification, and heavy flavor tagging.

The tracking detectors are enclosed by the superconducting solenoid, which provides a uniform magnetic field inside the detector with field lines parallel to the beam-axis. Charged particles traveling through magnetic field are curved depending on their momenta and charges. The resulting trajectory in transverse plain is a helix. The following parameters are used in the description of the trajectory in three dimensions:

C: half-curvature of the trajectory defined as

$$C = \frac{1}{2Q\rho} \tag{3.1}$$

where ρ is the radius of the projection of the trajectory to the transverse plane. It carries the same sign as the charge of the particle and is inversely proportional to the p_T of the track.

cotθ: cotangent of the polar angle of the trajectory at closest approach to the origin.

d_0: the impact parameter, the minimal distance between the trajectory and the origin in the transverse plane, defined as

$$d_0 = Q \cdot (\sqrt{x_0^2 + y_0^2} - \rho) \tag{3.2}$$

where x_0 and y_0 are the coordinates of the center of the helix circle in the transverse plane.

ϕ_0: the azimuthal angle of the trajectory at the point of closest approach to the detector center.

z_0: the z position of the trajectory point closest to the detector center.

We use four tracking algorithms in this analysis, called COT stand-alone tracking, Outside-In (OI) tracking, Inside-Out (IO) tracking, and Phoenix tracking.

The primary tracking algorithm of CDF begins with the COT. Firstly, hits in the COT are identified. These are associated together within each superlayer to form short track segments, which can be combined across superlayers to form a track. Because the superlayers of the COT alternate in orientation between axial and stereo superlayers, the tracking algorithm compares segments in all axial superlayers first, starting with tracks in the most outer superlayer and finding the segment that gives the best fit. It then adds the stereo superlayers and performs the fit again to create a final COT stand-alone track. COT stand-alone tracks are required to have hits in at least four of eight superlayers, using ≥ 2 axial and ≥ 2 stereo superlayers.

The OI tracking can extend the COT stand-alone tracks by adding high-resolution hit information from the silicon detector. It attaches axial silicon hits to COT tracks and then performs pattern recognition on the small angle and 90° stereo strips. At each wafer intersected by the seed track, every hit is attached to a separate copy of the seed track. Then, the track is extrapolated to the next wafer where the same matching procedure is performed until the track reaches the most inner silicon wafer. At the end, the track combination with the highest number of hits and lowest χ^2/dof is kept.

Due to the limited COT coverage ($|\eta| < 1.0$) and the strict hit requirement (at least four of eight superlayer), tracking in the forward region requires other algorithms, called IO tracking and Phoenix tracking. IO tracking algorithm firstly finds tracks in the silicon detector, requiring hits in at least three layers, then extends them by adding hits in the COT that are not already used to form COT stand-alone or OI tracks. Phoenix tracking uses a cluster in the plug calorimeter and the primary vertex as two points of the track and then looks for hits in between that would complete the track. It uses the energy of the cluster to estimate the momentum of the particle, giving a curvature estimate which is used to search for hits in the tracking region.

In this analysis, most tracks are from a collection which includes COT stand-alone tracks, OI tracks, and IO tracks. Phoenix tracks are only used to identify plug electrons.

3.1.2 Primary Vertex

Primary vertex location is required to calculate transverse energies in the calorimeter towers and to derive objects such as jets and missing energy, since the angle θ is defined by the vector pointing from the vertex to the shower maximum detectors within the calorimeter towers. Using the detector center, instead of the z-position of the vertex in the $\not\!\!E_T$ calculation, has an impact on the $\not\!\!E_T$ beyond the level of the corrections applied for jets and muons.

Vertices are found by fitting good quality tracks [45]. At high luminosities, several collisions may occur at one bunch crossing. The position of the vertex in the z-coordinate has a Gaussian spread of $\sigma_z = 29$ cm around the detector center. Therefore, the vertices for multiple interactions are normally separated in z-position. The estimate of the vertices is started with finding seed vertices in the z-coordinate. Then, the z-position of each vertex is calculated from the weighted average of the z-coordinate of all tracks within 1 cm of the seed vertex. The primary vertex is determined by an iterative vertex finding algorithm which uses tracks around a seed vertex to form a new vertex position. The χ^2 for all tracks relative to the new vertex is calculated, tracks with degraded χ^2 are removed, and the cycle is repeated until all tracks have a good χ^2. We finally

define the vertex associated with the highest sum of the track p_T as the primary vertex of the event.

3.1.3 Calorimeter Clustering

High momentum electrons, photons, and jets leave energy in small contiguous groups of calorimeter towers which can be identified as an energy cluster. Firstly, calorimeter clustering algorithm starts finding a seed cluster that has an energy larger than a certain threshold. Then, adjacent towers with energy greater than a lower threshold are added to form a cluster. The position of the cluster is defined by the energy-weighted mean of the towers in the cluster, and the total energy is estimated by the sum of the energies of the towers in the cluster. Once a cluster is defined, the precision of its position can usually be improved by matching it with a cluster in the shower maximum detector, which is constructed with a similar algorithm but which is optimized to achieve higher position resolution.

3.2 Particle Identification

Once high level detector objects are reconstructed, it is possible to identify physical objects from which we start physics analysis. In this section, we describe the identification of leptons, neutrinos (missing transverse energy), and jets. These objects are the final state of our signal process $WH \rightarrow \ell\nu b\bar{b}$.

3.2.1 Leptons

Electron

This analysis considers two categories of electrons: central electron (CEM) and plug electron (PHX). These types are basically defined by the detector when they are measured.

The central electron reconstruction starts from a track with $p_T > 9\ \mathrm{GeV}/c$ that extrapolates to a cluster of CEM with $E_T > 20\ \mathrm{GeV}$. To improve the purity of the electron selection, we apply several cuts as summarized in Table 3.1. The variables in Table 3.1 are defined as:

- p_T: The track p_T associated to the EM cluster.
- E_T: The transverse energy of the electron candidate defined as $E_T = E \sin\theta$.
- $E_{\mathrm{HAD}}/E_{\mathrm{EM}}$: The ratio of the total hadronic cluster energy to the total EM energy.
- E/p: The ratio between the cluster energy to the momentum of the associated track.
- Isolation: The ratio of the transverse energy surplus in a cone of radius $\Delta R < 0.4$ around the cluster center to the transverse energy of the cluster.
- L_{shr}: The difference between the lateral distribution of the energy in the calorimeter towers and what is expected for an electromagnetic shower. The expectation is derived from simulations and modified to fit test beam data. This requirement helps remove hadronic showers that might imitate electromagnetic showers.
- $|\Delta_x|_{\mathrm{CES}}$ and $|\Delta_z|_{\mathrm{CES}}$: The distances in the transverse plane and along the z-axis between the cluster position from the CES measurements and the extrapolated track associated with the cluster.

Central Electron Selection
To be in the active region of CES and CEM
$p_T \geq 10\,\mathrm{GeV}/c$
$E_T \geq 20\,\mathrm{GeV}$
COT Axial Segments ≥ 3
COT Stereo Segments ≥ 2
Hits per COT Segments ≥ 5
$\lvert z_0\rvert_{\text{track}} \leq 60$ cm
$E_{\text{HAD}}/E_{\text{EM}} \leq 0.055 + 0.00045 \times E/\mathrm{GeV}$
$E/p \leq 2.0$ unless $p_T \geq 50\,\mathrm{GeV}/c$
Isolation ≤ 0.1
$L_{\text{shr}} \leq 0.2$
$\lvert\Delta_z\rvert_{\text{CES}} \leq 3.0$ cm
$-3.0 \leq Q \times \lvert\Delta_x\rvert_{\text{CES}} \leq 1.5$ cm
$\chi^2_{\text{CES}} \leq 10$
Photon Conversions Veto

Table 3.1: Selection requirement for central electrons [46].

- χ^2_{CES}: Comparison of the CES shower profile with that of the test beam electrons given as the chi-square probability for the fit.
- Photon conversion veto: Electrons from photon conversions through the detector material are vetoed by rejecting electron candidates if an oppositely charged track with a small distance of closest approach is found.

The plug electron reconstruction starts from matching the plug EM cluster to a track reconstructed by Phoenix algorithm. The selection requirements are shown in Table 3.2:

- $\chi^2_{3\times3\,\text{PEM}}$: A χ^2 fit to electron test beam data for shower maximum profile.
- PES $U_{5\times9}$ and PES $V_{5\times9}$: The ratio of the central 5 strip energy to the central 9 strip energy.
- $\lvert\Delta_R\rvert_{\text{PEM}}$: The difference in the r–ϕ plane between the PES and PEM position measurements.
- $N_{\text{Si hits}}$: The number of hits in the silicon detector (L00, SVXII, and ISL) associated with the track.

Muon

This analysis considers two types of muons: CMUP and CMX. These types are basically defined by the detector which they pass through.

The central muon reconstruction is summarized in Table 3.3. Since CMU stand-alone muon candidates have a large fraction of fake muons coming from the punch-through particles through calorimeter, we also require a CMP detector stub to suppress fake muons and call such muons as CMUP muons. The range $0.65 < |\eta| < 1.0$ is covered by CMX detector. The selection requirements are explained below:

Plug Electron Selection
$E_T \geq 20\,\mathrm{GeV}$
$1.2 \leq \lvert\eta\rvert \leq 2.0$
$E_{\mathrm{HAD}}/E_{\mathrm{EM}} \leq 0.05$
$\chi^2_{3\times3\,\mathrm{PEM}} \leq 10$
PES $U_{5\times9} \geq 0.65$
PES $V_{5\times9} \geq 0.65$
Isolation ≤ 0.1
$\lvert\Delta_R\rvert_{\mathrm{PEM}} \leq 3.0$ cm
$N_{\mathrm{Si\,hits}} \geq 3$
$\lvert z_0\rvert_{\mathrm{Phoenix\ track}} \leq 60$ cm

Table 3.2: Selection requirement for plug electrons [46].

Central Muon Selection
$p_T \geq 20\,\mathrm{GeV}/c$
COT Axial Segments ≥ 3
COT Stereo Segments ≥ 2
Hits per COT Segments ≥ 5
$\lvert d_0\rvert_{\mathrm{track}} \leq 0.2$ cm if no silicon hits
$\lvert d_0\rvert_{\mathrm{track}} \leq 0.02$ cm if silicon hits
$E_{\mathrm{EM}} \leq \max(2, 2 + 0.0115(p - 100))\,\mathrm{GeV}$
$E_{\mathrm{HAD}} \leq \max(6, 6 + 0.0280(p - 100))\,\mathrm{GeV}$
$\lvert\Delta_x\rvert_{\mathrm{CMU}} \leq 3.0$ cm
$\lvert\Delta_x\rvert_{\mathrm{CMP}} \leq 5.0$ cm
$\lvert\Delta_x\rvert_{\mathrm{CMX}} \leq 6.0$ cm
Isolation ≤ 0.1
Cosmic Rays Veto

Table 3.3: Selection requirement for central muons [46].

- $|\Delta_x|_{\mathrm{CMU,\,CMP,\,CMX}}$: The distance between the actual stub in a given muon detector and the track position extrapolated to that detector.

- Cosmic Rays Veto: The impact parameter d_0 of the tracks are used to kill cosmic rays. Because most cosmic rays pass through the detector from the top to bottom, they often look back-to-back tracks reconstructed d_0 being identical.

Isolated Track

We use the isolated tracks to recover the gaps in the muon detector coverage. The isolated track reconstruction is similar to the reconstruction of the tracks associated with electron and muon candidates, but we do not apply any calorimeter related selection. Table 3.4 outlines the isolated track event selection requirement. The selection requirements are discussed below:

- χ^2 Probability: A track fit probability of a χ^2 per degree of freedom.

Isolated Track Selection
$p_T \geq 20\,\mathrm{GeV}/c$
$\lvert\eta\rvert \leq 1.2$
$\lvert d_0\rvert_{\text{track}} \leq 0.2$ cm if no silicon hits
$\lvert d_0\rvert_{\text{track}} \leq 0.02$ cm if silicon hits
COT Axial Hits ≥ 24
COT Stereo Hits ≥ 20
χ^2 Probability $> 10^{-8}$
Silicon Hits ≥ 3 (if expected hits ≥ 3)
Track Isolation ≥ 0.9

Table 3.4: Selection requirement for isolated tracks [47].

- Track Isolation: The p_T ratio between the isolated track candidate and other tracks in a cone of radius $\Delta R < 0.4$. This variable is defined as:

$$\text{TrkIsol} = \frac{p_T(\text{candidate})}{\left(p_T(\text{candidate}) + \sum p_T(\text{tracks})\right)} \tag{3.3}$$

  By definition, a track with no surrounding activity has an isolation of 1.0.

3.2.2 Jets

Jets are the results of hadronization of quarks and gluons. In this analysis, we reconstruct jets from a group of electromagnetic and hadronic calorimeter clusters which fall within a cone of radius $\Delta R = \sqrt{\Delta\phi^2 + \Delta\eta^2} \leq 0.4$ [48]. The calorimeter clusters which belong to electron candidate are not taken account for the jet reconstruction. Since the raw energy does not predict the correct parton energy due to instrumental and physical reason, we apply several jet energy corrections to estimate the energy of parton [49]. The corrected jet energy is expressed in the following equation:

$$E_T^{\text{parton}} = (E_{T,\,\text{jet}}^{\text{measured}} \times f_{\text{rel}} - E_T^{\text{MI}} \times N_{\text{vtx}}) \times f_{\text{abs}} - E_T^{\text{UE}} + E_T^{\text{OOC}} \tag{3.4}$$

where correction factors are:

$\boldsymbol{f_{\text{rel}}}$**:** a scale factor to make the jet response uniform over the pseudo-rapidity

$\boldsymbol{E_T^{\text{MI}} \times N_{\text{vtx}}}$**:** a correction for multiple interactions per beam crossing

$\boldsymbol{f_{\text{abs}}}$**:** an absolute energy correction determined by matching parton energy with jet energy

$\boldsymbol{E_T^{\text{UE}}}$**:** the contribution coming from the underling events

$\boldsymbol{E_T^{\text{OOC}}}$**:** an out-of-cone correction which is the energy of the parton emitted outside the jet cone

3.2.3 Missing Transverse Energy

Neutrinos cannot be detected by the detector, but they are identified from the missing energy. Since the z-component of momentum of the interacting partons are unknown, we cannot determine the z-component of the neutrino energy. However, we can determine the components in the transverse

plane the transverse momentum sum of initial partons can be ignored. The uncorrected missing transverse energy $\not\!\!E_T^{\text{raw}}$ is the negative of the vector sum of all calorimeter tower depositions projected on the transverse plane:

$$\not\!\!E_T^{\text{raw}} = -\sum_{i=\text{towers}} E_T^i \tag{3.5}$$

Since this missing transverse energy is measured from the raw calorimeter response, it needs to be corrected for the jet energy correction and for the muons escaped from the calorimeter. The missing transverse energy $\not\!\!E_T$ used in this analysis is then

$$\not\!\!E_T = \not\!\!E_T^{\text{raw}} - \sum_{\text{muon}} p_T + \sum_{\text{muon}} E_T(\text{EM} + \text{Had}) - \sum_{jet} E_T(\text{Jet Energy Correction}) \tag{3.6}$$

3.2.4 *b*-tagging

Physics processes with jets in their final observable particles suffer from huge amount of QCD background of light flavor jets, and searches in such a process become difficult to find a good sensitivity. The identification of b-jets (b-tagging) from the Higgs boson decay plays an important role in this analysis. Since most of the events coming from the background processes passing the W + jets selection do not contain b-jets in their final state, requirement of b-tagging provides a significant reduction of the non-signal processes. For this analysis, we employ three different b-tagging algorithms, a secondary vertex finding algorithm (SECVTX) [45], a jet probability tagging algorithm (JETPROB) [50], and a neural network tagging algorithm (NN). These algorithms can identify the b-jets using the B-hadron (such as B^0, Λ_B) specific features, such as its long lifetime or existence of leptons from its semi-leptonic decay.

Secondary Vertex *b*-tagging

B-hadrons having a proper decay length of about $c\tau = 500$ μm travel typically a few millimeters. The SECVTX uses tracks within a jet to reconstruct a decay vertex that is displaced from the primary vertex. The algorithm uses tracks within a cone of $\Delta R = 0.4$ about the jet direction. It forms vertices from the tracks with large impact parameter significance ($|d_0/\sigma_{d_0}|$). A two-pass approach is employed where high-quality vertices are searched for in the first pass and lower-quality vertices in the second pass.

- Pass 1: At least three tracks are required to pass the loose selection criteria ($p_T > 0.5\ \text{GeV}/c$, $|d_0/\sigma_{d_0}| > 2.0$). The secondary vertex is reconstructed out of the selected tracks, with one of the tracks required to have $p_T > 1.0\ \text{GeV}/c$.

- Pass 2: Exactly two tracks are required to pass the tight selection criteria ($p_T > 1.0\ \text{GeV}/c$, $|d_0/\sigma_{d_0}| > 3.5$, and one of the tracks $p_T > 1.5\ \text{GeV}/c$). If Pass 1 fails, Pass 2 is performed.

If either attempt is successful, the algorithm calculates the transverse distance (L_{xy}) from the primary vertex and the associated uncertainty ($\sigma_{L_{xy}}$). The sign of the transverse distance depends on the position of secondary vertex relative to the primary vertex along the direction of the jet. A jet is tagged if the vertex is significantly displaced as

$$L_{xy}/\sigma_{L_{xy}} \geq 7.5 \quad \text{(positive tag)} \tag{3.7}$$
$$L_{xy}/\sigma_{L_{xy}} \leq -7.5 \quad \text{(negative tag)} \tag{3.8}$$

The positive tag is consistent with a B-hadron traveling from the primary vertex in the direction of the jet, which is preferred in a true B-hadron decay. The negative tag happens by coincidence or as a result of mis-measured tracks due to the finite tracking resolution. The negative tagged jet is labeled a mis-tagged jet. Mis-tagged jets are useful for evaluating the rate of false positive tags. The algorithm also vetoes the events with following criteria:

- Pass 2 vertices found between 1.2 and 2.5 cm from the center of detector since these vertices are likely to come from material interactions in beam-pipe and L00.
- The vertices found more than 2.5 cm from the center of detector since the decay lengths are too large for genuine B-hadrons in our search channel.

The b-tagging efficiency is calculated as a function of jet E_T, jet η, and number of primary vertices as shown in Figure 3.1. The operation point used in this analysis is called "tight". The SECVTX b-tagging efficiency at the tight operation point is approximately 40%. Unfortunately, the b-tagging efficiency obtained from MC samples does not exactly reflect the data. Thus, this difference is compensated by taking a scale factor of $SF_{\text{btag}} = \epsilon_{\text{data}}/\epsilon_{\text{MC}}$ into account.

The scale factor is estimated by two methods, called electron method and muon method. Both methods use two jets event with $E_{T\text{ jet}} > 15$ GeV. One jet is required to be tagged by the SECVTX ("away" jet), and the other jet is required the existence of an electron with $E_T > 15$ GeV (electron jet) or a muon with $p_T > 8$ GeV/c (muon jet). The requirement of the electron/muon jet helps to improve the purity of the real b-jet using the semi-leptonic decay of the b-quark. Since double-tagged events are rarely faked, the tagging rate of the electron/muon jet allows a reasonable estimate of the tagging efficiency.

Then, the tagging efficiency is calculated as

$$\frac{N_+ - \alpha N_-}{N} \frac{1}{F_{\text{HF}}} \tag{3.9}$$

where $N_{+(-)}$ is the number of positive (negative) tagged jets, N is the total number of events, α is a mistag asymmetry factor, and the F_{HF} is the heavy flavor fraction in the away jet, respectively. The ratio of this quantity between data and MC is the scale factor.

By combining the electron and muon method, we obtain the scale factor for SECVTX as:

$$SF_{\text{SECVTX}} = 0.93 \pm 0.04 \tag{3.10}$$

The mistag rates of SECVTX are shown in Figure 3.2. The tight operation point is tuned to a low fake rate, typically 1-2%.

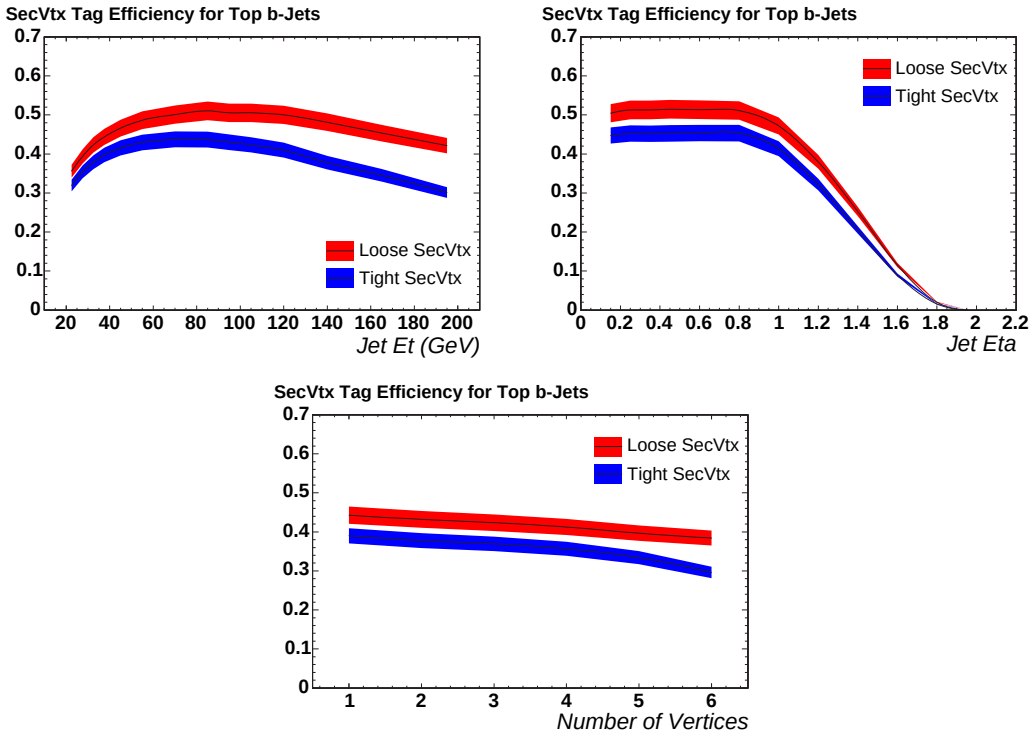

Figure 3.1: b-tagging efficiency of SECVTX as a function of jet E_T, jet η, and number of vertices. The operation point called tight is used for this analysis.

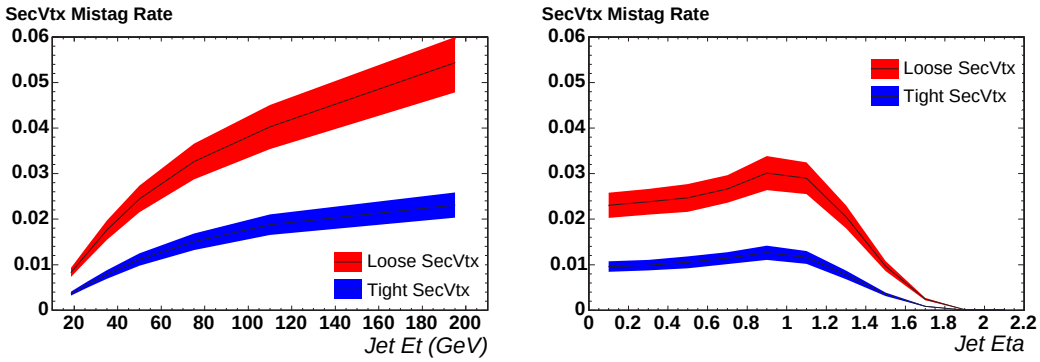

Figure 3.2: Mistag rates of SECVTX as a function of jet E_T and jet η. The rate is measured using inclusive jet data.

Jet Probability *b*-tagging

The JETPROB algorithm is used to determine whether a jet is produced promptly at the primary vertex, or from the decay of a long-lived particle. This algorithm makes use of the information of the tracks that are associated to a jet to determine the probability for this ensemble of tracks to be consistent with coming from the primary vertex. This probability is based on the impact parameters and their uncertainties of the tracks in a jet. The impact parameter of a track is assigned with a positive or negative sign depending on the direction of the track with respect to the jet axis. For the impact parameter in the $r-\phi$ plane, the sign is defined as: positive if cos$\phi > 0$, negative if cos$\phi < 0$, where ϕ is the angle between the jet axis and the track point of closest approach to the primary vertex (shown in Figure 3.3).

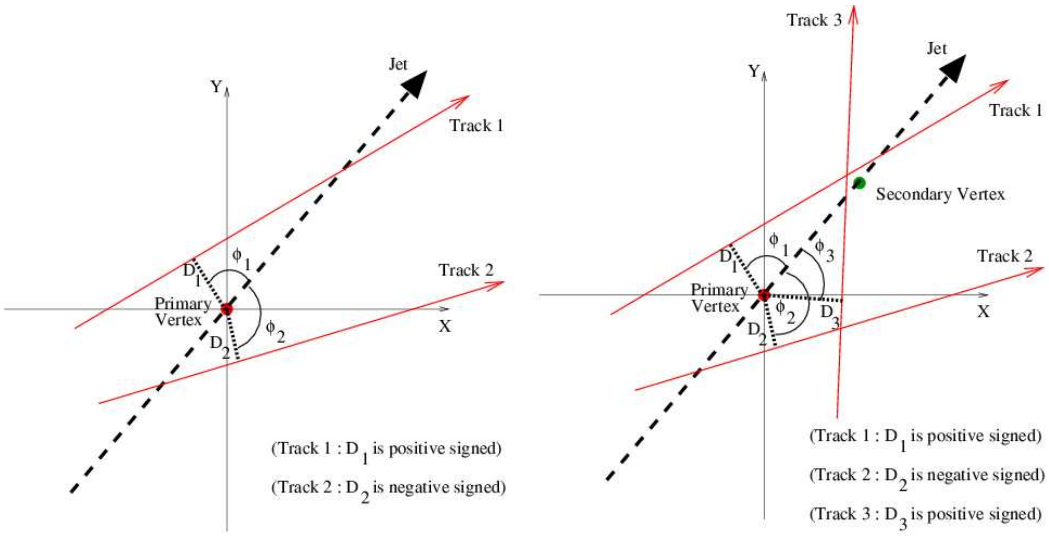

Figure 3.3: Tracks from a primary vertex (left) and from a secondary vertex (right).

For a primary jet, all its particles should come from the primary vertex. Due to the finite tracking resolution, these tracks are reconstructed with a non-zero impact parameter and have equal probability to be either positive or negative signed as shown in Figure 3.4 (left). On the other hand, a long-lived particle will travel some distance along the jet direction, and its decay products will preferentially have positive signed impact parameter (Figure 3.4 (right)).

The tracking resolution can be extracted from the data by fitting the negative side of the signed impact parameter distribution for primary jets. To minimize the contribution from poorly measured tracks having large reconstructed impact parameters, the distribution of signed impact parameter significances is employed. A quality cut on track is also applied for the tracks to be used in the tagging:

- track $p_T > 0.5$ GeV$/c$
- $|d_0| < 0.1$ cm
- more than 3 hits in the SVXII
- total number of COT axial hits ≥ 20
- total number of COT stereo hits ≥ 17

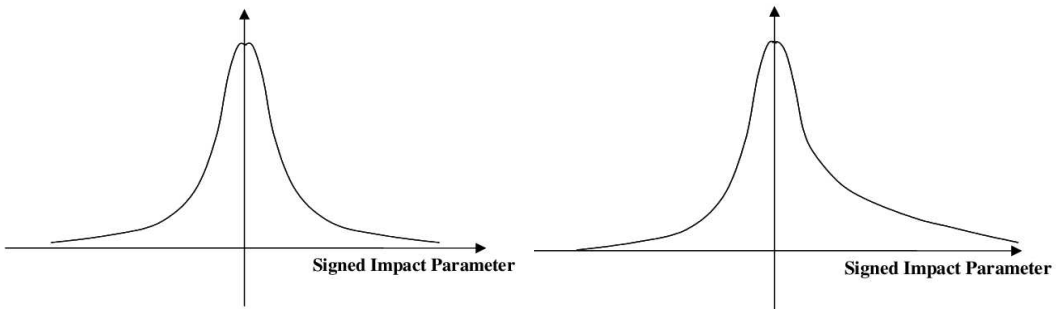

Figure 3.4: Signed impact parameter distribution. (Left) Tracks from primary vertex. (Right) Tracks from secondary vertex.

- z_0 of track within 5 cm of the primary vertex

We define a probability that a track in a jet comes from the primary vertex (Track Probability). While the tracks with negative signed impact parameters are used for calibration of the algorithm, only tracks with positive signed impact parameters are used in the tagging of b-jets. For a track with positive impact parameter, the track probability is calculated as follows: First, a signed impact parameter significance distribution for tracks in primary jets is extracted from a generic jet data sample. The positive part of the distribution is normalized so that the total area becomes 1. Then, for a given track, the track probability is defined as the area where the signed impact parameter of this track. By definition, this variable has a flat distribution between 0 and 1 for tracks in primary jets. However, it has a peak around 0 for tracks in heavy quark jets.

We then define a variable (Jet Probability) to characterize the probability of a jet coming from a primary vertex by combining the track probabilities (P_i) of the tracks in the jet. The jet probability is defined as

$$P_{\text{jet}} = \Pi \sum_{k=0}^{N-1} \frac{(-\ln\Pi)^k}{k!} \tag{3.11}$$

where

$$\Pi = P_1 P_2 P_3 \cdots P_N \tag{3.12}$$

The probability distribution of a primary jet is uniformly distributed between 0 and 1. For a long-lived jet, the distribution peaks at 0, meaning that the probability of such jet to be primary is small. Figure 3.5 shows simulated jet probability distributions for light flavor, charm, and bottom jets.

In this analysis, we use the JETPROB algorithm with a loose requirement, at a cut value of 0.05. In this operation point, the JETPROB b-tagging efficiency is approximately 33%. Similarly to the SECVTX scale factor, the JETPROB scale factor is obtained as:

$$SF_{\text{JETPROB}} = 0.79 \pm 0.04 \tag{3.13}$$

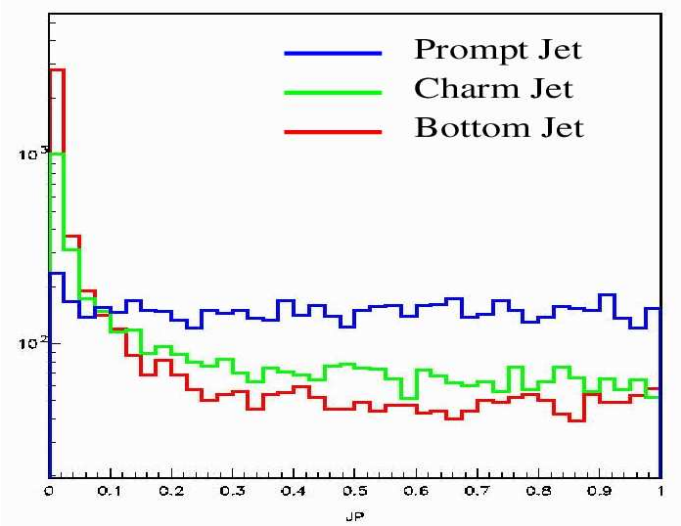

Figure 3.5: JETPROB distribution for jets matched to b, c, or light flavor jets.

Neural Network b-tagging

To further distinguish the b-jet signals from the light or charm flavor jets, we employ a neural network b-tagging algorithm (NN). A neural network tequnique is described in Section 6.1.1.

The NN algorithm starts from the collection of tracks lying inside a jet cone, and associates them to a series of vertices. Then, it gathers the jet observables to distinguish the flavor of the jet, which related to the identified vertices, any tracks inside the jet not associated to a vertex, and additional information from the SECVTX, JETPROB, and soft-muons b-tagging (the muons come from semi-leptonic decay of B-hadrons) [51].

The NN algorithm consists of a vertexing algorithm and three neural networks, vertex identification (Vertices NN), track identification (Tracks NN), and flavor identification. These neural networks are trained by the NeuroBayes package [52]. Figure 3.6 gives an overview of the information flow in the NN algorithm.

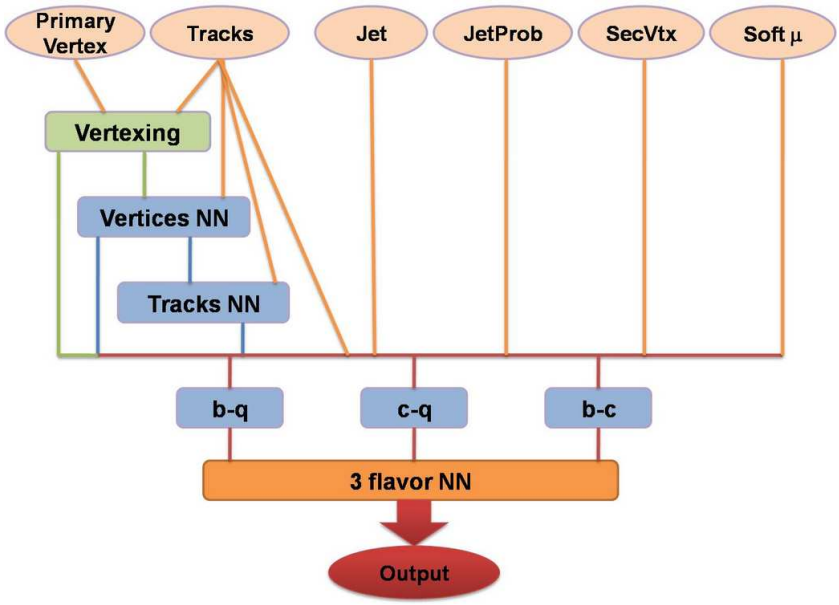

Figure 3.6: Flow chart of NN b-tagging algorithm.

The concept of the vertexing algorithm is similar to SECVTX, but this vertexing algorithm not only considers displaced tracks from the primary vertex but also uses tracks in the jet, and it allows the reconstruction of more than one vertex per jet (Figure 3.7). To choose the heavy flavor jets, the tracks outside the 0.15 cm (d_0) – 1.0 cm (z_0) window are not taken account. In addition to those requirements, we require a $p_T > 1.0$ GeV$/c$ and reject COT stand-alone tracks and silicon stand-alone tracks. We also reject tracks identified as originating from photon conversion. All vertex fits are performed by CTVMFT algorithm [53].

Once the vertices are found, the Vertices NN distinguish the primary vertex, the true displaced vertices originating from a long-lived particle, or the fake displaced vertices. It is trained with following five input variables:

- Track d_0 significance of the 2^{nd} highest p_T track
- Angle between vertex momentum (momentum sum of the tracks sharing the same vertex) and the vector pointing to the displaced vertex

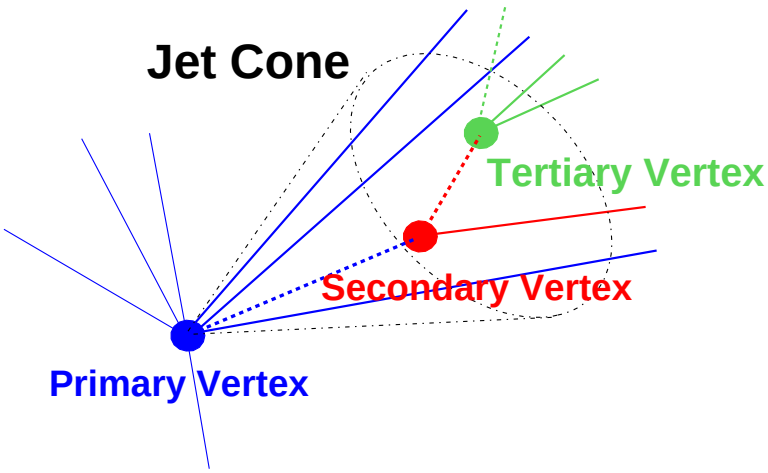

Figure 3.7: A sketch of the vertexing in NN algorithm.

- L_{xyz} (3-D) significance
- Invariant mass of tracks sharing the same vertex
- Vertex pseudo $c\tau$, derived using vertex mass and momentum

The distribution of the Vertices NN outputs is shown in Figure 3.8. The vertices originating from heavy flavors go to right (around $+1$), while other vertices go to left (around -1).

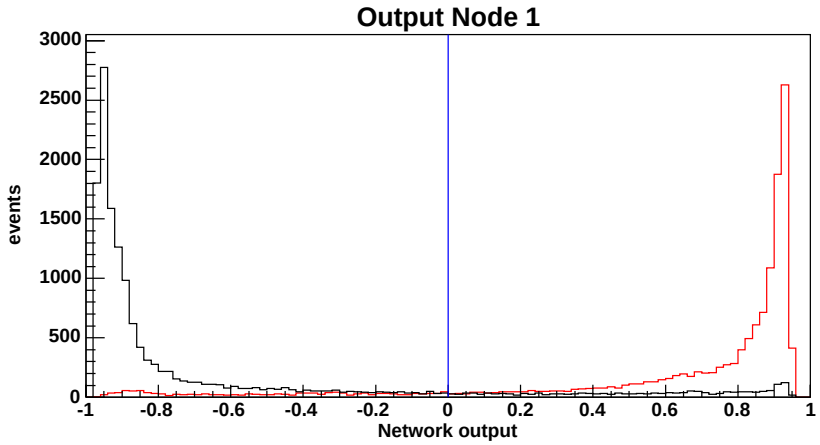

Figure 3.8: Output distributions of the Vertices NN (Monte Carlo simulation). Red: The vertices originating from heavy flavors. Black: The vertices originating from light flavors.

Some tracks from the B-hadrons decay often do not associated to any vertex. To recover such tracks which contain some information about the jet flavor, we employ the next neural network (Tracks NN). Tracks NN first collects the information from each unvertexed track and determines

that the tracks are from the heavy flavor decay or from the others. Following 5 variables are used as input variables:

- track d_0 significance (σ_{d_0})
- D/L
- Vertices NN output
- α
- D

where the definitions of D, L, and α are illustrated in Figure 3.9. The distribution of the Tracks

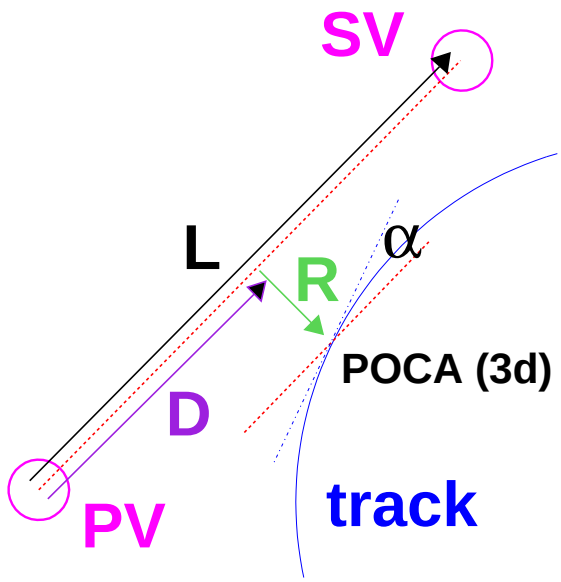

Figure 3.9: Definition of track selection observables. PV is the primary vertex. SV is the vertex with which the track is being examined. POCA is the "point of closest approach" (in 3D) of the track to the line L connecting the PV and SV.

NN outputs is shown in Figure 3.10.

The information from the two neural networks is combined with information from existing CDF b-tag algorithms SECVTX, JETPROB and soft-muons b-tagging. Combining with these information, we form flavor separation neural networks, which separate b-jets from light or c-jets. We choose following 16 variables as the input of the b-q, c-q, and b-c neural networks:

- Jet probability
- Pseudo $c\tau$ of the vertex with highest Vertices NN output
- SECVTX tag/untag information
- Number of muons inside the jet
- $\sum_{\text{all tracks}} p_T$

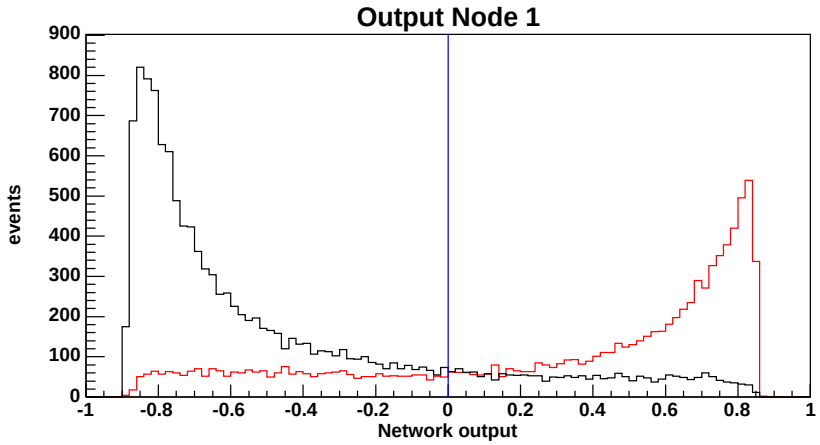

Figure 3.10: Output of the Tracks NN. Red: The unvertexed tracks originating from heavy flavors. Black: The unvertexed tracks originating from light flavors.

- $\sum_{\text{selected tracks}} p_T / \sum_{\text{all tracks}} p_T$, where selected track means Tracks NN output > 0.0
- L_{xyz} significance of vertex with highest Vertices NN output
- Invariant mass of vertex with highest NN
- Invariant mass of all selected tracks with Vertices NN output or Tracks NN output > 0.0
- Number of selected tracks with Tracks NN output > 0.0
- L_{xyz} of vertex with highest NN
- Number of tracks in jet
- L_{xyz} of vertex with second highest NN
- Highest p_T of muon
- Mass of secondary vertex
- Jet E_T

The output distributions of the networks are shown in Figure 3.11-3.13.

Finally, we combine three flavor separation NN outputs to a single network output. To separate the three inputs into two discrete training targets, we employ the TMultiLayerPerceptron package [54]. The output distribution of the network are shown in Figure 3.14. In this analysis, we define NN output with > 0.0 as a b-tagged jet. Similar to the SECVTX and JETPROB scale factors, we estimate a scale factor for NN tagged jets. Since the b-tagging performance of the final NN algorithm largely differs depending on existence of muon inside the jets, we separately parameterize the scale factor for the jets with and without an associated muon:

jets with an associated muon: $SF_{\text{NN btag}} = 0.885 - 0.0061 \times (E_T - 45) \pm 0.067$

jets without an associated muon: $SF_{\text{NN btag}} = 0.84 \times \frac{(0.877 - 0.0229 \times (N_{\text{vtx}} - 1.8))}{0.877} \pm 0.086$

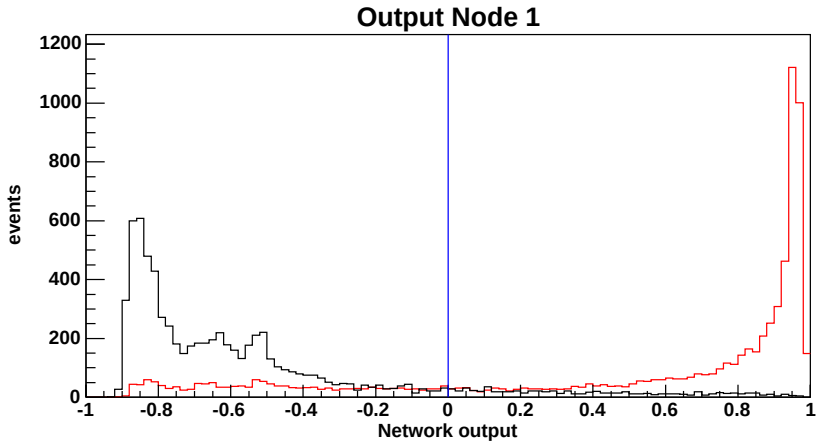

Figure 3.11: Output of the b-light jet NN. Red: b-jets. Black: Light flavor jets.

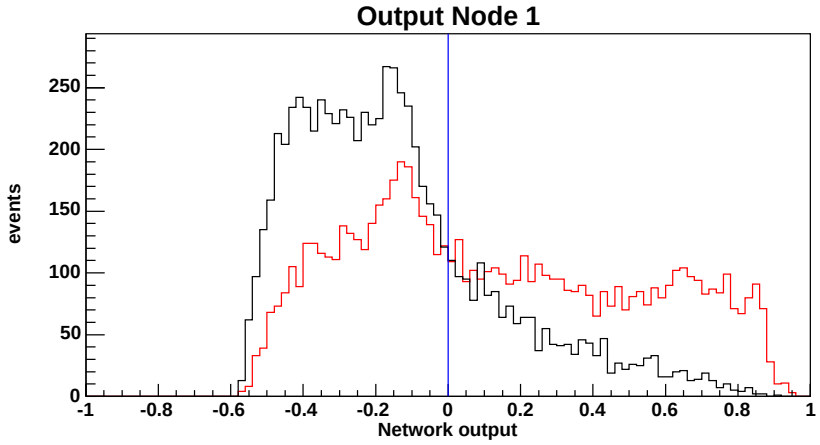

Figure 3.12: Output of the c-light jet NN. Red: c-jets. Black: Light flavor jets.

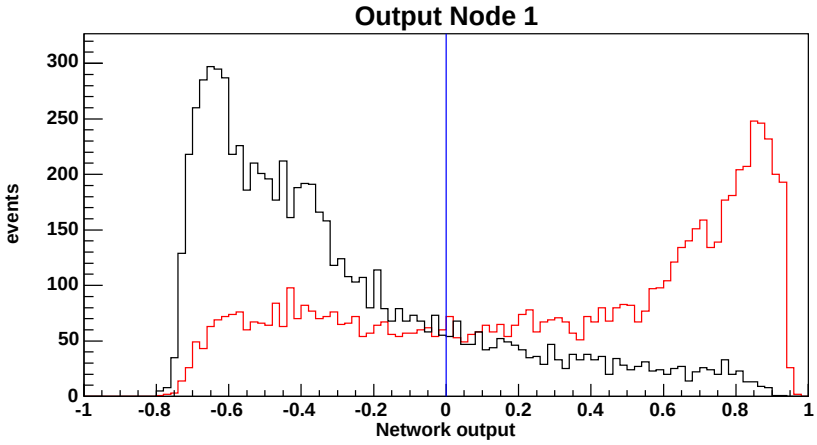

Figure 3.13: Output of the b-c jet NN. Red: b-jets. Black: c-jets.

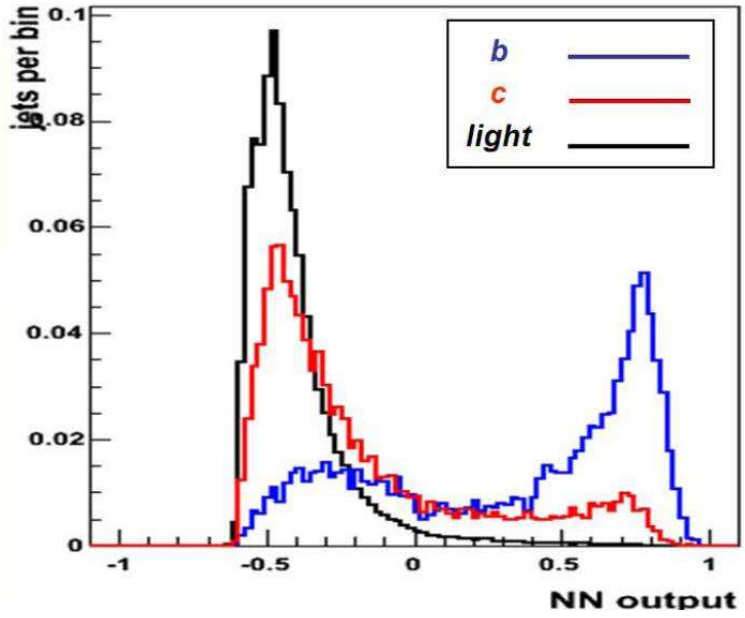

Figure 3.14: Output of the final NN.

Chapter 4

Event Selection

This chapter describes the selection of W + jets events which are subsequently used in the search for $WH \rightarrow \ell\nu b\bar{b}$. W + jets events are selected with the requirement of exactly one electron or muon candidate, large missing transverse energy, and two high E_T jets. Section 4.1 describes the trigger which is required in this analysis. The details of event selection are given in Section 4.2.

4.1 Trigger Requirements

Events considered in this analysis must first pass one of six specific trigger paths. The CDF trigger system is described in Section 2.2.5. The six trigger paths used in this analysis are ELECTRON_CENTRAL_18, MUON_CMUP18, MUON_CMX18, MET_PEM, MET2J, and MET45. The first three (Central lepton) are specifically designed to trigger on high-p_T central electrons and muons using a minimal set of identification cuts. The MET_PEM trigger (Plug electron) is designed to trigger on events with a high-energy electromagnetic object in the forward calorimeter region, such as an electron or photon, and $\not\!\!E_T$. The MET2J and MET45 triggers are designed to trigger on events with large $\not\!\!E_T$ and high-energy jets, or with only large $\not\!\!E_T$ requirement. These $\not\!\!E_T$ related triggers offer a chance to reconstruct WH events that are not caught by the high-p_T lepton triggers. In reconstructing $\not\!\!E_T$ triggered events, we require a high-p_T isolated track (Isolated track). As a result, we categorize each event into one of three categories: central leptons, plug electrons, and isolated tracks. The specific trigger requirements are given in the following sub-sections.

4.1.1 Central Lepton

ELECTRON_CENTRAL_18

The ELECTRON_CENTRAL_18 trigger path is designed to accept events which contain a high-p_T electron which enters the CEM. This trigger path consists of the following level 1, 2, and 3 requirements:

- L1_CEM8_PT8 requires a central EM cluster with a measured E_T of at least 8 GeV, the ratio $E_{\text{Had}}/E_{\text{EM}}$ to be less than 0.125, and an XFT track with $p_T > 8.34\ \text{GeV}/c$.
- L2_CEM16_PT8 additionally requires an EM cluster with an E_T of at least 16 GeV in the range $|\eta| < 1.317$.

- L3_ELECTRON_CENTRAL_18 requires an L_{shr} less than 0.4, the Δ_z between the COT track extrapolation and the CES shower location measurement to be less than 8 cm, $E_T > 18$ GeV, and a COT track with $p_T > 9$ GeV/c.

For this analysis, we use 4.31 fb^{-1} of central electron data.

MUON_CMUP18

The MUON_CMUP18 trigger path is designed to accept events that contain a high-p_T muon where a high-momentum track is associated with hits in both the CMU and CMP detectors. This trigger consists of the following level 1, 2, and 3 requirements:

- L1_CMUP6_PT4 requires an XFT track with $p_T > 4.09$ GeV/c pointing to the CMP fiducial region and a CMU stub with a track having $p_T > 6$ GeV/c.
- L2_CMUP6_PT8 additionally requires a 4-layer XFT track with $p_T > 8.34$ GeV/c which is fiducial to both the CMU and CMP detectors.
- L3_MUON_CMUP18 requires a COT track with $p_T > 18$ GeV/c whose extrapolation matches hits in the CMU and CMP detectors within $\Delta_{xCMP} < 20$ cm and $\Delta_{xCMU} < 10$ cm.

For this analysis, we use 4.31 fb^{-1} of CMUP muon data.

MUON_CMX18

The MUON_CMX18 trigger path is designed to accept events that contain a high-p_T muon with a high-momentum track pointing to hits in the CMX detector. This trigger consists of the following level 1, 2, and 3 requirements:

- L1_CMX6_PT8_CSX requires an XFT track with $p_T > 8.34$ GeV/c pointing to the CMX fiducial region, a CMX stub with a track having $p_T > 6$ GeV/c, and a hit in the CSX.
- L2_CMX6_PT10 additionally requires a 4-layer XFT track with $p_T > 10.1$ GeV/c.
- L3_MUON_CMX18 requires a COT track with $p_T > 18$ GeV/c with a stub in the CMX matching to its extrapolation within $\Delta_{xCMX} < 10$ cm.

For this analysis, we use 4.26 fb^{-1} of CMX muon data.

Trigger Efficiency

The triggers are very efficient, but they can not take events perfectly. Thus, we have to estimate trigger efficiency for each trigger path and apply this estimation to the Monte Carlo simulation. The trigger efficiency is estimated using the data triggered by a different trigger, applying the trigger selection cuts, and counting how often events are accepted by our target trigger path.

The followings are the estimated trigger efficiency used for this analysis.
The ELECTRON_CENTRAL_18 trigger efficiency is 96.8 $\pm$ 0.4%, the MUON_CMUP18 trigger efficiency is 88.4 $\pm$ 0.5%, and the MUON_CMX18 trigger efficiency is 91.0 $\pm$ 0.5%, respectively.

4.1.2 Plug Electron

MET_PEM

The MET_PEM trigger path is designed to accept events that contain a high-p_T electron which enters the PEM. Due to the higher background rate in the forward region, this trigger further requires a large $\not\!\!E_T$ to reduce the trigger rate. The missing transverse energy calculation used in the online trigger system is the vector sum of raw transverse energy over all calorimeter towers ($\not\!\!E_T^{\rm raw}$). The MET_PEM trigger consists of the following level 1, 2, and 3 requirements:

- L1_EM8_&_MET15 requires at least a central or plug calorimeter cluster with $E_T > 8$ GeV, $E_{\rm Had}/E_{\rm EM} < 0.125$, $\not\!\!E_T^{\rm raw} > 15$ GeV, and a minimum central and plug calorimeter ΣE_T of 1 GeV.
- L2_PEM20_L1_ EM8_&_MET15 additionally requires a plug calorimeter object with $E_T >$ 20 GeV in $1.1 < |\eta_{\rm det}| < 3.6$.
- L3_PEM20_MET15 additionally requires a plug calorimeter cluster using 3 towers with $E_T > 20$ GeV and $E_{\rm Had}/E_{\rm EM} < 0.125$.

For this analysis, we use 4.31 fb^{-1} of plug electron data.

Trigger Efficiency

The MET_PEM trigger path requires both the clusters in the plug calorimeter and the presence of large missing transverse energy. Since the requirements of this trigger are tighter compared to the offline selection (in Section 4.2.4), the trigger efficiency depends on an electron E_T and missing transverse energy. We model the dependency on electron E_T for level 2 and 3 trigger, and missing transverse energy for level 1 separately, by the function $\epsilon(x) = \frac{1}{1+e^{-\beta(x-\alpha)}}$. The resulting formula is

$$\frac{1}{1+e^{-\beta_1(\not\!\!E_T^{\rm raw}-\alpha_1)}} \cdot \frac{1}{1+e^{-\beta_2(p_T^{\rm ele}-\alpha_2)}} \cdot \frac{1}{1+e^{-\beta_3(p_T^{\rm ele}-\alpha_3)}} \tag{4.1}$$

where α_i and β_i is the turn-on parameter for the i level trigger. The Monte Carlo simulation is weighted event-by-event basis using this formula.

4.1.3 Isolated Track

The W + jets events which do not fire high-p_T triggers are reconstructed using the MET2J and MET45 triggers. The high-p_T lepton candidate in this category is reconstructed as an isolated track. The usage of MET2J trigger and MET45 trigger is described in the event selection section.

MET2J

The MET2J trigger path is designed to accept events that contain large missing transverse energy and at least two high-E_T jets. We choose the trigger called MET35_&_TWO_JETS which was later changed to MET35_&_CJET_&_JET. MET35_&_TWO_JETS was active from July 22, 2002, and through March 27, 2005. Then, its definition was changed to require one central jet ($|\eta_{\rm det}| < 1.1$) out of the two. The MET35_&_TWO_JETS and MET35_&_CJET_&_JET trigger paths consist of the following level 1, 2, and 3 requirements:

- L1_MET25 requires $\not\!\!E_T^{\rm raw} > 25$ GeV.

- L2_TWO_JET10_L1_MET25 requires two jet clusters of 10 GeV.
  The level 2 of MET35_&_CJET_&_JET trigger path additionally requires one central jet cluster with $|\eta_{\text{det}}| < 1.1$ and 20 GeV. Dynamically changing pre-scale (DPS) factor between 1 and 40 is also applied.

- L3_MET35 additionally requires $\not\!\!E_T^{\text{raw}} > 35\ \text{GeV}$.

In order to minimize dead-time in the data acquisition system, events corrected by this trigger path are randomly discarded with DPS factor at the level 2. The DPS factor shows how many events have to be produced in order for one event to be sent to the next trigger level. This factor decreases proportionally with the instantaneous luminosity. For this analysis, we use 3.95 fb^{-1} of MET2J triggered data.

MET45

The MET45 trigger path is designed to accept events that contain large missing transverse energy. The MET45 trigger path consists of the following level 1, 2, and 3 requirements:

- L1_MET25 requires $\not\!\!E_T^{\text{raw}} > 25\ \text{GeV}$.

- L2_MET35 requires $\not\!\!E_T^{\text{raw}} > 35\ \text{GeV}$.

- L3_MET45 requires $\not\!\!E_T^{\text{raw}} > 45\ \text{GeV}$.

For this analysis, we use 4.17 fb^{-1} of MET45 triggered data.

Trigger Efficiency

The trigger efficiency for the MET2J and MET45 trigger is estimated by the same methodology as the MET_PEM trigger. We parameterize the MET2J and MET45 trigger turn-on parameters for each trigger level separately as a function of the missing transverse energy. We measure the trigger turn-on following the procedure using events recorded with the MUON_CMUP_18 trigger. We define the trigger efficiency as the number of events passing the trigger requirements that fired the MET2J or MET45 trigger. The final efficiency is:

$$\frac{1}{1+e^{-\beta_1(\not\!\!E_T^{\text{raw}}-\alpha_1)}} \cdot \frac{1}{1+e^{-\beta_2(\not\!\!E_T^{\text{raw}}-\alpha_2)}} \cdot \frac{1}{1+e^{-\beta_3(\not\!\!E_T^{\text{raw}}-\alpha_3)}} \tag{4.2}$$

Same as the MET_PEM trigger, we weight the Monte Carlo simulation by this formula.

4.2 Event Selection

4.2.1 Baseline Selection

To select candidate events of the $WH \to \ell\nu b\bar{b}$ process, the following criteria are required:

- Trigger:
  Events must be triggered by the specific triggers as discussed in the previous section. The special treatment for the isolated track category is discussed in Section 4.2.5.

- Primary vertex position:
  The z-coordinate of the reconstructed primary vertex must be within 60 cm from the center of the detector.

- Presence of exactly one isolated lepton:
  The leptonic decay of W boson produces exactly one high p_T lepton, which must be identified. We require $p_T > 20$ GeV/c for the lepton candidate. If there exist more than one leptons, such events are rejected.

- Difference between the primary vertex and lepton track intercept:
  The difference $|z_{\text{track}} - z_0| < 5$ cm.

- Photon conversion veto:
  Discussed in electron identification section.

- Cosmic ray veto:
  Discussed in muon identification section.

- Z boson veto:
  If one of the leptons is not identified correctly, $Z \to \ell^+\ell^-$ events still remain. To remove such events, the invariant mass of the lepton and any track with opposite charge must not be in the Z boson mass window (76 – 106 GeV/c^2).

- Large missing transverse energy:
  $\not\!\!E_T > 20$ GeV ($\not\!\!E_T > 25$ GeV for PHX). The $\not\!\!E_T$ is corrected for the presence of muons (including muon-like isolated tracks) and jet energy correction.

- Jet:
  The jets are identified using the cone algorithm with a cone of 0.4 [48] and are required to be central ($|\eta| < 2.0$) with $E_T > 20$ GeV. We use exactly 2-jet events.

- QCD veto:
  To suppress the non-W QCD background, we apply specific cuts. The strategy of the QCD veto is described in each lepton selection section (Section 4.2.3 – 4.2.5).

- ***b*-tagging**: To increase the purity of b-tagged events, we require at least one SECVTX b-tagged jet. The strategy for b-tagging category is described in next section.

4.2.2 *b*-tagging Strategy

The b-tagging is a very powerful tool to reduce the predominant backgrounds, W+light flavor jets. Because a sample of events with two b-tagged jets is purer than a sample with only one, we adopt a b-tagging strategy that maximizes the number of events with two or more b-tags by making use of the SECVTX, JETPROB, and NN algorithms. Within our strategy, every event with at least one SECVTX b-tagged jet falls into one of four exclusive b-tagging categories, defined below:

SECVTX tight + SECVTX tight (ST+ST): Events in this category are required to have both jets tagged by the tight operating point of SECVTX.

SECVTX tight + Jet Probability 5% (ST+JP): Events in this category are required to have one jet tagged by the tight operating point of SECVTX and another jet to be tagged by the JETPROB algorithm. To be tagged, a jet must have a jet probability of less than 5%.

SECVTX tight + NN (ST+NN): Events in this category are required to have one jet tagged by the tight operating point of SECVTX and another jet to be tagged by the NN b-tagging algorithm. To be tagged, a jet must have a final NN output value greater than 0.0.

SECVTX tight (1-ST): Events in this category are required to have exactly one SECVTX tagged jet with the tight operating point and with no additional SECVTX, JETPROB, or NN tagged jet.

4.2.3 Central Lepton Selection

In addition to the baseline selection, we require following selections for central leptons. To reduce the non-W QCD background, we apply a QCD veto to the pre-b-tagged (pretag) and 1-ST events. This veto is not applied to the ST+ST, ST+JP and ST+NN categories. Specifically, we place the following cuts:

- CEM:
  - $m_T^W > 20$ GeV
  - $MET_{\text{sig}} \geq -0.05 m_T^W + 3.5$
  - $MET_{\text{sig}} \geq 2.5 - 3.125 \times \Delta\phi_{\not\!\!E_T, jet2}$
- CMUP, CMX:
  - $m_T^W > 10$ GeV

where m_T^W is the transverse mass of W boson and $\Delta\phi_{\not\!\!E_T, jet2}$ is the azimuthal angle between $\vec{\not\!\!E}_T$ and second leading jet. Here, MET_{sig} is defined as follows:

$$MET_{\text{sig}} := \frac{\not\!\!E_T}{\sqrt{\sum_{\text{jets}} C_{JES}^2 \cos^2(\Delta\phi_{\not\!\!E_T, jet1}) E_T + \cos^2(\Delta\phi_{vtx\not\!\!E_T, corr\not\!\!E_T})(\not\!\!E_T - \sum_{\text{jets}} E_T)}}, \tag{4.3}$$

where C_{JES} is jet energy correction factor; $\Delta\phi_{vtx\not\!\!E_T, corr\not\!\!E_T}$ is the azimuthal angle between corrected and uncorrected missing transverse energy directions.

4.2.4 Plug Electron Selection

In addition to the baseline selection, we require following selections for plug electrons. Because of the high non-W QCD contamination in the forward electron sample, we require stricter selection criteria for the plug electrons: $\not\!\!E_T > 25$ GeV and a QCD veto for all b-tagging categories:

- $MET_{\text{sig}} > 2.0$
- $\not\!\!E_T > 45 - 30 \cdot |\Delta\phi_{\not\!\!E_T, \text{jet1}}|$
- $\not\!\!E_T > 45 - 30 \cdot |\Delta\phi_{\not\!\!E_T, \text{jet2}}|$

4.2.5 Isolated Track Selection

In addition to the baseline selection, we require following selections for isolated tracks. We select high quality, high-p_T isolated tracks with $|\eta| < 1.2$ using the selection criteria described in Section 3.2.1.

We apply the following vetoes to ensure that isolated track events are from W events and that they are not double counted in other lepton categories.

- **Tight Lepton Veto**: If the event contains any CEM, CMUP, CMX, or PHX leptons, the event is not considered as an isolated track event.
- **Tight Jet Veto**: We veto isolated tracks with an angular separation $\Delta R < 0.4$ from any jets in the event.
- **Two Track Veto**: We count the number of isolated tracks in an event before applying the tight jet veto. If there are two or more counted isolated tracks, we veto the event.
- **QCD Veto**: A cut of $m_T^W > 10$ GeV is required for the pretag and 1-ST events to suppress the non-W QCD background contribution. This veto is not applied to the ST+ST, ST+JP and ST+NN categories.

Jets Trigger Requirements The previous studies have shown that the MET2J trigger requirements are fully efficient after the following cuts:

- Two jets with $E_T > 25$ GeV
- $\Delta R > 1.0$
- One of two leading jets with $|\eta| < 0.9$

We apply these additional jet cuts to the identified jets in the event. For jet count ≥ 3, we require that the two leading jets in the event satisfy these requirements. If any one of requirements failed, we consider that the event should belong to the orthogonal sample which requires the MET45 trigger. As a result, we have two exclusive isolated track categories, which are referred to as the MET2J and MET45 trigger samples.

Chapter 5

Background Estimation

In this chapter, the method of background estimation is discussed. The final signature of our signal, $WH \rightarrow \ell\nu b\bar{b}$, is one high-$p_T$ lepton, large $\not\!\!E_T$, and two b-jets. This signature is similar to the top-quark pair production having W + 4jets, thus we employ the methodology developed for the top-quark pair production analysis [45].

In the W + jets sample, the following background sources are considered:

Top Quark Backgrounds: This background comes both from single top quark production and top quark pair production. The final states include two b-jets, at least one charged lepton, and real $\not\!\!E_T$ from at least one high-p_T neutrino. This background is modeled based on a Monte Carlo simulation (MC) and estimated using the theoretical cross sections.

Electroweak Backgrounds: Additional small but non-negligible background contributions come from Z + jets production and diboson (WW, WZ, and ZZ) production. This background is modeled based on a MC and estimated using the theoretical cross sections.

Non-W QCD: A W-like signature is generated when one jet fakes a high p_T lepton and $\not\!\!E_T$ is generated through jet energy mismeasurement. This background is modeled using the sideband distribution in a QCD enriched data sample.

***W* + Mistags:** This background occurs when one or more light flavor jets produced in association with a W boson are mistakenly identified as a heavy flavor jet by the b-tagging algorithms. Mistags are generated because of the finite resolution of the tracking detectors, material interactions, or from long-lived light flavor hadrons (Λ and K_s) which produce real displaced vertices. This background is estimated using an inclusive jet sample.

***W*+ Heavy Flavor:** These processes ($W+b\bar{b}$, $W+c\bar{c}$, and $W+c$) involve the production of actual heavy flavor quarks in association with a W boson. This background is firstly estimated from a MC. Then, it is corrected accounting for a difference in the heavy flavor production in MC and the data. This correction factor is called k-factor.

Our background estimate begins in the W + jets sample before applying b-tagging requirement, which we call the "pretag" sample. Since this sample is dominated by the background and the signal contribution is negligible, we use the pretag sample as a sideband sample to determine the W + jets and non-W QCD normalization. Then, we extrapolate to the signal region after b-tagging requirement. The details for each background estimation are described in the following sections.

Theoretical Cross Sections	
WW	12.40 $\pm$ 0.25 pb
WZ	3.96 $\pm$ 0.06 pb
ZZ	1.58 $\pm$ 0.05 pb
Single Top s-channel	0.88 $\pm$ 0.11 pb
Single Top t-channel	1.98 $\pm$ 0.25 pb
$Z +$ jets	787.4 $\pm$ 85.0 pb
$t\bar{t}$	6.7 $\pm$ 0.8 pb

Table 5.1: NLO theoretical cross sections and uncertainties for the electroweak and top-quark backgrounds ($m_t = 175\ \mathrm{GeV}/c^2$).

5.1 Monte-Carlo Based Background Estimation

The top-quark and diboson backgrounds are estimated using PYTHIA [55] normalized to the next-to-leading-order (NLO) theoretical cross sections (Table 5.1). The contribution from production of single top quarks is estimated using MADEVENT [56] and PYTHIA normalized to the NLO cross section. The Z + jets background is estimated using ALPGEN [57] and PYTHIA normalized to the NLO cross section. The event acceptance and b-tagging efficiency are derived from MC. The acceptance is corrected in MC events for lepton identification, trigger efficiencies and z vertex cut. The tagging efficiency is always scaled by the data/MC scale factor as described in Sec. 3.2.4.

The expected number of selected events is obtained by the equation

$$N = \int \mathcal{L}dt \times \epsilon \times \sigma, \tag{5.1}$$

where ϵ is the total detection efficiency including all the relevant scale factors, σ is the cross section, and $\int \mathcal{L}dt$ is the integrated luminosity.

5.2 Non-W QCD

We estimate the non-W QCD fraction in the pretag and tagged samples by fitting background templates to the data $\not\!\!E_T$ distribution. The following sideband samples are used to produce the non-W QCD templates:

- CEM electron: The data sample where two or more of the five requirements shown in Table 3.1 are failed: $E_{\mathrm{HAD}}/E_{\mathrm{EM}}$, χ^2_{CES}, L_{shr}, $Q \times |\Delta_x|_{\mathrm{CES}}$, and $|\Delta_z|_{\mathrm{CES}}$
- CMUP and CMX muon: The data sample where the isolation requirement shown in Table 3.3 is failed.
- PHX electron: The data sample where two or more of the five requirements shown in Table 3.2 are failed: $E_{\mathrm{HAD}}/E_{\mathrm{EM}}$, PES $U_{5\times9}$, PES $V_{5\times9}$, PEM 3×3 Fit Tower, and $\chi^2_{3\times3\,\mathrm{PES}}$.
- Isolated track: The muon data sample where the isolation requirement is failed. For this template, we use the non-isolated muons in the CMU, CMP, or BMU detector. The non-isolated muons with CMUP detector are not taken account.

Figures 5.1 through 5.5 show the results of fitting the $\not\!\!E_T$ distribution in the pretag and tag regions. The fits in the double b-tagged samples suffer from low statistics, showing a uncertainty of 40%.

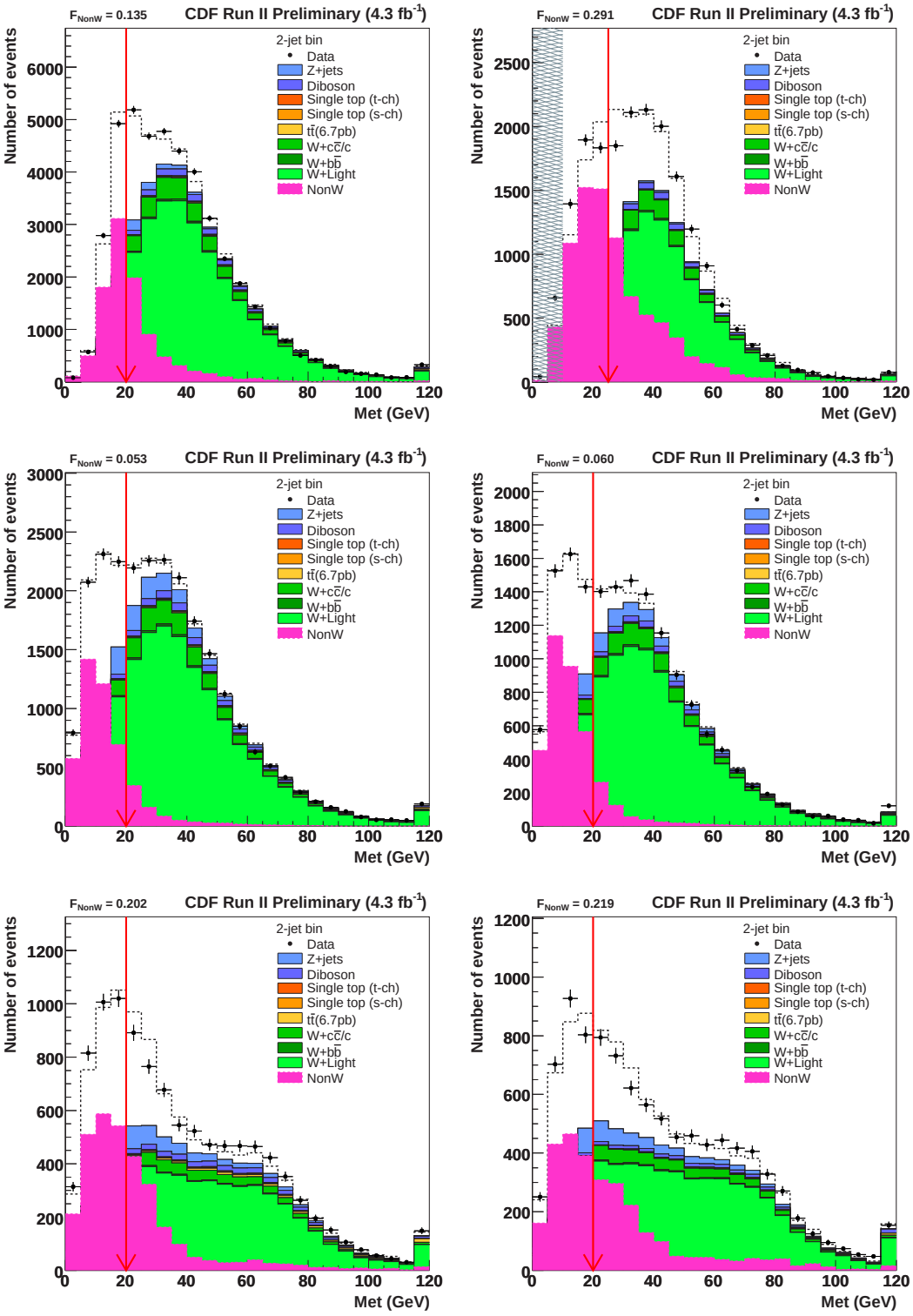

Figure 5.1: QCD fraction estimate for pretag 2-jet events. The figures represent (left to right and top to bottom) the CEM, PHX, CMUP, CMX, isolated track (MET2J), and isolated track (MET45) samples.

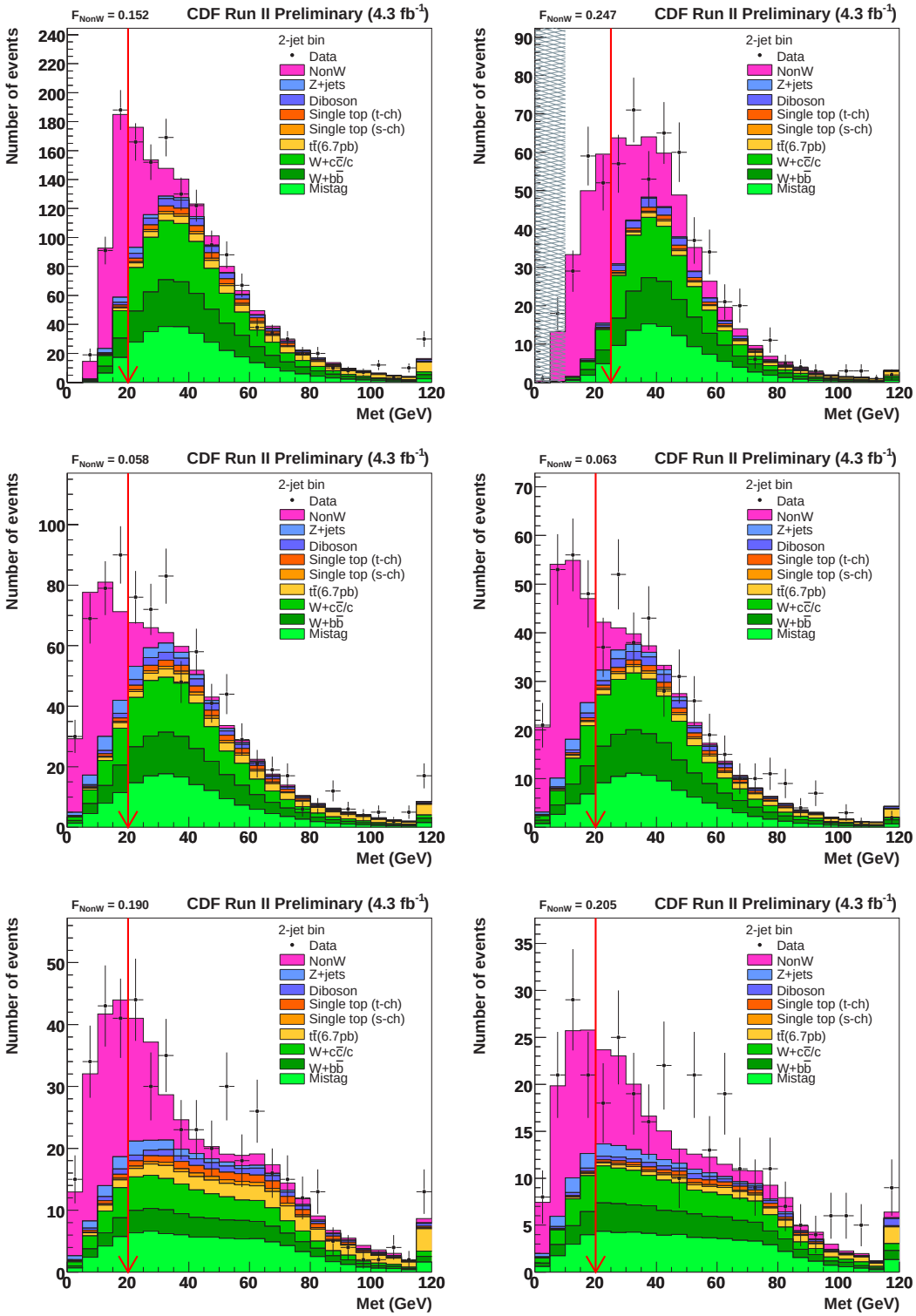

Figure 5.2: QCD fraction estimate for 1-ST 2-jet events. The figures represent (left to right and top to bottom) the CEM, PHX, CMUP, CMX, isolated track (MET2J), and isolated track (MET45) samples.

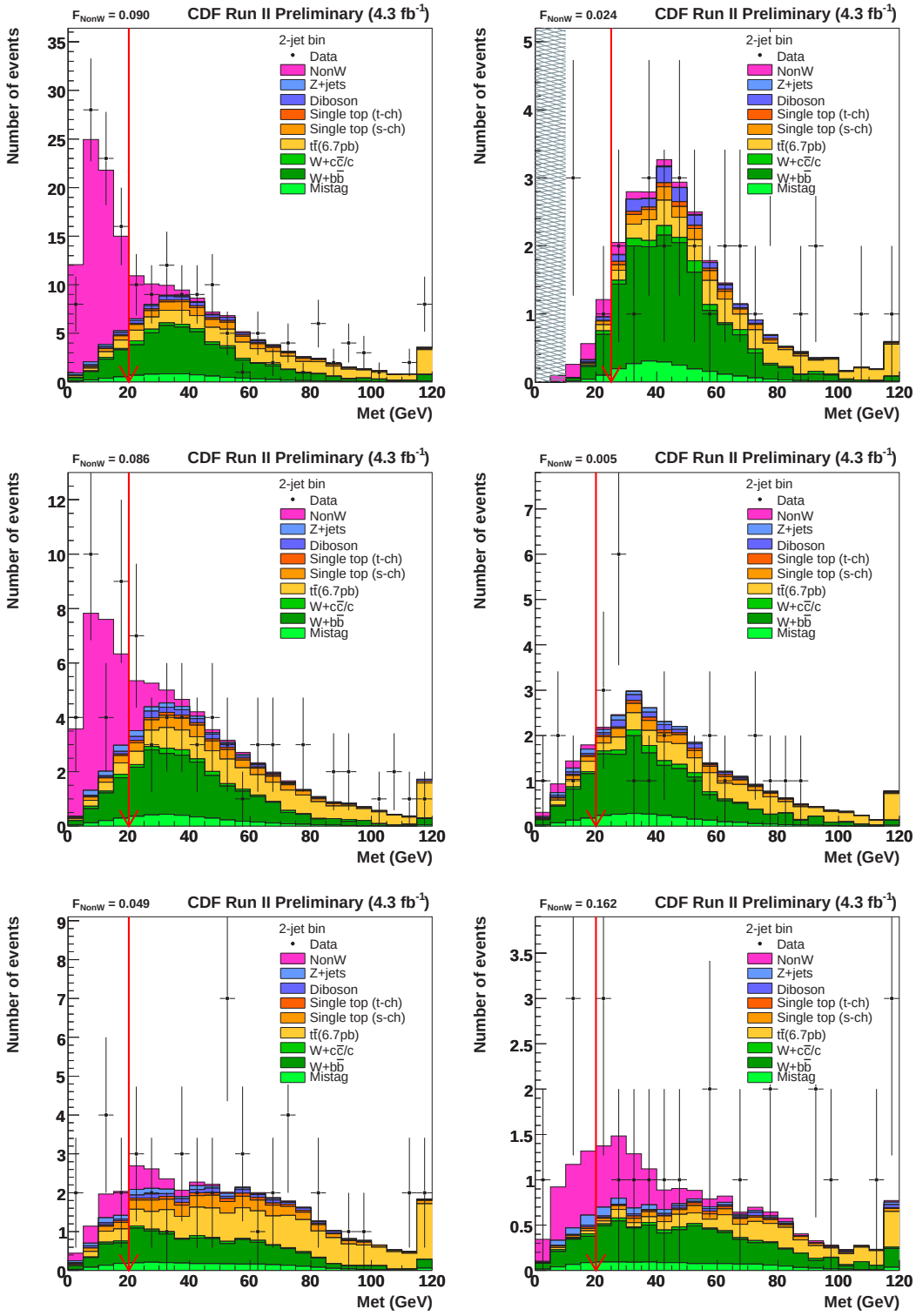

Figure 5.3: QCD fraction estimate for ST+ST 2-jet events. The figures represent (left to right and top to bottom) the CEM, PHX, CMUP, CMX, isolated track (MET2J), and isolated track (MET45) samples.

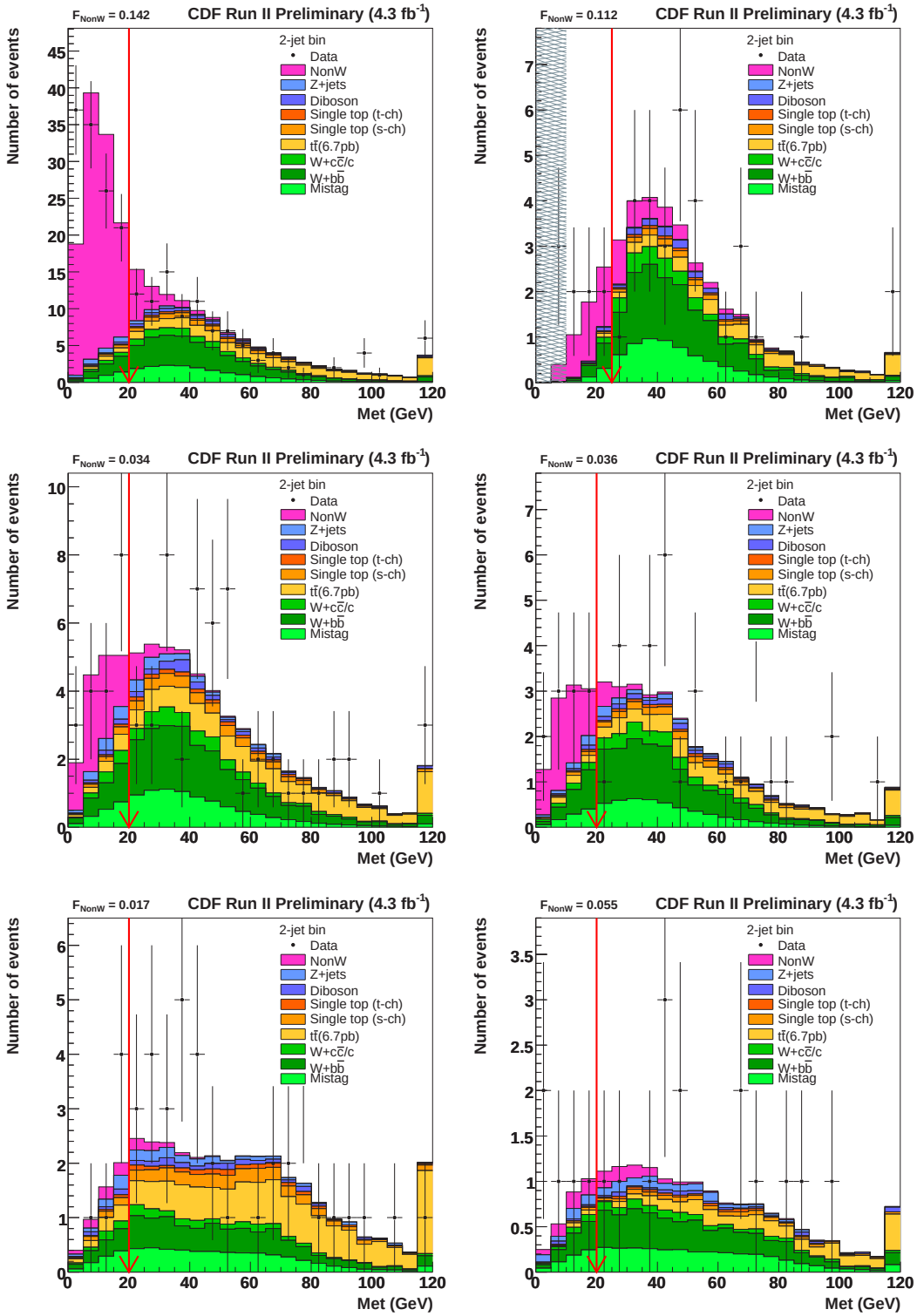

Figure 5.4: QCD fraction estimate for ST+JP 2-jet events. The figures represent (left to right and top to bottom) the CEM, PHX, CMUP, CMX, isolated track (MET2J), and isolated track (MET45) samples.

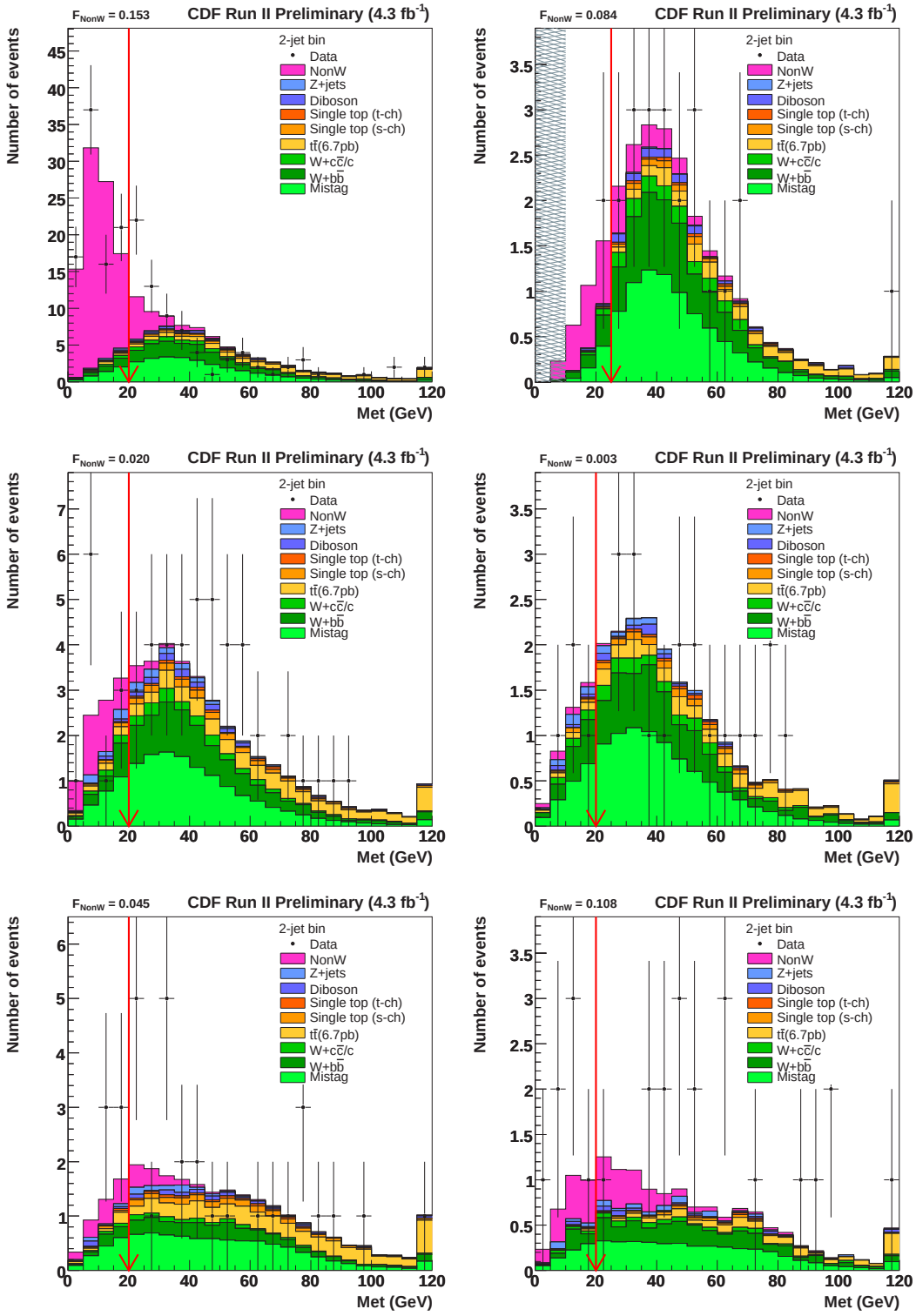

Figure 5.5: QCD fraction estimate for ST+NN 2-jet events. The figures represent (left to right and top to bottom) the CEM, PHX, CMUP, CMX, isolated track (MET2J), and isolated track (MET45) samples.

5.3 W + Heavy Flavor

The W + $b\bar{b}$, W + $c\bar{c}$, and W + c are major sources of background events in the W + heavy flavor jets channel. They are estimated firstly from the ALPGEN MC, then their overall rates are normalized to data. The contribution from true heavy flavor production in W + jet events is determined from measured W + jet events and the b-tagging efficiency for those events.

The heavy flavor fractions and an overall scaling factor for these fractions have been calibrated using W + 1 jet events from data. The scale factor (k-factor, or KF) to explain the difference between data and MC is measured. The k-factor is defined by

$$KF \equiv \frac{F^b_{j,data}}{F^b_{j,MC}}$$

where $F^b_{j,data}$ and $F^b_{j,MC}$ are the W+b-jets fractions in data and MC, respectively. $KF = 1.0$ is ideal, however, it is larger than 1.0 since ALPGEN MC could only treat the leading-order effect. To calibrate this k-factor, we convert it to

$$KF = \frac{F^b_{tag,data} \times F^{tag}_{j,data}}{F^{btag}_{j,MC} \times SF}$$

where SF is b-tagging scale factor, $F^{btag}_{j,MC}$ is the fraction of the b-tagged jets in the MC sample, $F^{tag}_{j,data}$ is the one in W + 1 jet events of data, and $F^b_{tag,data}$ is the fraction of correctly b-tagged jet in any tagged jet in W + 1 jet data events. We finally found a k-factor of 1.4 ± 0.4. We have calculated the tagging rates and heavy flavor fraction for events passing our selection. We estimate the number of W + heavy flavor events in our b-tagged samples according to

$$N_{W+HF} = f_{HF} \cdot \epsilon_{\rm tag} \cdot [N_{\rm pretag} \cdot (1 - f_{\rm non-}W) - N_{\rm top+EW}] \tag{5.2}$$

where f_{HF} is the heavy flavor fraction, $\epsilon_{\rm tag}$ is the tagging efficiency and $N_{\rm top+EW}$ is the expected number of $t\bar{t}$, single top, $Z+$ jets, and diboson events.

5.4 Mistags

The rate of W + mistags, or W + falsely-tagged jets, is derived from a sample of inclusive jet trigger data with no heavy flavor requirement. The mistag rate is obtained using a sample of *negatively-tagged* jets, which are b-tagged jets with there vertices measured behind the primary vertex, with respect to the momentum of the jet. The mistag rate obtained from negative tags is parameterized in bins of η, jet E_T, track multiplicity within the jet, $\sum E_T$ of the event, number of z-vertices, and the z-vertex position. The mistag rate derived from negative tags is corrected for the effects of heavy flavor in the jet sample, long-lived light-flavor secondary-vertices, and secondary-vertices caused by material interactions in the silicon detector. This correction is parameterized as a function of E_T to reduce its systematic uncertainty.

The total mistag rate is estimated from the pretag data. For each pretag event, the mistag probability for each jet is calculated, and the total mistag rate is estimated as the summation of the mistag probability over the number of jets and number of events:

$$N_{\rm mistag} = \sum_{n={\rm event}} \sum_{j={\rm jet}} \mathcal{P}^{\rm mistag}_j$$

We calculate the probabilities for that event to be singly or doubly tagged. The sum of the single-tag or double-tag probabilities over all pretag events provides the total mistag rate estimate. This estimate is then corrected for the fraction of the pretag events that come from other processes (non-W QCD, top production, Z + jets, or dibosons).

The mistag parameterization for SECVTX, JETPROB, and NN was derived using 4.1 fb^{-1} of data. It has been justified to apply the same parametrization through 4.3 fb^{-1} of data used in this analysis.

5.5 Background Summary

We have described the contributions of individual background sources in the final background estimate. The summary of the background estimates is shown in Tables 5.2 - 5.5. The numbers of expected and observed events are shown in Figures 5.6 - 5.9 as function of jet multiplicity. In these tables and plots, all lepton types are combined. In general, number of expected and observed events are in good agreement within the uncertainties.

Njet	2jet	3jet	>=4jet
Pretag Events	91437	16259	4609
Mistag	20.45 ± 8.85	17.21 ± 8.17	13.87 ± 8.17
$Wb\bar{b}$	108.52 ± 32.50	36.73 ± 11.07	12.21 ± 4.24
$Wc\bar{c}/c$	8.27 ± 2.42	4.31 ± 1.32	1.07 ± 1.14
$t\bar{t}$(6.7pb)	60.13 ± 9.15	165.55 ± 25.16	305.99 ± 46.65
Single top(s-ch)	20.52 ± 3.14	6.60 ± 1.01	1.88 ± 0.29
Single top(t-ch)	5.09 ± 0.79	4.38 ± 0.68	1.57 ± 0.25
WW	0.41 ± 0.04	0.48 ± 0.05	0.58 ± 0.06
WZ	7.62 ± 0.69	2.02 ± 0.19	0.50 ± 0.06
ZZ	0.24 ± 0.02	0.15 ± 0.01	0.06 ± 0.01
$Z + jets$	4.09 ± 0.57	2.58 ± 0.36	0.95 ± 0.13
non-W QCD	19.24 ± 8.48	9.12 ± 9.12	2.96 ± 2.96
Total background	254.58 ± 66.65	249.13 ± 61.03	341.65 ± 64.48
WH (115 GeV)	3.21	Control region	Control region
Observed Events	258	261	335

Table 5.2: Background summary table for ST+ST tag category. All lepton categories are combined. As a reference, the expected signal for $m_H = 115\ \mathrm{GeV}/c^2$ is also shown.

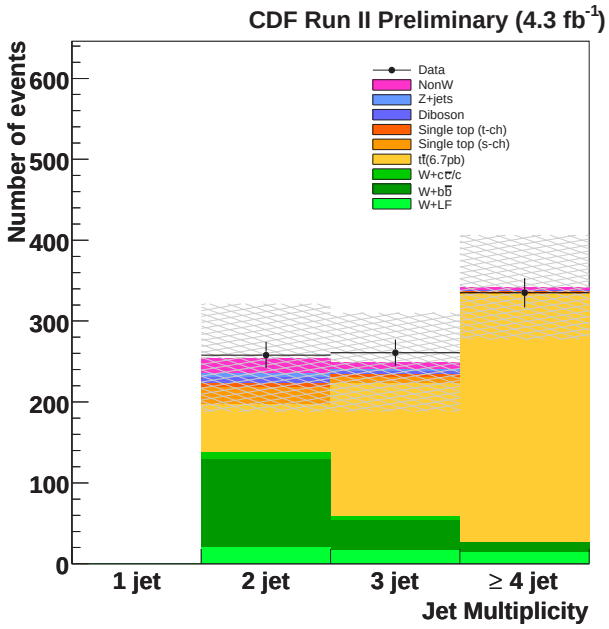

Figure 5.6: Number of expected and observed events for ST+ST tag category. All lepton categories are combined. Gray hash means total background uncertainty.

Njet	2jet	3jet	>=4jet
Pretag Events	91437	16259	4609
Mistag	53.08 ± 23.13	34.78 ± 16.89	23.08 ± 14.17
$Wb\bar{b}$	92.25 ± 28.66	30.62 ± 9.53	12.36 ± 4.43
$Wc\bar{c}/c$	23.61 ± 7.38	12.03 ± 3.85	6.20 ± 2.23
$t\bar{t}$(6.7pb)	55.17 ± 8.41	158.75 ± 24.18	286.57 ± 43.79
Single top(s-ch)	17.02 ± 2.61	5.91 ± 0.91	1.81 ± 0.28
Single top(t-ch)	6.12 ± 0.95	4.51 ± 0.70	1.54 ± 0.24
WW	2.82 ± 0.26	2.14 ± 0.21	1.41 ± 0.14
WZ	6.51 ± 0.60	2.12 ± 0.21	0.60 ± 0.07
ZZ	0.25 ± 0.03	0.14 ± 0.01	0.08 ± 0.01
$Z + jets$	7.16 ± 1.00	4.64 ± 0.65	1.83 ± 0.26
non-W QCD	21.81 ± 7.28	18.30 ± 6.18	6.65 ± 6.65
Total background	285.79 ± 80.31	273.93 ± 63.32	342.13 ± 73.02
WH (115 GeV)	2.62	Control region	Control region
Observed Events	264	266	344

Table 5.3: Background summary table for ST+JP tag category. All lepton categories are combined. As a reference, the expected signal for $m_H = 115\ \mathrm{GeV}/c^2$ is also shown.

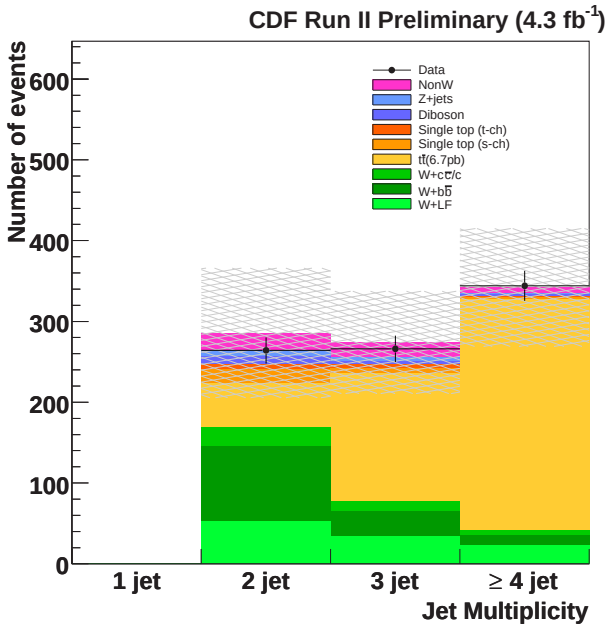

Figure 5.7: Number of expected and observed events for ST+JP tag category. All lepton categories are combined. Gray hash means total background uncertainty.

Njet	2jet	3jet	>=4jet
Pretag Events	91437	16259	4609
Mistag	77.43 ± 33.45	60.96 ± 29.23	49.45 ± 29.33
$Wb\bar{b}$	48.62 ± 22.77	17.64 ± 7.45	7.19 ± 3.81
$Wc\bar{c}/c$	12.46 ± 4.57	6.77 ± 2.51	3.32 ± 1.35
$t\bar{t}$(6.7pb)	25.81 ± 4.55	70.74 ± 12.44	119.62 ± 21.04
Single top(s-ch)	8.06 ± 1.42	2.70 ± 0.48	0.82 ± 0.15
Single top(t-ch)	2.96 ± 0.53	2.14 ± 0.38	0.68 ± 0.13
WW	1.86 ± 0.24	1.24 ± 0.16	0.70 ± 0.09
WZ	3.22 ± 0.41	1.02 ± 0.14	0.28 ± 0.05
ZZ	0.14 ± 0.02	0.08 ± 0.01	0.02 ± 0.01
$Z + jets$	3.39 ± 0.56	2.17 ± 0.36	0.94 ± 0.16
non-W QCD	17.65 ± 6.77	10.67 ± 5.59	2.98 ± 2.98
Total background	201.59 ± 75.29	176.14 ± 58.75	186.02 ± 71.49
WH (115 GeV)	1.22	Control region	Control region
Observed Events	204	160	171

Table 5.4: Background summary table for ST+NN tag category. All lepton categories are combined. As a reference, the expected signal for $m_H = 115\ \mathrm{GeV}/c^2$ is also shown.

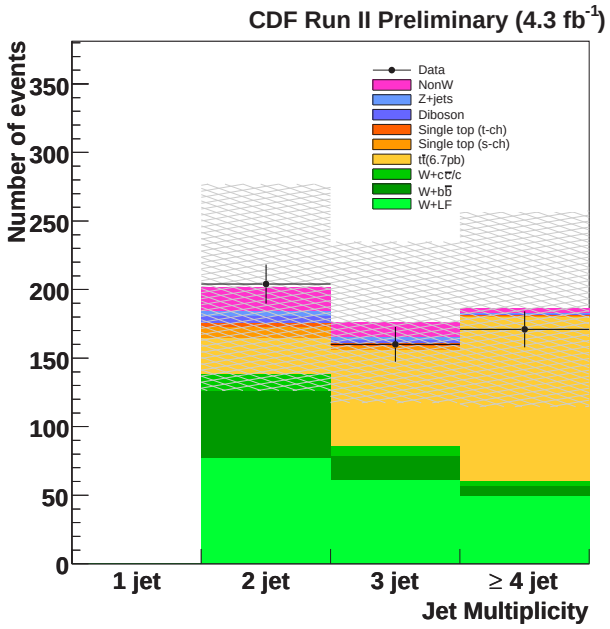

Figure 5.8: Number of expected and observed events for ST+NN tag category. All lepton categories are combined. Gray hash means total background uncertainty.

Njet	1jet	2jet	3jet	>=4jet
Pretag Events	481411	91437	16259	4609
Mistag	1877.74 ± 545.81	834.67 ± 361.78	236.22 ± 112.61	79.06 ± 46.92
$Wb\bar{b}$	1267.91 ± 372.64	643.81 ± 196.82	162.66 ± 50.83	46.08 ± 17.74
$Wc\bar{c}/c$	2158.47 ± 907.09	791.92 ± 348.03	189.03 ± 81.57	51.55 ± 25.73
$t\bar{t}$(6.7pb)	31.49 ± 4.57	195.03 ± 28.41	330.69 ± 48.16	367.96 ± 53.78
Single top(s-ch)	18.96 ± 2.77	42.16 ± 6.18	11.30 ± 1.66	2.68 ± 0.40
Single top(t-ch)	65.48 ± 9.62	97.01 ± 14.31	18.52 ± 2.74	3.30 ± 0.49
WW	33.88 ± 2.65	84.53 ± 6.61	22.34 ± 1.77	6.74 ± 0.55
WZ	17.96 ± 1.40	26.93 ± 2.09	6.76 ± 0.54	1.85 ± 0.16
ZZ	0.42 ± 0.04	0.96 ± 0.09	0.32 ± 0.03	0.14 ± 0.02
$Z + jets$	66.24 ± 8.71	62.68 ± 8.31	19.12 ± 2.54	5.42 ± 0.73
non-W QCD	576.38 ± 116.17	464.89 ± 82.36	140.74 ± 26.92	14.98 ± 14.98
Total background	6114.93 ± 1971.48	3244.60 ± 1054.98	1137.70 ± 329.37	579.76 ± 183.73
WH (115 GeV)	Control region	6.62	Control region	Control region
Observed Events	6046	3160	1113	609

Table 5.5: Background summary table for 1-ST tag category. All lepton categories are combined. As a reference, the expected signal for $m_H = 115$ GeV$/c^2$ is also shown.

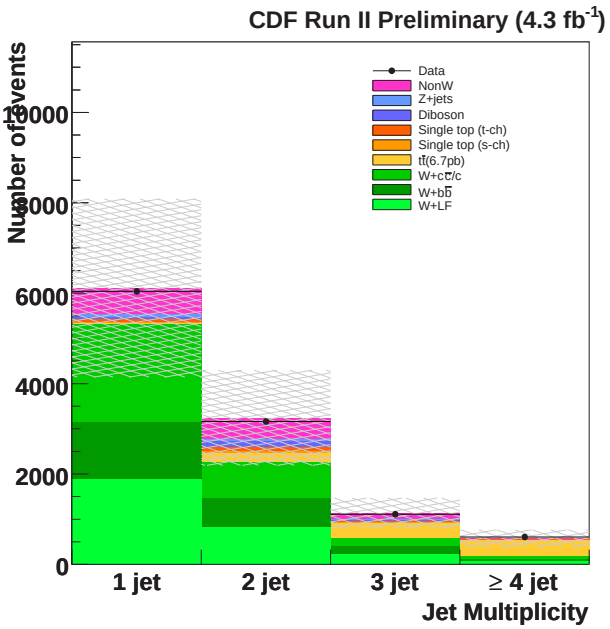

Figure 5.9: Number of expected and observed events for 1-ST tag category. All lepton categories are combined. Gray hash means total background uncertainty.

Chapter 6

Analysis Optimization

6.1 b-jet Energy Correction

The di-jet invariant mass resolution is a critical variable in this analysis. Improvement of the di-jet mass resolution directly results in improvement of the WH signal sensitivity. We develop a neural network b-jet energy correction method.

6.1.1 Neural Network Technique

The type of neural network used in this analysis consists of 3 "layers" which are made up of "nodes". Figure 6.1 shows an example of neural network structure. The first layer is called the "input" which are chosen by the user. In this analysis, the input variables to the input nodes are kinematic variables. The second layer is called "hidden" layer and every node in this layer is typically described by a sigmoid function which depends on the input variables:

$$h_j(x) = \frac{1}{1 + \exp(-\sum_i u_{ij} x_i)} \tag{6.1}$$

where u_{ij} is a weight for the j^{th} hidden node determined by the process called "training". The third layer is called "output" layer which includes one output node in our use. The output node is described as the linear combination of the hidden nodes as:

$$f(x) = \sum_j v_j h_j(x) \tag{6.2}$$

where v_j is a weight determined by the training.

A neural network is trained using known signal and background samples. For this analysis, we use the Monte Carlo simulation samples. In training, a neural network is given many variables as input for known events which it uses to determine the weights for each input connection in internal layers. The training is performed to minimize the error function:

$$E = \frac{1}{2}(f(x) - t)^2 \tag{6.3}$$

where t is the target value which can set free by user. For the purpose of signal-background separation, t is typically set as 1 for the signal and 0 or -1 for the background. For the neural network b-jet energy correction, t is a true value for each event.

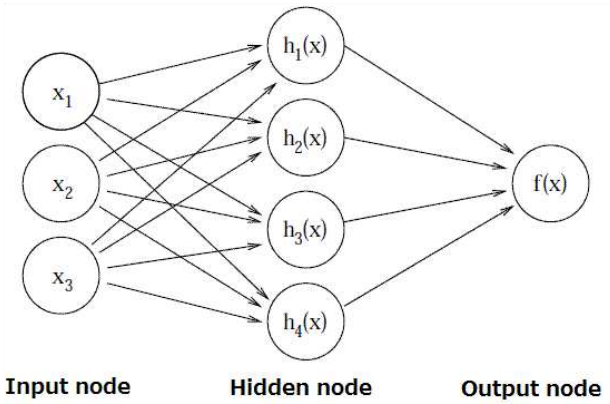

Figure 6.1: The schematic view of a typical neural network structure.

6.1.2 b-jet Energy Correction

We employ two neural network b-jet energy correction functions: one for SECVTX-tagged jets and another for non-SECVTX-tagged jets. Nine input variables are used for the SECVTX-tagged jet corrections:

- Jet E_T
- Jet p_T
- Raw jet E_T
- Transverse mass of the jet
- Decay length, L_{XY}, of the jet
- Uncertainty of the decay length, $\sigma(\mathrm{L}_{XY})$
- SECVTX p_T, momentum sum of the tracks sharing the secondary vertex
- maximum p_T of the tracks inside the jet
- $\sum p_T$ of all tracks inside the jet

For non-SECVTX-tagged jets, all variables above are used but L_{XY} and $\sigma(\mathrm{L}_{XY})$.

To validate the NN b-jet energy corrections, we use a sample of ST+ST events with at least 4 jets for the SECVTX-tagged correction, and a sample of 1-ST events with exactly two jets for the non-SECVTX-tagged correction.

Figure 6.2 shows the correction input variables for SECVTX-tagged jets, and Figure 6.3 shows the corresponding variables for non-SECVTX-tagged jets.

Applying NN corrections to b-jets in the Higgs decays improve the di-jet mass resolution from $\sim$15% to $\sim$11% for ST+ST tagged events, and from $\sim$17% to $\sim$13% for 1-ST tagged events. Figure 6.4 shows the di-jet mass resolution comparison before and after applying the NN b-jet energy correction for ST+ST tagged events (left) and for 1-ST tagged events (right), respectively. Figure 6.5 shows the di-jet invariant mass distributions after applying the NN b-jet energy correction for each b-tagging category.

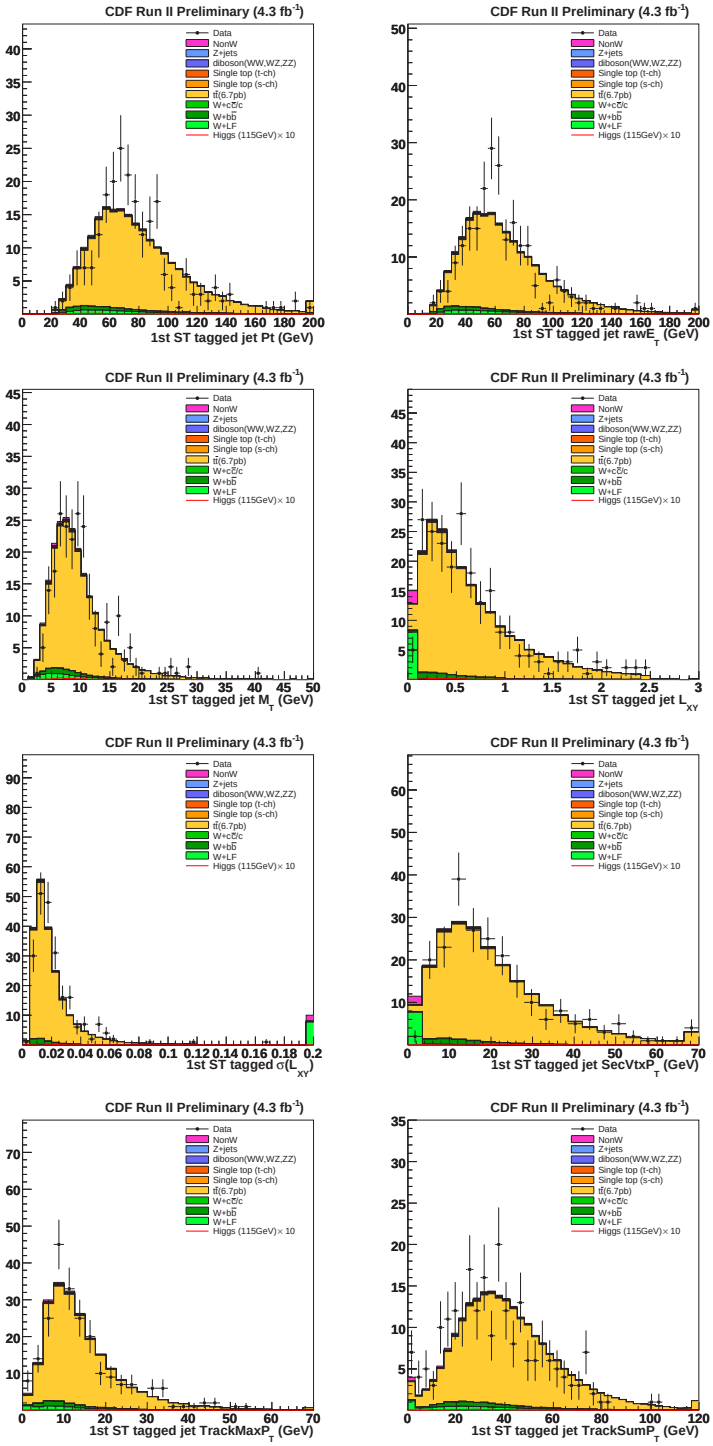

Figure 6.2: NN b-jet energy correction input variables for SECVTX-tagged jets. The figure represents a sample of central lepton ST+ST events with at least 4 jets.

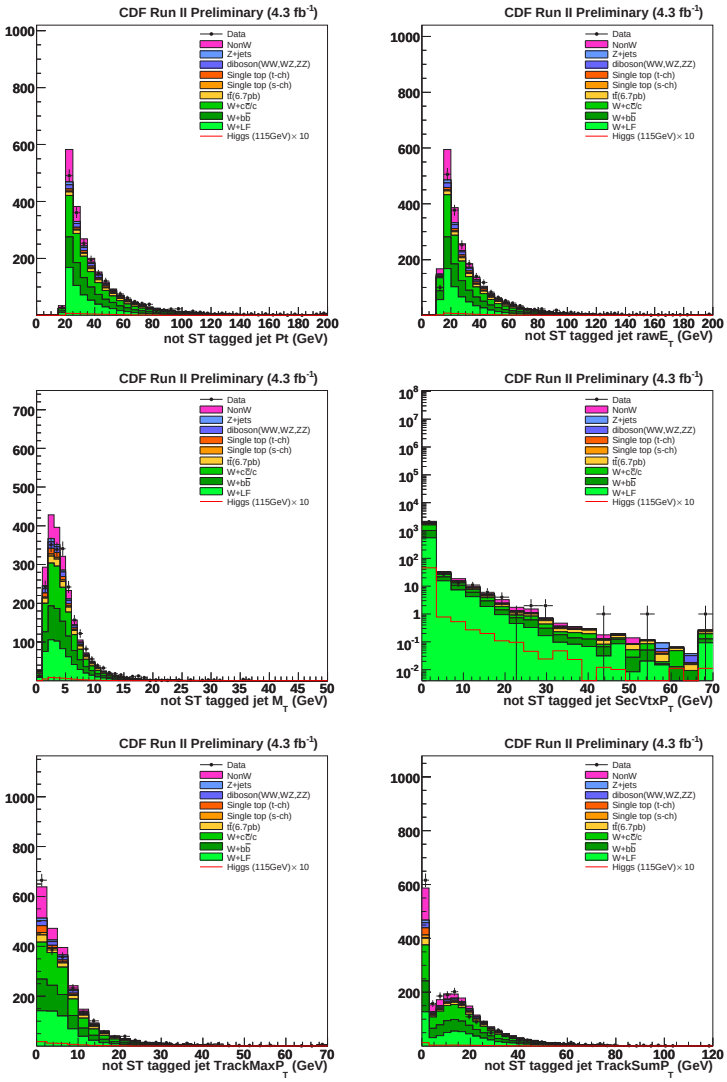

Figure 6.3: NN *b*-jet energy correction input variables for non-SECVTX-tagged jets. The figure represents a sample of central lepton 1-ST events with exactly two jets.

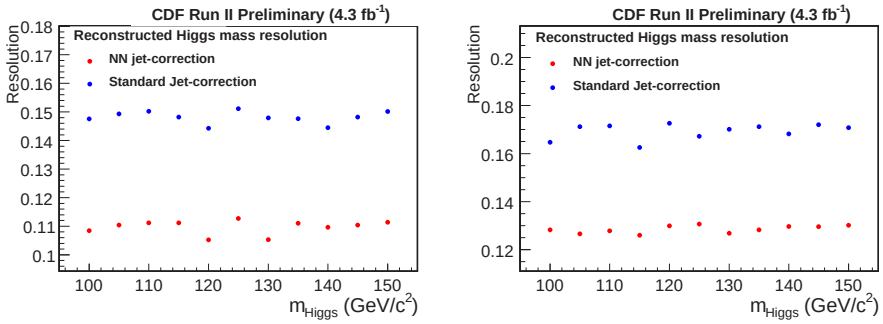

Figure 6.4: Higgs mass resolution for ST+ST tagged (left) and 1-ST tagged WH events as a function of generated Higgs mass.

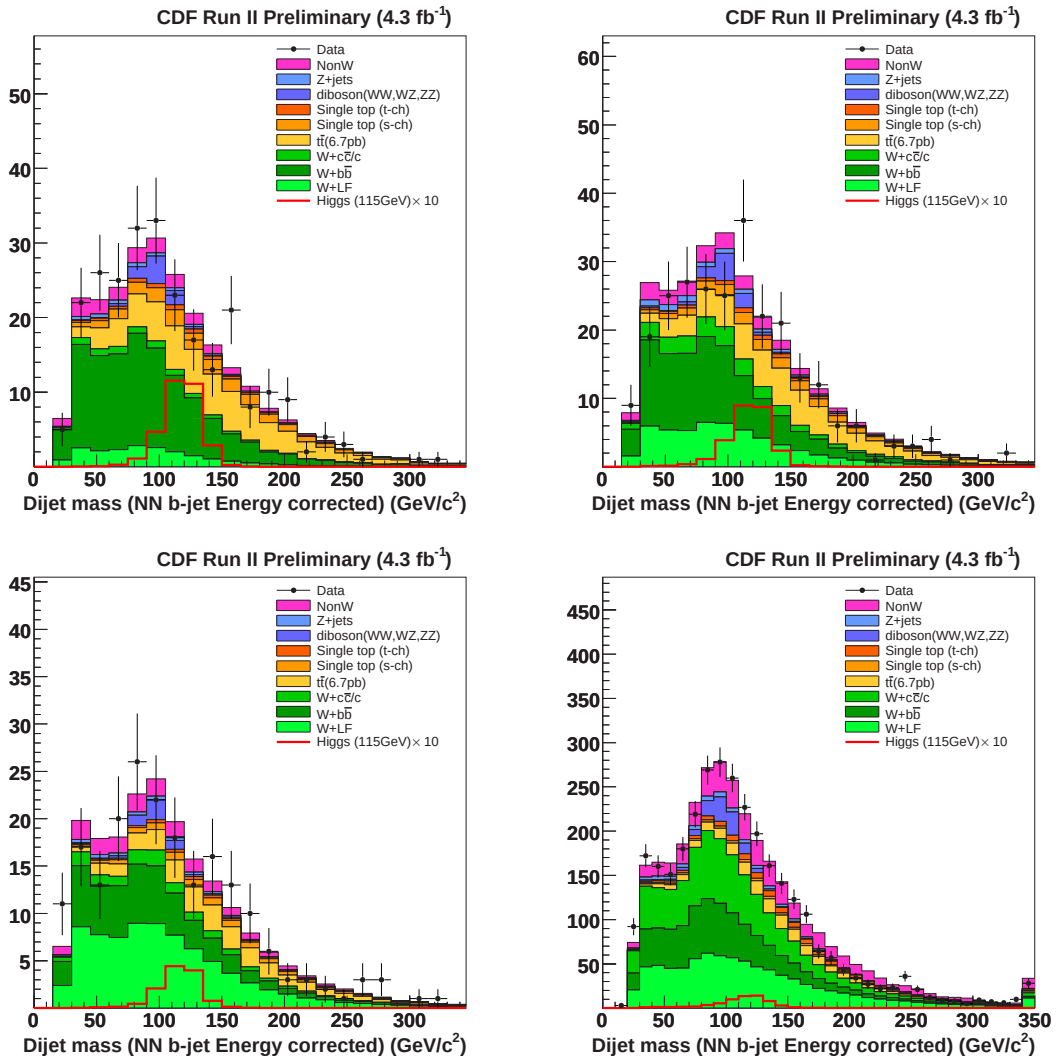

Figure 6.5: Di-jet invariant mass distributions after appealing the NN b-jet energy correction. From left to right and top to bottom, ST+ST, ST+JP, ST+NN and 1-ST b-tag category, respectively. All lepton types are combined. As a reference, the 10 times expected signal for $m_H = 115\ \mathrm{GeV}/c^2$ is also shown.

6.2 Bayesian Neural Network Discriminant

To further improve the signal-to-background discrimination, we employ a Bayesian neural network (BNN) [58, 59]. One advantage using BNN is less prone over-training because of the Bayesian sampling.

6.2.1 Bayesian Neural Network Technique

The idea of BNN is to determine the each weight as the posterior probability with the Bayes' theorem approach rather than to find one value just like general neural network. One advantage using BNN is less prone over-training because of the sampling of the posterior from the many networks.

In the Bayesian approach to neural network training, the weights u_{ij} and v_j are determined using training data $\{(t_1, x_1), \cdots, (t_N, x_N)\}$, where t_i is the target value and x_i is a set of input variables. The probability density assigned to point u_{ij} is given by Bayes' theorem

$$\begin{aligned} P(u_{ij}|t,x) &= \frac{P(t,x|u_{ij})P(u_{ij})}{P(t,x)} \\ &= \frac{P(t|x,u_{ij})P(x|u_{ij})P(u_{ij})}{P(t|x)P(x)} \\ &= \frac{P(t|x,u_{ij})P(u_{ij})}{P(t|x)} \end{aligned} \tag{6.4}$$

where we assume that x does not depend on u_{ij} and thus we can consider $P(x|u_{ij}) = P(x)$. According to the Equation 6.5, we need the likelihood $P(t|x, u_{ij})$ and the prior density $P(u_{ij})$ to determine a probability density to a neural network.

If a neural network is trained ideally, the probability that $t = 1$ (signal) is $f(x, u_{ij})$, and the $t = 0$ (background) is $1-f(x, u_{ij})$. The probability for the set of training data $\{(t_1, x_1), \cdots, (t_N, x_N)\}$ is

$$P(t|x,u_{ij}) = \prod_{k=1}^{N} f(x_k,u_{ij})^{t_k}(1 - f^{t_k}(x_k,u_{ij}))^{1-t_k} \tag{6.5}$$

where we assume the events to be independent. Then, for a given event x', an estimate is given by the weighted average

$$\begin{aligned} \bar{f}(x'|t,x) &= \int f(x',u_{ij})P(u_{ij}|t,x)\,du_{ij} \\ &\approx \frac{1}{K}\sum_{n=1}^{K} f(x',u_n) \end{aligned} \tag{6.6}$$

where $P(u_{ij}|t, x)$ is the posterior density given by Eq. 6.5.

6.2.2 Input Variables

For this analysis, we employ distinct BNN discriminant functions which are optimized for one of three tagging categories: ST+ST, ST+JP and ST+NN, and 1-ST. Once training is done, we perform a check for over-training by comparing the output shape for the training sample to that for a test sample which was generated using the same MC but not used in the training. Figure 6.6 shows examples of the over-training check for the Higgs mass of 115 GeV/c^2. We conclude that our neural network discriminant is not over-trained since the response for the training sample is in good agreement with that for the test sample.

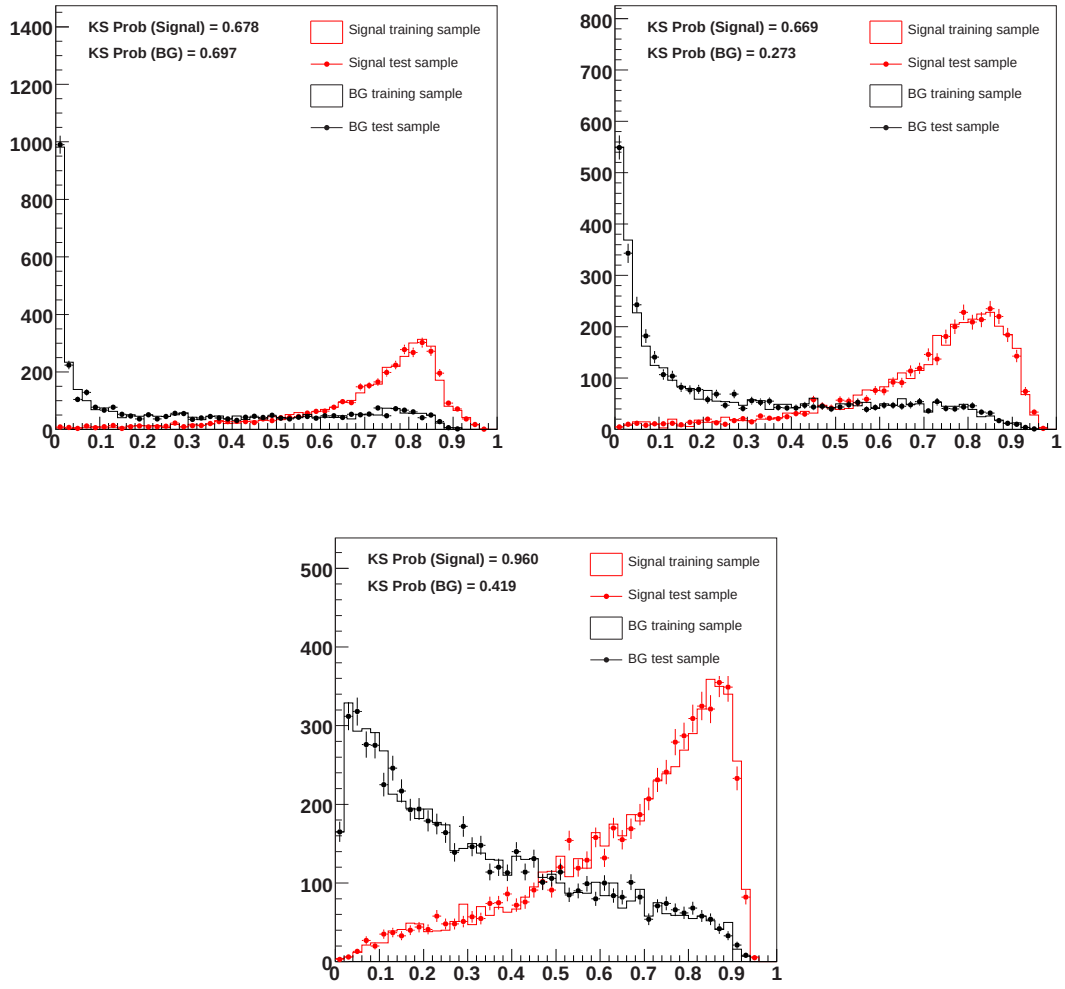

Figure 6.6: Examples of the output distribution for training and test samples of MC signal events generated with the Higgs mass of 115 GeV/c^2. From left to right and top to bottom, the BNN output for ST+ST, ST+JP/ST+NN and 1-ST BNN samples, respectively.

Discriminant for ST+ST *b*-tagging Category

The ST+ST BNN discriminant is optimized separately for each Higgs mass used in the search. This discriminant is trained to separate WH signal from top pair production, single top production (s-channel), and W + heavy flavor production. The input variables for the ST+ST BNN are listed below:

M_{jj}: the invariant mass calculated from the two tight jets with the NN b-jet energy correction applied.

p_T imbalance: the difference between $\not\!\!E_T$ and the scalar sum of p_T of lepton and two jets $p_T(\text{jet1}) + p_T(\text{jet2}) + p_T(\text{lep}) - \not\!\!E_T$.

$M_{l\nu j}^{max}$: the invariant mass of the lepton, $\not\!\!E_T$, and one of the two jets, where the jet is chosen to give the maximum invariant mass.

$Q_{lep} \times \eta_{lep}$: the charge of the lepton times the η of the lepton.

$\sum E_T$(Loose Jets): the scalar sum of the loose jet transverse energy. The loose jet is defined as: $E_T > 12$ GeV and $|\eta| < 2.4$. The nominal jets are not counted in this summation.

$p_T(W)$: the transverse momentum of the reconstructed W, computed as $\vec{p_T}(\text{lep}) + \vec{p_T}(\nu)$.

H_T: the scaler sum of the transverse energies $H_T = \Sigma_{\text{jets}} E_T + p_T(\text{lep}) + \not\!\!E_T$.

Figure 6.7 shows normalized shapes of the BNN outputs compared between signal and background MC events for the ST+ST sample.

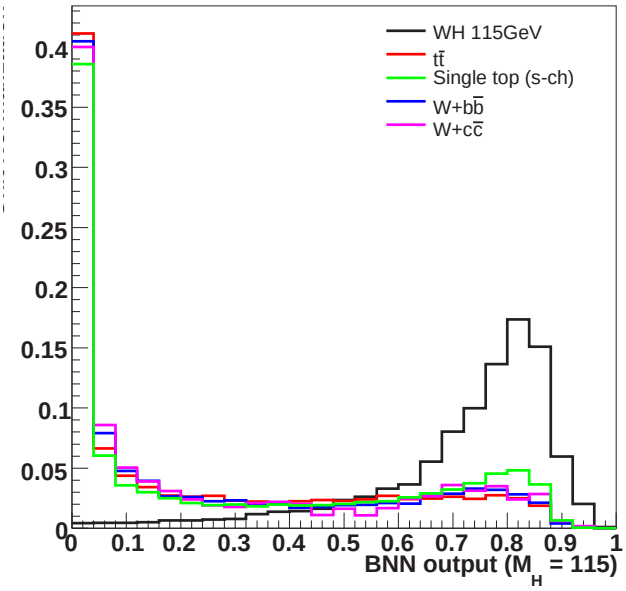

Figure 6.7: Comparison of the BNN output for signal and background events in the ST+ST sample. Each of signal and background histograms is normalized to unit area.

Discriminant for ST+JP/ST+NN *b*-tagging Category

The ST+JP and ST+NN BNN discriminants are optimized separately for each Higgs mass and trained with top pair production, single top production (s-channel), W + heavy flavor production, and W + light flavor production samples. The input variables for the ST+JP/ST+NN BNN are listed below:

M_{jj}**:** The same variable as is described for the ST+ST category.

$\sum E_T$**(Loose Jets):** The same variable as is described for the ST+ST category.

$Q_{lep} \times \eta_{lep}$**:** The same variable as is described for the ST+ST category.

$M_{l\nu j}^{min}$**:** This is the invariant mass of the lepton, $\not\!\!E_T$, and one of the two jets, where the jet is chosen to give the minimum invariant mass.

H_T**:** The same variable as is described for the ST+ST category.

$p_T(W)$**:** The same variable as is described for the ST+ST category.

$\not\!\!E_T$**:** Missing transverse energy.

Figure 6.8 shows normalized shapes of the BNN outputs comparing between signal and background MC events for the ST+JP and ST+NN samples.

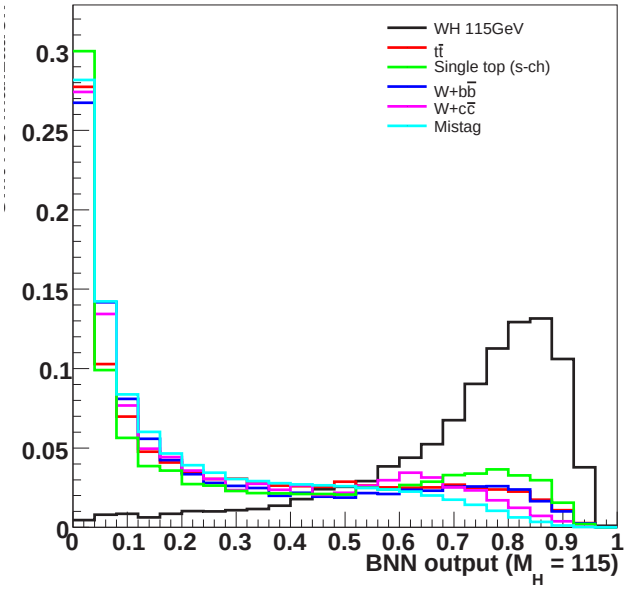

Figure 6.8: Comparison of the BNN output for signal and background events in the ST+JP/ST+NN samples. Each of signal and background histograms is normalized to unit area.

Discriminant for 1-ST *b*-tagging Category

The 1-ST BNN discriminant is optimized separately for each Higgs mass and trained with top pair production, single top production (s-channel, t-channel), W + heavy flavor production, and W + light flavor production samples. The input variables for the 1-ST BNN are listed below:

M_{jj}**:** The same variable as is described for the ST+ST category.

$\sum E_T$**(Loose Jets):** The same variable as is described for the ST+ST category.

$Q_{lep} \times \eta_{lep}$**:** The same variable as is described for the ST+ST category.

$p_T(W)$**:** The same variable as is described for the ST+ST category.

H_T**:** The same variable as is described for the ST+ST category.

$\not\!\!E_T$**:** The same variable as is described for the ST+JP/ST+NN category.

p_T **Imbalance:** The same variable as is described for the ST+ST category.

Figure 6.9 shows normalized shapes of the BNN outputs comparing between signal and background MC events for the 1-ST samples.

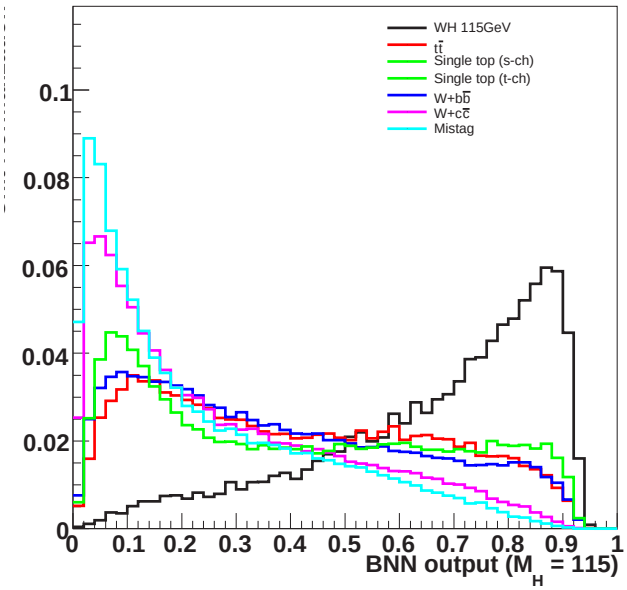

Figure 6.9: Comparison of the BNN output for signal and background events in the 1-ST sample. Each of signal and background histograms is normalized to unit area.

6.2.3 Background Modeling Validation

The BNN output distributions and kinematic distributions for all discriminant input variables have been thoroughly examined to establish a proper modeling. The modeling validations for the BNN input variables are performed using pretag events and shown in Figures 6.10 through

6.14. The pretag BNN output distributions for each lepton category are shown in Figure 6.16 for $m_H = 115\ \mathrm{GeV}/c^2$. The BNN output distributions for each b-tag category are shown in Figure 6.17 for $m_H = 115\ \mathrm{GeV}/c^2$. The modeling validations for the other basic kinematics are shown in Appendix B.

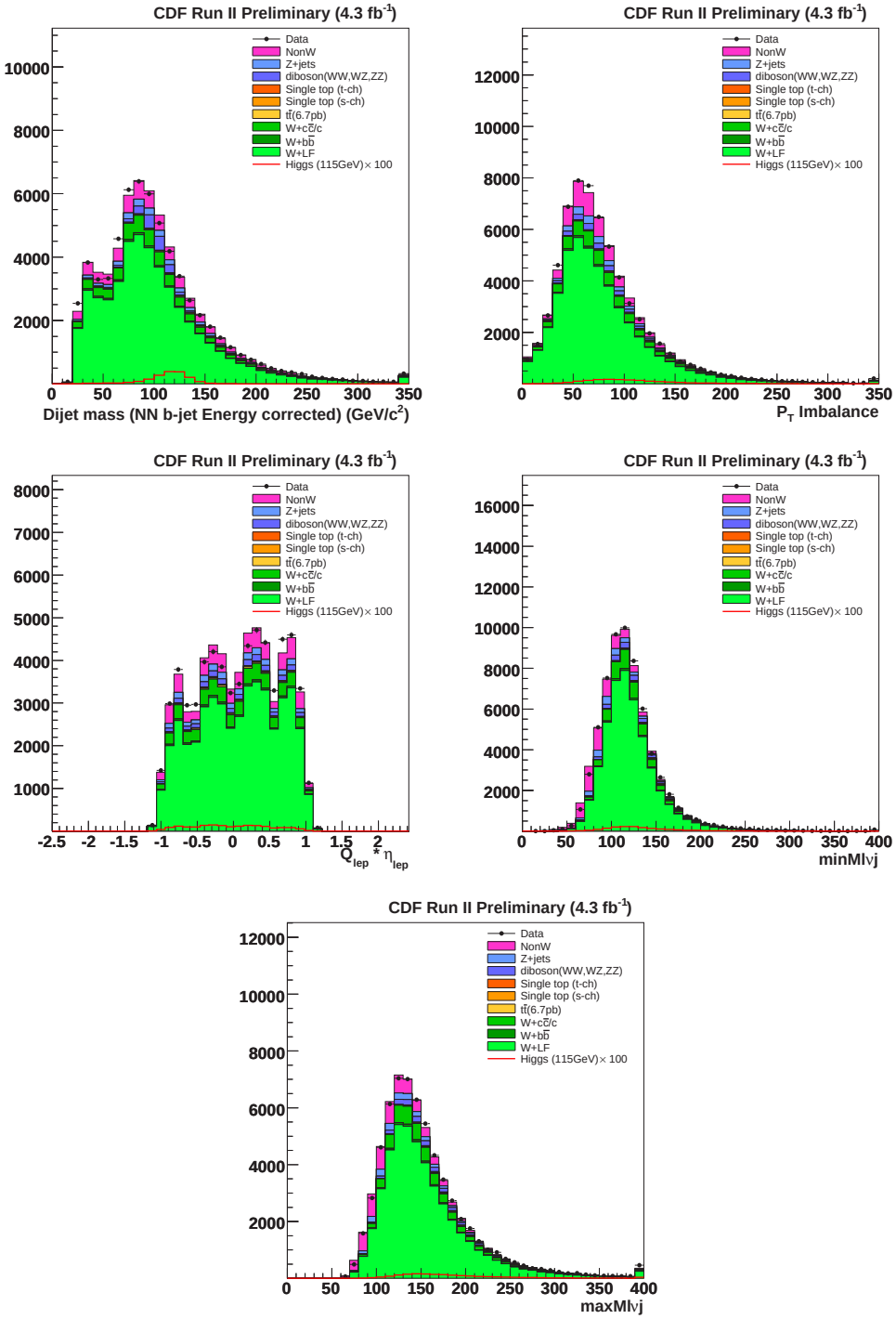

Figure 6.10: Central lepton pretag BNN inputs kinematics (1)

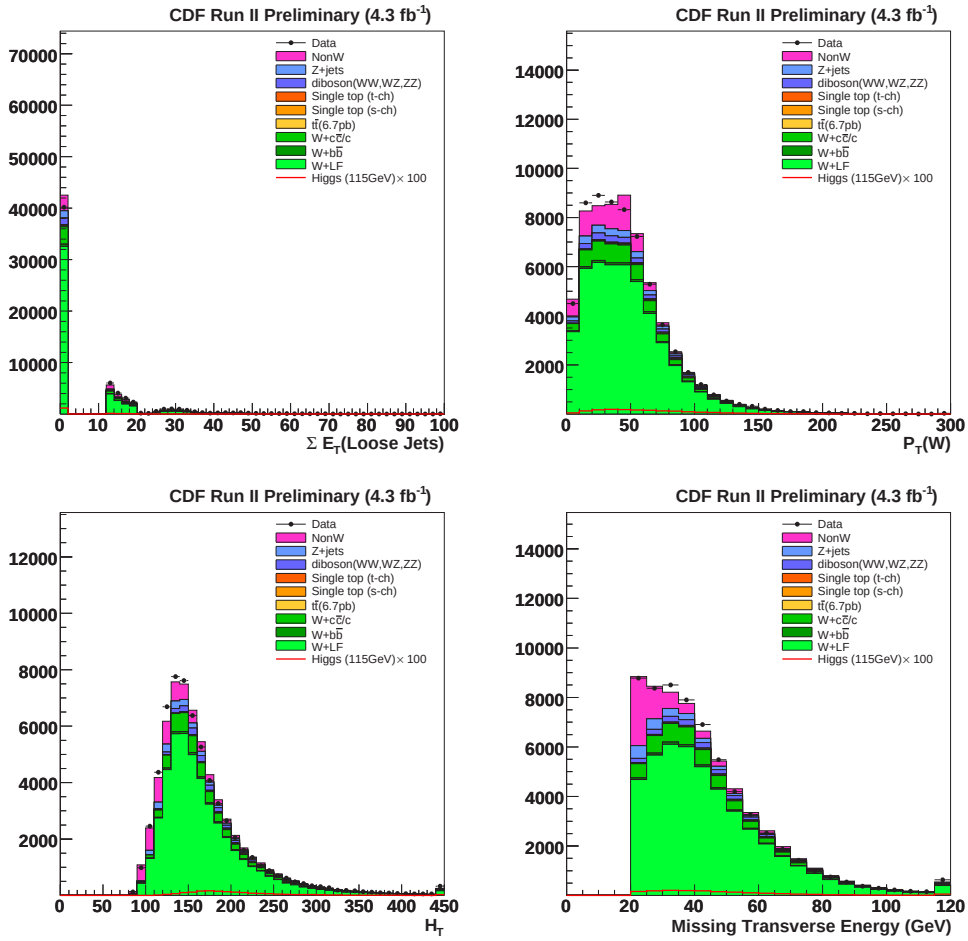

Figure 6.11: Central lepton pretag BNN inputs kinematics (2)

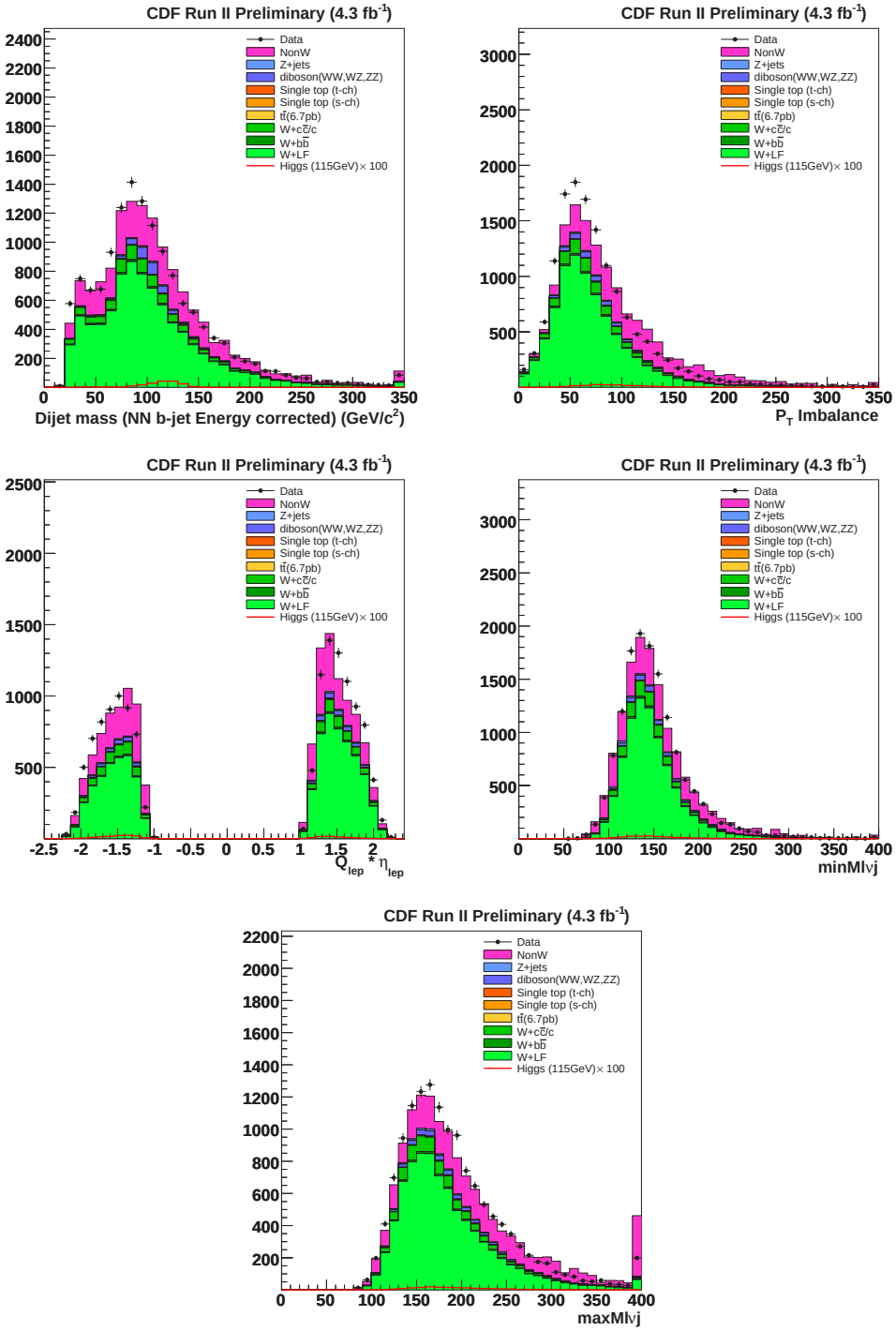

Figure 6.12: Plug electron pretag BNN inputs kinematics (1)

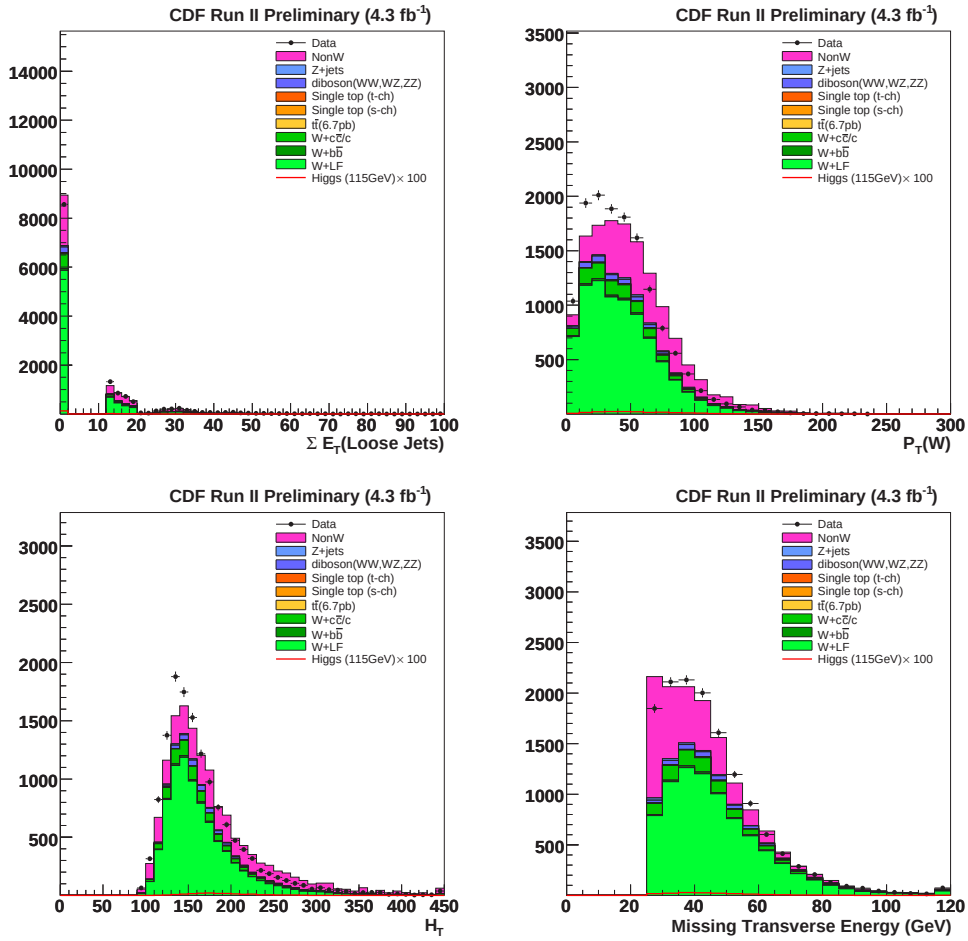

Figure 6.13: Plug electron pretag BNN inputs kinematics (2)

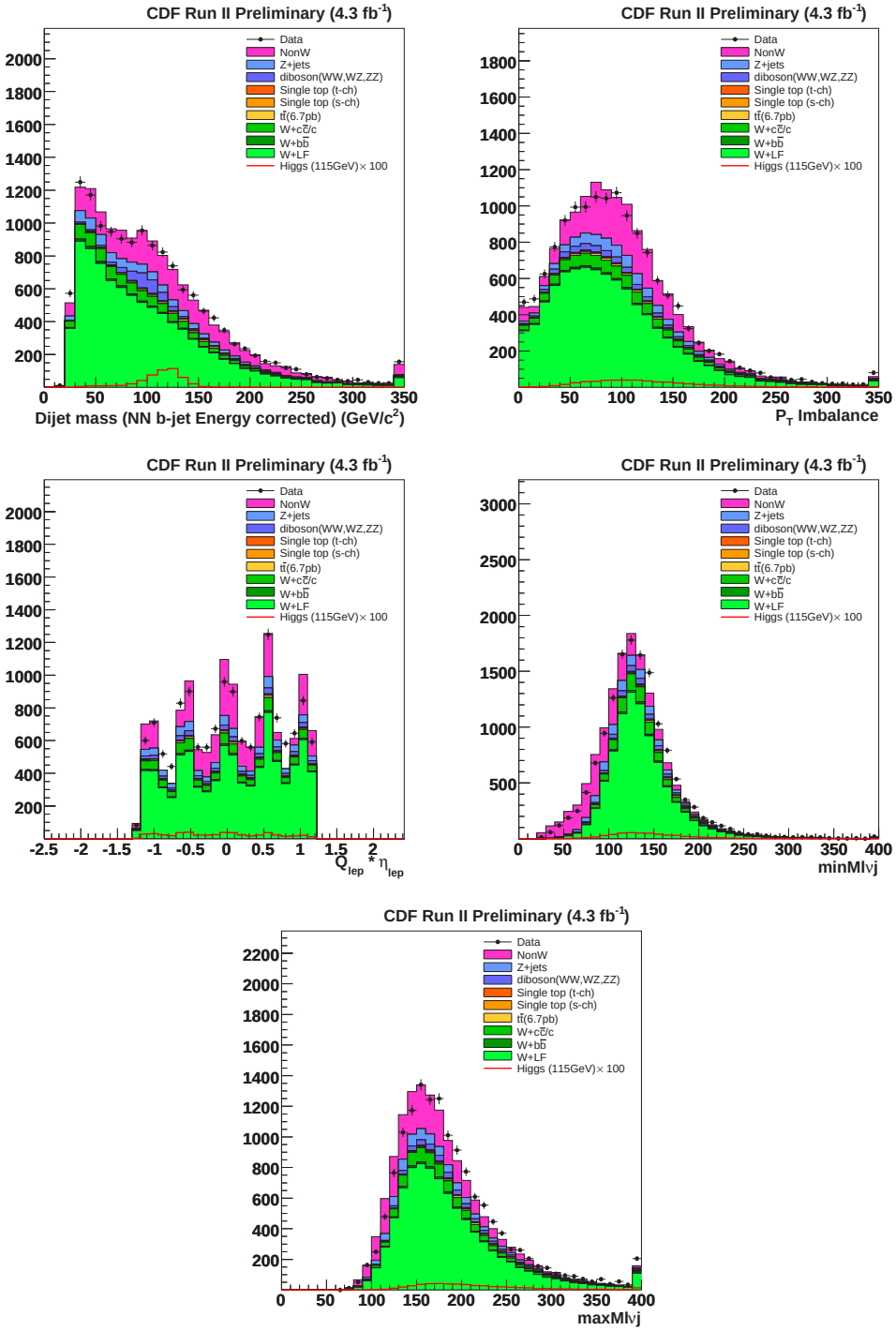

Figure 6.14: Isolated track pretag BNN inputs kinematics (1)

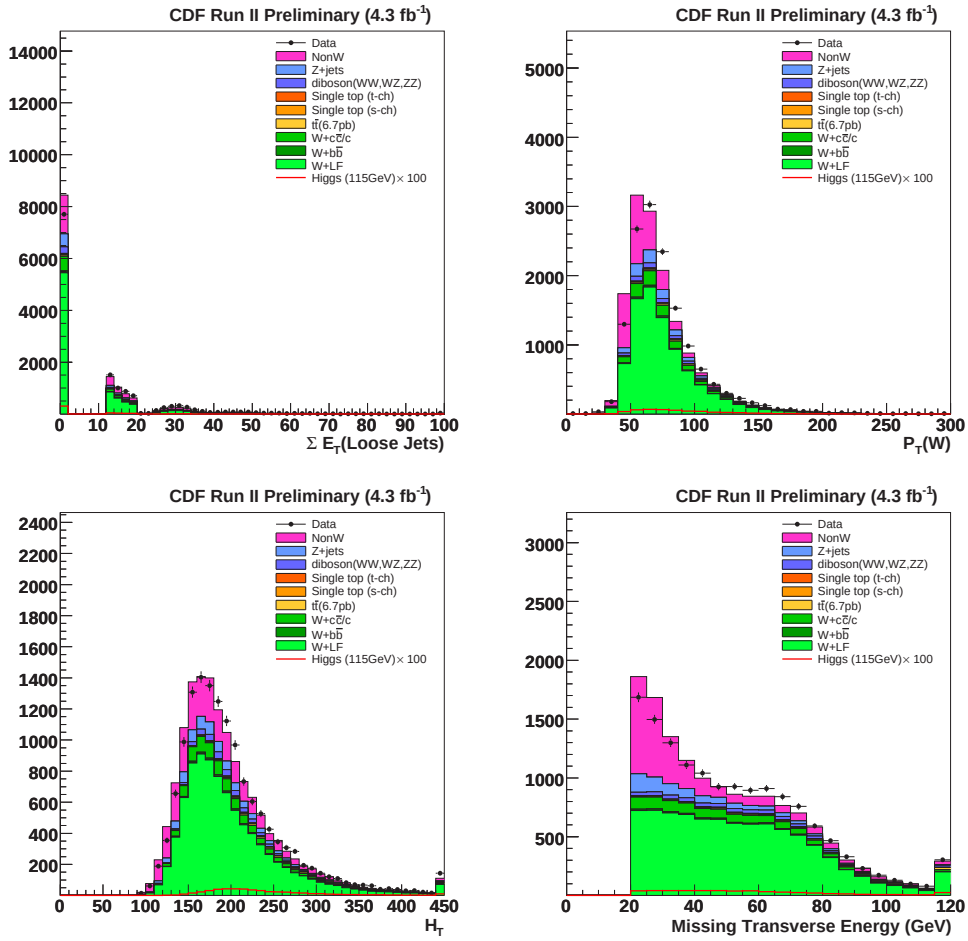

Figure 6.15: Isolated track pretag BNN inputs kinematics (2)

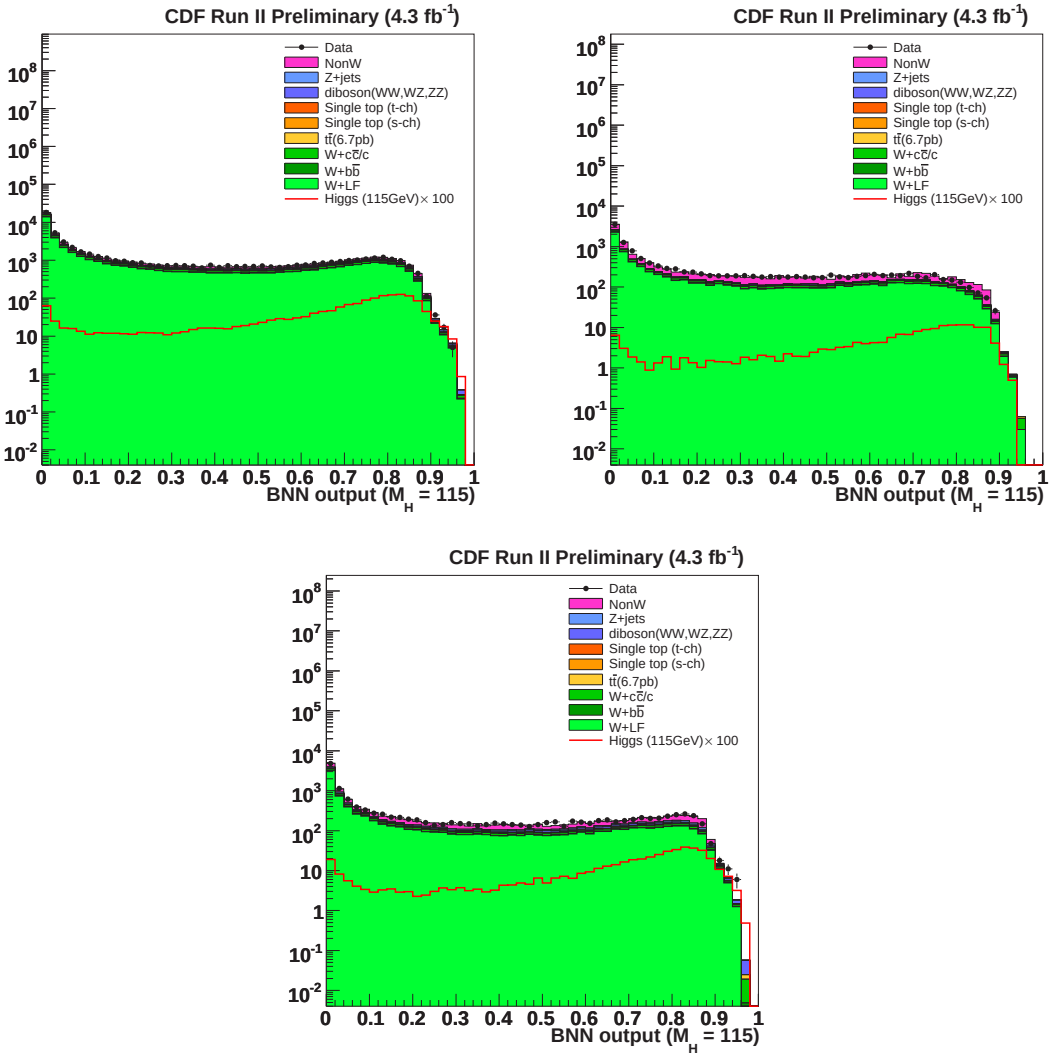

Figure 6.16: Pretag BNN outputs for the $m_H = 115\ \mathrm{GeV}/c^2$. From left to right and top to bottom, central lepton, plug electron, and isolated track category, respectively.

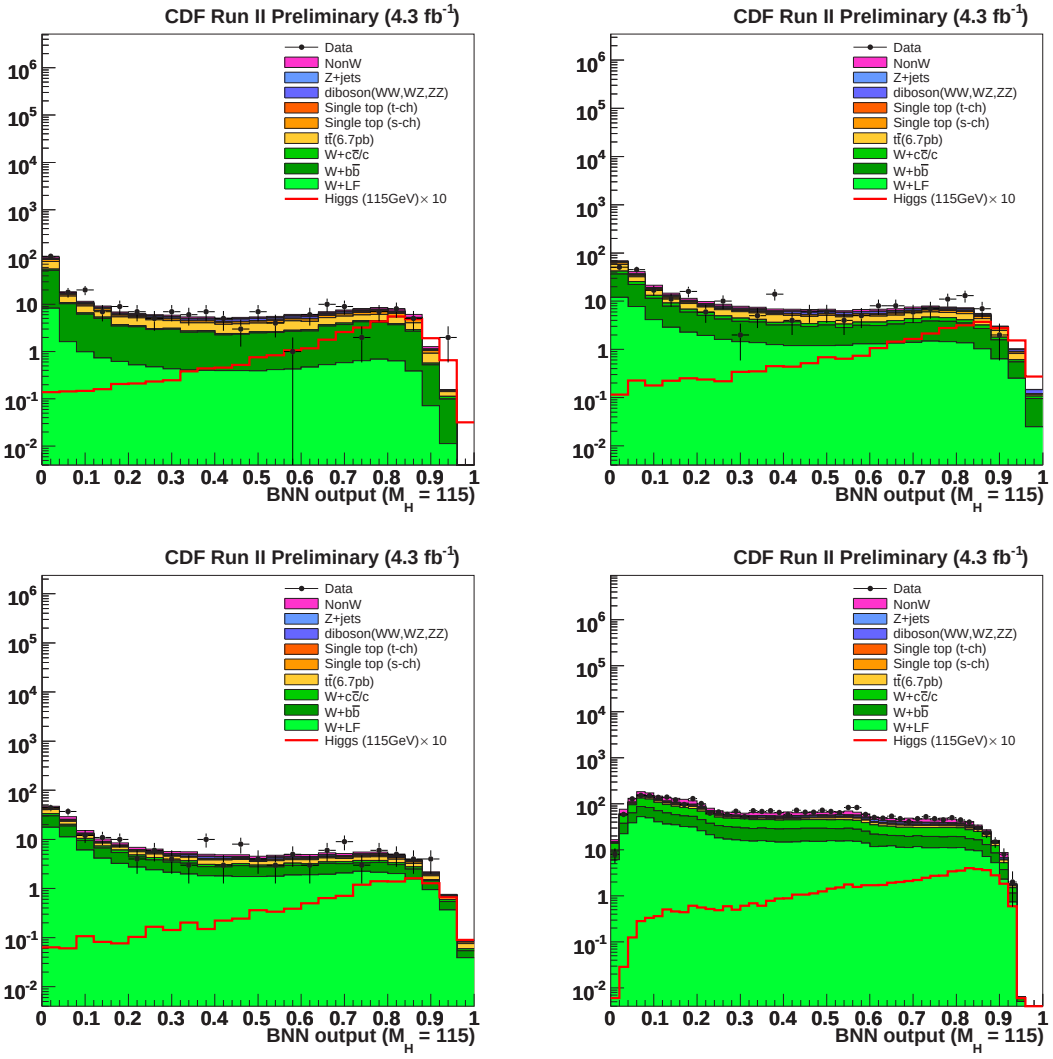

Figure 6.17: BNN outputs for the $m_H = 115\ \mathrm{GeV}/c^2$. From left to right and top to bottom, ST+ST, ST+JP, ST+NN and 1-ST b-tag category, respectively. All lepton types are combined.

Chapter 7

Signal Acceptance and Systematic Uncertainties

In this chapter, the number of expected Higgs events and systematic uncertainties on the signal acceptance are estimated.

7.1 Expected Higgs Signal

To calculate the expected number of signal events, $N_{WH\to l\nu b\bar{b}}$, the following equation is used:

$$N_{WH\to l\nu b\bar{b}} = \epsilon_{WH\to l\nu b\bar{b}} \cdot \mathcal{L} \cdot \sigma(p\bar{p} \to WH) \cdot \text{Br}(H \to b\bar{b}), \tag{7.1}$$

where $\epsilon_{WH\to l\nu b\bar{b}}$ is the detection efficiency for signal events, $\mathcal{L}$ is the integrated luminosity, $\sigma(p\bar{p} \to WH)$ is the WH production cross section in $p\bar{p}$ collisions and $\text{Br}(H \to b\bar{b})$ is the branching ratio for Higgs decaying to $b\bar{b}$. The detection efficiency for signal events is defined as:

$$\epsilon_{WH\to l\nu b\bar{b}} = \epsilon_{Z0} \cdot \epsilon_{\text{trig}} \cdot \epsilon_{\text{leptonid}} \cdot \epsilon^{\text{MC}}_{WH\to \ell\nu b\bar{b}} \cdot \left(\sum_{l=e,\mu,\tau} \text{Br}(W \to l\nu) \right), \tag{7.2}$$

where $\epsilon^{MC}_{WH\to l\nu b\bar{b}}$ is the fraction of signal events (with $|z_0| < 60$cm) which pass the kinematic and b-tagging requirements. We correct the number of tagged events in the MC by multiplying the b-tag scale factors. The quantity ϵ_{Z0} is the efficiency for the $|z_0| < 60$ cm cut. The trigger efficiency, ϵ_{trig}, is measured in the data. We apply a lepton reconstruction scale factor as to match the efficiency for the various types of lepton reconstruction to what is measured in $Z \to \ell^+\ell^-$ data. Finally, $\text{Br}(W \to l\nu)$ is the branching ratio for leptonic W decay.

Samples of PYTHIA $WH \to l\nu b\bar{b}$ MC with Higgs boson masses between 100 GeV/c^2 and 150 GeV/c^2 are generated with 5 GeV/c^2 step and used to estimate $\epsilon^{MC}_{WH\to l\nu b\bar{b}}$.

Table 7.1 shows the NNLO WH production cross section and the branching ratio of $H \to b\bar{b}$. The cross sections and the branching ratios in Table 7.1 are multiplied together with the integrated luminosity, 4.3 fb^{-1}, and the overall event detection efficiencies, which are the numbers of expected WH events as shown in Table 7.2.

m_H (GeV/c^2)	$\sigma(p\bar{p} \to W^{\pm}H)$ (pb)	Br($H \to b\bar{b}$)
100	0.298	0.812
105	0.253	0.796
110	0.216	0.770
115	0.186	0.732
120	0.160	0.679
125	0.138	0.610
130	0.119	0.527
135	0.104	0.436
140	0.090	0.344
145	0.079	0.256
150	0.069	0.176

Table 7.1: Theoretical cross section for WH production and Higgs boson branching ratio to $b\bar{b}$ for different masses.

Category	CEM	CMUP	CMX	PHX	IsoTrk (MET2J)	IsoTrk (MET45)
1-ST tag	2.68	1.39	0.69	0.53	0.95	0.38
ST+ST tag	1.25	0.66	0.33	0.26	0.60	0.11
ST+JP tag	1.07	0.56	0.26	0.20	0.43	0.11
ST+NN tag	0.48	0.26	0.12	0.10	0.21	0.05

Table 7.2: Expected number of WH events for $m_H = 115\ \mathrm{GeV}/c^2$, shown for each b-tag category and lepton type.

7.2 Systematic Uncertainties on Acceptance

In this section, we describe the systematic uncertainty estimation on the signal acceptance.

1. Lepton identification systematic uncertainties are evaluated by comparing the CDF data sample of Z events with the PYTHIA Z sample. These uncertainties are estimated for each lepton type.

2. Trigger systematic uncertainty is measured using a backup trigger, as described in Section 4.1. This uncertainty depends on the trigger type, but it has only a small contribution.

3. Initial and Final State Radiation (ISR and FSR) systematic uncertainties are estimated by changing the parameters related to ISR and FSR from their default values to half and double. Half of the difference between the two shifted samples is taken as the systematic uncertainty.

4. The parton distribution functions (PDFs) of the protons and antiprotons are not perfectly known. The MC samples used in this analysis are generated with CTEQ5L PDF [60, 61], which is calculated in a leading order (LO). The CTEQ PDF is parameterized with 20 eigenvectors. First, we re-weight the nominal MC samples using the 20 orthogonal PDF sets and calculate the 20 corresponding acceptance. The differences between the nominal and weighted acceptance is added in a quadrature and taken as the uncertainty. Secondly, we compare the difference on acceptance using two different PDFs, CTEQ5L and MRST72 [62], and take the absolute difference as the uncertainty. Thirdly, we also compare PDFs with different values of the strong coupling constant, corresponding to different QCD energy scales: MRST72 ($\Lambda_{QCD} = 228$ MeV) and MRST75 ($\Lambda_{QCD} = 300$ MeV), and take the absolute difference on acceptance as the uncertainty. Finally, we take the larger of the first uncertainty or the uncertainty of second and third added in a quadrature as the systematic uncertainty.

5. To obtain the systematic uncertainty coming from the jet energy scale, we use the WH MC sample for a Higgs mass of 120 GeV/c^2. The jet energies in the WH MC samples are shifted by $\pm 1\sigma$, and then we calculate the acceptance and take the deviation of this acceptance from the nominal acceptance as the systematic uncertainty.

6. The uncertainty for the b-tagging scale factor is discussed in Section 3.2.4.

7. The luminosity measurement uncertainty is also taken account. This contributes an overall 6% of rate uncertainty.

Total systematic uncertainties are listed in Table 7.3, 7.4 and 7.5 for each lepton category.

b-tagging category	Lepton ID	Trigger	ISR/FSR/PDF	JES	b-tagging	Total
1-ST	2%	$< 1\%$	3.0%	2.3%	4.3%	6.1%
ST+ST	2%	$< 1\%$	4.9%	2.0%	8.6%	10.3%
ST+JP	2%	$< 1\%$	4.9%	2.8%	8.1%	10.1%
ST+NN	2%	$< 1\%$	7.7%	2.2%	13.6%	15.9%

Table 7.3: Systematic uncertainties on the acceptance for central leptons.

b-tagging category	Lepton ID	Trigger	ISR/FSR/PDF	JES	b-tagging	Total
1-ST	2%	$< 1\%$	5.7%	2.9%	4.3%	8.0%
ST+ST	2%	$< 1\%$	7.7%	2.4%	8.6%	12.0%
ST+JP	2%	$< 1\%$	4.5%	3.9%	8.1%	10.3%
ST+NN	2%	$< 1\%$	12.9%	6.7%	13.6%	20.0%

Table 7.4: Systematic uncertainties on the acceptance for plug electrons.

b-tagging category	IsoTrk Reco	Trigger	ISR/FSR/PDF	JES	b-tagging	Total
1-ST	8.85%	2%	8.4%	4.7%	4.3%	13.9%
ST+ST	8.85%	2%	7.1%	1.7%	8.6%	14.5%
ST+JP	8.85%	2%	6.4%	2.4%	8.1%	14.0%
ST+NN	8.85%	2%	19.5%	1.9%	13.6%	25.5%

Table 7.5: Systematic uncertainties on the acceptance for isolated tracks.

Chapter 8

Results and Discussions

8.1 Limits on Higgs Production Cross Section

Since there is no significant excess of events in the data comparing the background expectation and the BNN output distributions, we fit the BNN output distribution and extract 95% C.L. upper limits for the four b-tag categories (1-ST, ST+ST, ST+JP and ST+NN) in each of the three lepton categories (central leptons, plug electrons, and isolated tracks) using pseudo-experiments based on the background expectation distribution.

We set an upper limit on the production cross section times branching ratio of $p\bar{p} \rightarrow WH$ as a function of m_H by using the number of events in the W + 2 jets sample. Since there are no peaks observed in the BNN output distribution, we assume that the W + 2 jets and BNN output distributions in the data consist of mistags, W + heavy flavors ($W + b\bar{b}$, $W + c\bar{c}$, $W + c$), dibosons (WW, WZ, ZZ), Z+jets, and top productions ($t\bar{t}$ and single top). A 1-dimensional binned maximum likelihood technique is used to obtain the limit on the cross section of signal process. The expected number of events (μ_i) in each mass bin is

$$\mu_i = \sum_{k=1}^{\text{Bkg}} f_i^k \cdot N^k + f_i^{WH \rightarrow l\nu b\bar{b}} \cdot (\varepsilon \cdot \mathcal{L} \cdot \sigma_{WH \rightarrow l\nu b\bar{b}}),$$

where k corresponds to background index for mistags, W + heavy flavors, dibosons, Z+jets, and top productions. f_i^k and $f_i^{WH \rightarrow l\nu b\bar{b}}$ are the expected fractions of events for the background and the signal in a given mass bin, predicted by MC. N^k, ε, $\mathcal{L}$ and $\sigma_{WH \rightarrow l\nu b\bar{b}}$ are the expected number of background events, the detection efficiency, the luminosity, and the unknown $WH \rightarrow l\nu b\bar{b}$ cross section, respectively. In pseudo-experiments, we select background events independently according to Gaussian distributions with the estimated total uncertainty as the standard deviations. The corresponding likelihood is then

$$\begin{aligned} L(\sigma/\sigma_{\text{SM}}) &= \int \cdots \int \prod_{i \in \text{ bins}} \frac{\mu_i^{N_i} \cdot e^{-\mu_i}}{N_i!} \prod_{k=1}^{Bkg} G(N_k, \sigma_{N_k}) \\ &\times G(N_{WH}, \sigma_{N_{WH}}) dN_k dN_{WH}. \end{aligned} \tag{8.1}$$

We define the expected limit by taking the median value of the pseudo-experiments. The extracted limit using all lepton categories and b-tag categories is obtained by taking the product of the

m_H (GeV/c^2)	Observed Limit	Expected Limit
100	0.96 (3.98)	0.67 (2.78)
105	0.90 (4.47)	0.63 (3.12)
110	0.83 (5.01)	0.58 (3.48)
115	0.72 (5.26)	0.54 (3.98)
120	0.53 (4.88)	0.50 (4.62)
125	0.59 (7.01)	0.50 (5.99)
130	0.47 (7.53)	0.46 (7.36)
135	0.54 (11.8)	0.45 (10.1)
140	0.49 (15.7)	0.44 (14.1)
145	0.51 (25.0)	0.44 (21.8)
150	0.46 (37.6)	0.41 (33.7)

Table 8.1: Expected and observed upper limits $\sigma(p\bar{p} \rightarrow WH) \times BR(H \rightarrow b\bar{b})$ [pb] as a function of Higgs mass for the combined search of central lepton, plug electron and isolated track events, including all b-tag categories. The values in parenthesis are the upper limits normalized to the SM expectation.

likelihoods for all b-tagging and lepton categories:

$$L(\sigma/\sigma_{\text{SM}}) = \prod_{i \in \text{ leptons}} L(\sigma/\sigma_{\text{SM}}|\text{ST+ST})_i \times L(\sigma/\sigma_{\text{SM}}|\text{ST+JP})_i \times L(\sigma/\sigma_{\text{SM}}|\text{ST+NN})_i \times L(\sigma/\sigma_{\text{SM}}|1-\text{ST})_i \quad (8.2)$$

where i corresponds to the lepton category of central leptons, plug electrons, or isolated tracks.

Table 8.1 details the expected and observed limits at the assumed Higgs mass points. Figure 8.1 shows the observed limits and the expected limits with 1σ and 2σ pseudo-experiment bands.

This $WH \rightarrow \ell\nu b\bar{b}$ analysis represents a substantial improvement in sensitivity over the prior analysis using a neural network [12][†]. The increase in sensitivity is 26% at m_H = 115 GeV/c^2, including an increase in integrated luminosity. New analysis techniques alone provide 15% of increased sensitivity.

[†]The previous analysis combines two $WH \rightarrow \ell\nu b\bar{b}$ analyses: a neural network analysis and a matrix element analysis. The comparison described here is the sensitivity improvement compared to the former neural network analysis.

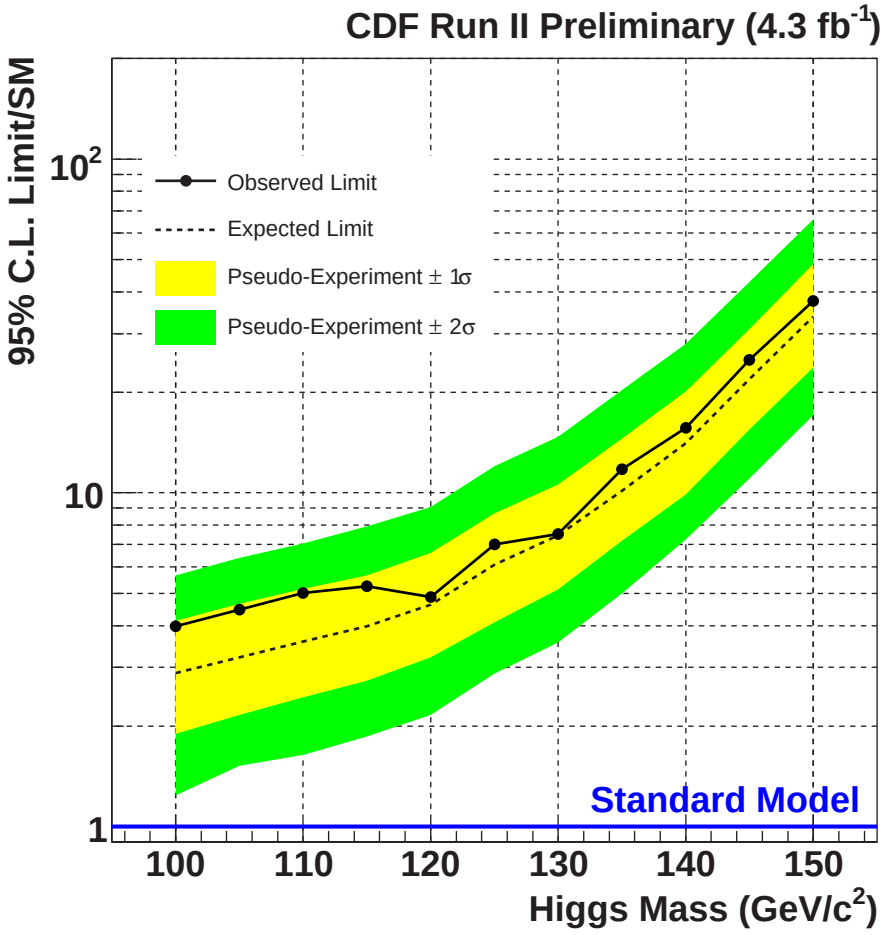

Figure 8.1: Expected and observed limits for a search combing all lepton and b-tag categories.

8.2 Combined Upper Limit on Higgs Boson Production Cross Section

8.2.1 Combined Upper Limit on Higgs Boson Production Cross Section at CDF

In this section, we describe the combined limit on Standard Model Higgs boson production at CDF [63].

This combination includes the results of the six main searches: the $WH \rightarrow \ell\nu b\bar{b}$ channel with 4.3 fb^{-1} of data, the $WH + ZH \rightarrow \not\!\!E_T + b\bar{b}$ channel with 3.6 fb^{-1} of data, the $ZH \rightarrow \ell^+\ell^- b\bar{b}$ channel with 4.1 fb^{-1} of data, the $H \rightarrow \tau^+\tau^-$ channel with 2.0 fb^{-1} of data, the $H \rightarrow W^+W^- \rightarrow \ell^+\nu\ell'^-\bar{\nu}$ channel with 4.8 fb^{-1} of data, and $WH + ZH \rightarrow jjb\bar{b}$ channel with 2.0 fb^{-1} of data. The combined observed and expected limits at CDF are shown in Figure 8.2 together with the individual analysis contributions. We obtain the observed (expected) values of 3.12 (2.38) at $m_H = 115\ \mathrm{GeV}/c^2$, and 1.18 (1.19) at $m_H = 165\ \mathrm{GeV}/c^2$.

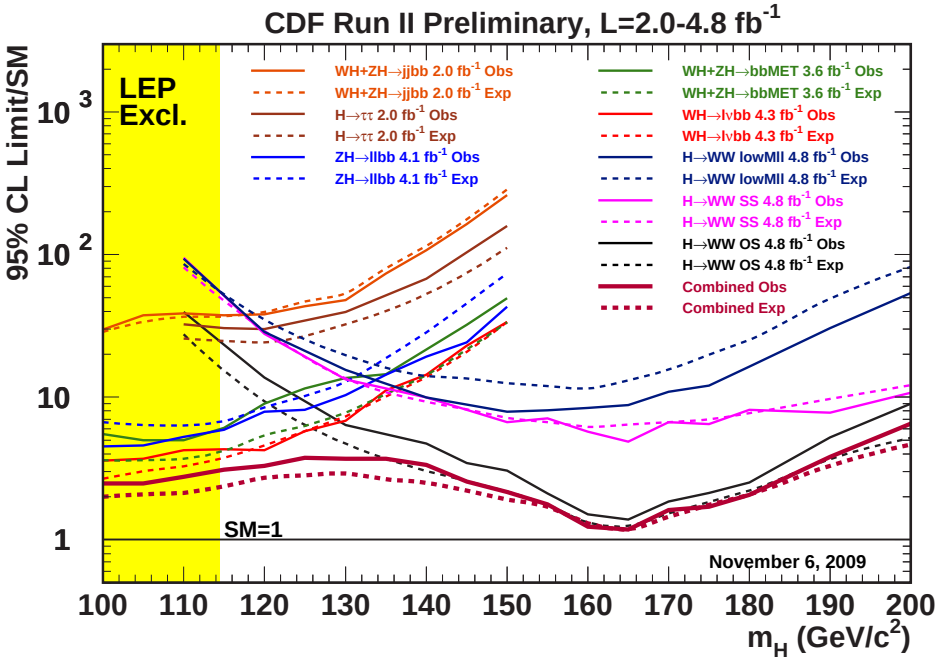

Figure 8.2: The combined upper limit at CDF as a function of the Higgs boson mass between 100 and 200 GeV/c^2. Solid lines are the observed upper limits for each channel and combined result (dark red). Dashed lines are the median expected upper limits for each channel and the combined result (dark red).

8.2.2 Combined Upper Limit on Higgs Boson Production Cross Section at Tevatron

Both the CDF and D0 experiments have performed new combinations of multiple direct searches for the Standard Model Higgs boson [64]. The corresponding integrated luminosity of data at CDF is ranging from 2.0 to 4.8 fb^{-1}, and at D0 is ranging from 2.1 to 5.4 fb^{-1}. The Higgs boson decay mode studied are $H \to b\bar{b}$, $H \to W^+W^-$, $H \to \tau^+\tau^-$, and $H \to \gamma\gamma$.

The ratio of the 95% C.L. expected and observed limits to the Standard Model cross section are shown in Figure 8.3 for the combined CDF and D0 analyses. We obtain the observed (expected) values of 2.7 (1.8) at $m_H = 115$ GeV/c^2, and 0.9 (0.9) at $m_H = 165$ GeV/c^2. The mass range expected to be excluded is $159 < m_H < 168$ GeV/c^2, while the obtained excluded region is $163 < m_H < 166$ GeV/c^2.

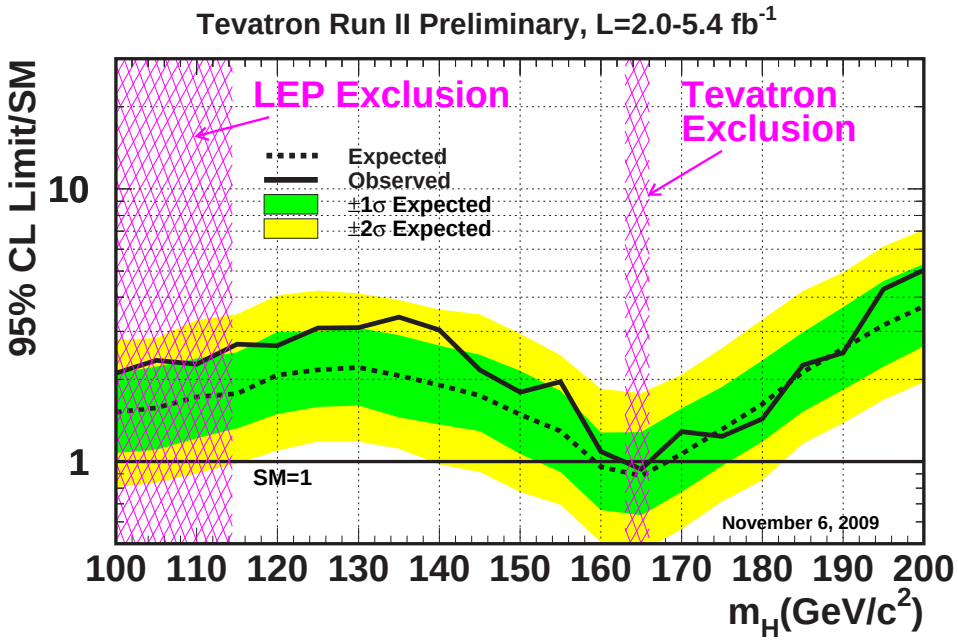

Figure 8.3: The upper limits as a function of the Higgs boson mass between 100 and 200 GeV/c^2 combined for the CDF and D0 analyses. The bands indicate the 68% and 95% probability regions where the limits can fluctuate, in the absence of signal. The limits displayed in this figure are obtained with the Bayesian calculation.

8.3 Outlook for the Higgs Boson Searches

As data are accumulated, the sensitivity of the searches is expected to increase. A simple extrapolation of the sensitivity is to scale the median expected limit with $1/\sqrt{\int \mathcal{L}dt}$. The comparison of the achieved expected limits and the extrapolations for CDF analyses is shown in Figure 8.4 for

$m_H = 115\ \mathrm{GeV}/c^2$ and $m_H = 160\ \mathrm{GeV}/c^2$. In this figure, the expected limits are divided by $\sqrt{2}$, which assumes the effects of combining with D0 analyses.

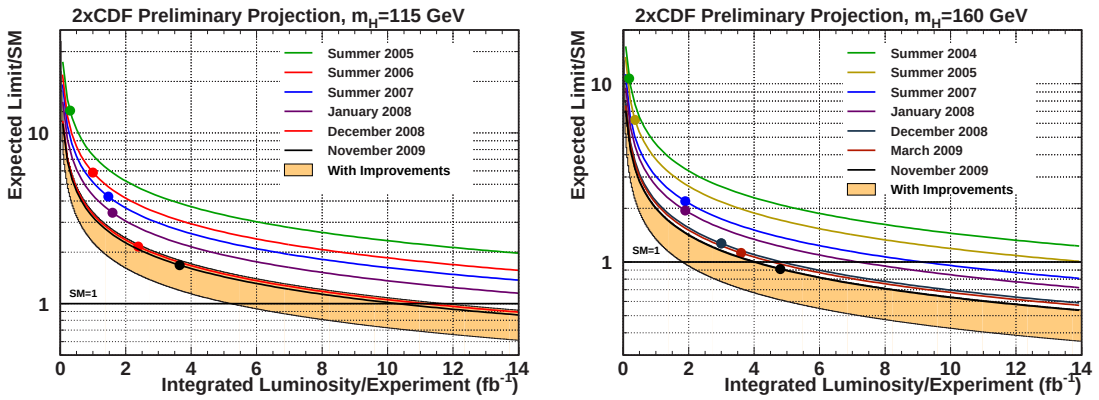

Figure 8.4: Projected median expected upper limits on the SM Higgs boson cross section, scaling the CDF performance to twice the luminosity. The solid lines are $1/\sqrt{\int \mathcal{L}dt}$ projections, as functions of integrated luminosity. The top of the orange band corresponds to the Summer 2007 performance expected limit divided by 1.5, and the bottom of the orange band corresponds to the Summer 2007 performance expected limit divided by 2.25. Left plot is shown for $m_H = 115\ \mathrm{GeV}/c^2$ and right plot is shown for $m_H = 160\ \mathrm{GeV}/c^2$.

The sensitivity of our combined search is sufficient to exclude the Higgs boson in the high mass region and is expected to grow substantially with additional luminosity already recorded by the CDF and D0 experiments. Since Tevatron plans to run through 2010, we will be able to analyze > 8.0 fb^{-1} of data near future. With additional improvements on the analyses, it is also possible to reach the Standard Model sensitivity even in the low mass region.

Chapter 9

Conclusions

We have performed a search for the Standard Model Higgs boson in the $WH \rightarrow \ell\nu b\bar{b}$ channel in 1.96 TeV proton-antiproton collisions at CDF. The search sensitivity is improved significantly with respect to previous searches, by about 15% more than the expectation from simple luminosity scaling. The main improvements are due to a sophisticated b-tag technique, a multivariate neural network technique to further separate the signal from the background, an improvement of di-jet mass resolution with a neural network b-jet energy correction, and increasing the acceptance for signal events by employing the MET45 trigger. These improvements, along with a dataset of 4.3 fb^{-1}, allow us to set a 95% C.L. upper limit on the production cross section times branching fraction that ranges 3.98 to 37.6 times the Standard Model expectation for Higgs boson masses spanning from 100 to 150 GeV/c^2. The resulting observed (expected) 95% C.L. upper limit for a Higgs mass of 115 GeV is:

$$\sigma(p\bar{p} \rightarrow W^{\pm}H) \times BR(H \rightarrow b\bar{b})|_{m_H=115} < 5.26\,(3.98) \times \mathrm{SM}$$

In addition to the $WH \rightarrow \ell\nu b\bar{b}$ channel, other search channels are combined to further improve the discovery sensitivity of the Standard Model Higgs boson. Another experiment at the Tevatron, the D0 experiment, also performed the Higgs boson searches using various channels. By combining the results from the two experiments, we set the latest upper limit on Standard Model Higgs Boson production cross section at Tevatron. The 95% C.L. on Higgs boson production cross section is 2.7 (0.9) times the Standard Model cross section for a Higgs boson mass of $m_H = 115$ (165) GeV/c^2. As a result, the 95% C.L. excluded region of the Standard Model Higgs boson mass is:

$$163 < m_H < 166\ \mathrm{GeV}/c^2$$

In the next couple of years, the Tevatron will continue running and deliver approximately twice data used in this analysis. The improvement of analyses has been done with continuous effort. It would be possible to reach the sensitivity that the Standard Model Higgs boson could be discovered, not only in the high mass region around $m_H = 160\ \mathrm{GeV}/c^2$ but also in the low mass region $m_H = 115\ \mathrm{GeV}/c^2$.

Appendix A

Search for Technicolor Particles

We present a search for the technicolor particles ρ_T and π_T in the process $p\bar{p} \to \rho_T \to W\pi_T$ at a center of mass energy of $\sqrt{s} = 1.96\,\mathrm{TeV}$ [65], in the context of the technicolor straw man (TCSM) model [66]. The search uses a data sample corresponding to approximately $1.9\,\mathrm{fb}^{-1}$ of integrated luminosity accumulated by the CDF II detector at the Fermilab Tevatron. The event signature we consider is $W \to \ell\nu$ and $\pi_T \to b\bar{b}, b\bar{c}$ or $b\bar{u}$ depending on the π_T charge. Figure A.1 shows the Feynman diagram of the technicolor signal.

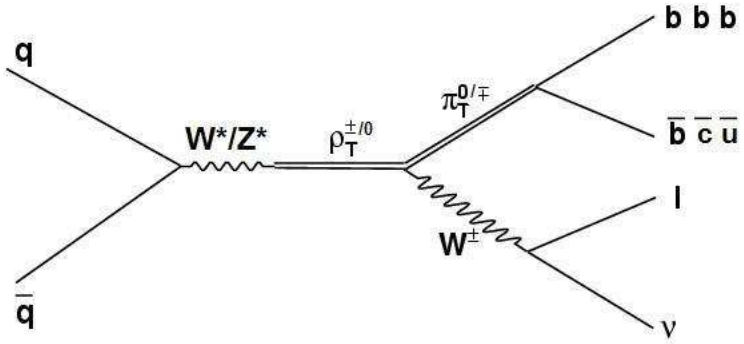

Figure A.1: Feynman diagram of the $p\bar{p} \to \rho_T \to W\pi_T$ channel.

The mechanism of electroweak symmetry breaking in nature is still unknown. The standard model (SM) assumes the Higgs mechanism [8, 9] but provides no explanation as to why there should be a fundamental scalar Higgs field with a non-zero vacuum expectation value. An alternative approach is to seek a dynamical mechanism for the symmetry breaking. The scenario known as technicolor [67–69] proposes a new strong interaction, modeled on QCD, which spontaneously breaks electroweak symmetry in an analogous way to the breaking of chiral symmetry in QCD. The strong technicolor interaction between the new technifermions results in a vacuum technifermion condensate which can break electroweak symmetry and hence give mass to the $W^{\pm}$ and Z gauge bosons. As in QCD, the technicolor interaction should give rise to technipions (π_T) and other technimesons. Like the SM Higgs, the technipion coupling to fermions is proportional to mass, and hence the technipion predominantly decays to $b\bar{b}$, $b\bar{c}$, or $b\bar{u}$, depending on its charge. The resulting final state is identified by selecting events with exactly one high-p_T electron or muon candidate, large missing transverse energy, and two jets, at least one of which is identified as containing a b-quark (b-tagged).

Previous searches by the CDF and D0 experiments [70, 71] were limited not only by smaller data samples, but also by contamination from jets associated with charm or light-flavor quarks which can be falsely tagged as b-jets. To improve the purity of the selected event sample, the search described in this Letter employs the same b-tagging strategies that are used in the SM Higgs search in the W + 2 jets channel [72]. Previous searches for technicolor particles at LEP were able to exclude ρ_T production at 95% confidence level for $90 < m_{\rho_T} < 206.7\,\mathrm{GeV}/c^2$, independently of the assumed π_T mass and other model parameters [73].

Events are required to have exactly one electron or muon candidate, large missing transverse energy ($\not\!\!E_T > 20\,\mathrm{GeV}$), and two jets. The electron or muon must be within the central part of the detector, in the pseudorapidity regions $|\eta| < 1.1$ or $|\eta| < 1.0$, respectively, and must have $E_T > 20\,\mathrm{GeV}$ or $p_T > 20\,\mathrm{GeV}$. Because the lepton from a leptonic W decay is well isolated from the rest of the event, the cone of $\Delta R = 0.4$ surrounding the lepton is required to contain less than 10% of the lepton transverse energy. It must also be no more than 5 cm in z away from the primary event vertex, which is defined by fitting a subset of charged particle tracks in the event to a single vertex. To reduce the background from Z boson decays, we reject not only events with multiple high-p_T leptons, but also events in which the lepton and another high-p_T track of opposite sign form an invariant mass between $76 < M_{ll} < 106\,\mathrm{GeV}/c^2$. Jets used in the analysis must fall within the acceptance of the silicon detector ($|\eta| < 2.0$) for reliable b-tagging, and they must have transverse energy greater than $20\,\mathrm{GeV}$.

The primary background to this technicolor search is SM W + 2 jets production. However this process is dominated by light-flavor jets, while the technipion decay process should contain at least one b quark. Identifying these b-quark jets therefore helps to significantly suppress the background. We use two b-tagging algorithms: SECVTX and JETPROB. To further improve the purity of the SECVTX sample, a neural network (NN) filter has been trained to reject tagged jets originating from charm or light-quarks [74,75][†]. The selection cuts on the NN output are chosen to give 90% efficiency for true b-jets identified with SECVTX while rejecting $65 \pm 5\%$ for light-flavor jets and $50 \pm 5\%$ for charm jets, as measured using simulated events and verified with multi-jet data. The search sensitivity is maximized by using three exclusive b-tagged event categories. The first category (ST+ST) contains events with two SECVTX b-tagged jets. The second category (ST+JP) consists of events where only one of the jets is b-tagged by SECVTX and the second jet is only b-tagged by JETPROB. The third category (ST+NNtag) is for events which do not belong to the first two categories but contain exactly one SECVTX b-tagged jet that also passes the NN filter. Because events with charm and light-flavor jets are unlikely to be double-tagged, the extra NN filter is not applied to double-tagged events.

The selected event sample includes contributions from other standard model processes. The largest backgrounds are due to W + jets production, $t\bar{t}$ production, and non-W multi-jet production, with small contributions from single top, diboson (WW, WZ, ZZ), and $Z \to \tau\tau$ production. These backgrounds are estimated using the same methods as the standard model Higgs boson search analysis in the W + 2 jets channel [74, 75]. A summary of the estimated backgrounds to the W + 2 jets final state that are described below is shown in Table A.1, along with the number of observed events in data and the expected technicolor signal events with $m_{\rho_T} = 200\,\mathrm{GeV}/c^2$ and $m_{\pi_T} = 115\,\mathrm{GeV}/c^2$.

The W + jets contribution includes jets from b and c quarks, and light-flavor jets mistagged by the b-tagging algorithm. The effect of true W + heavy-flavor production is estimated from a combination of data and simulation. We use the ALPGEN Monte Carlo program [57] to calculate the rate of $Wb\bar{b}$, $Wc\bar{c}$, and Wc production relative to inclusive W + jets production. This relative

[†]The NN filter introduced here is not same one introduced in Section 3.2.4

rate is then applied to the observed W + jets sample, after non-W and $t\bar{t}$ contributions have been subtracted. Finally, we apply b-tagging efficiencies and the NN filter rate calculated using the ALPGEN event samples.

Contributions from events with falsely tagged light-flavor jets (mistags) are estimated by measuring a mistag rate in inclusive jet data. The mistag rate is further modified by the NN filter efficiency. The resulting overall mistag rate is applied to the observed W + jets sample to yield the number of mistagged events expected in the sample.

Events from $t\bar{t}$ production followed by leptonic W decay typically have two b jets from top decay, significant missing transverse energy, and one high-p_T lepton with additional jets if one of the W bosons from the top quarks decay hadronically. The $t\bar{t}$ contribution to the $\ell\nu b\bar{b}$ final state is estimated using simulated PYTHIA events [55]. It is normalized to the next-to-leading-order (NLO) cross section $\sigma_{t\bar{t}} = 6.7^{+0.7}_{-0.9}$ pb calculated for $m_t = 175\,\mathrm{GeV/c^2}$ [76]. The small contribution from production of single top quarks is estimated using MADEVENT [56] and PYTHIA normalized to the NLO cross section [77].

The signature of W decay can also be mimicked by non-W multi-jet events which may contain a high-p_T reconstructed lepton and missing transverse energy. These can arise from semi-leptonic heavy-flavor decay or from hadrons misidentified as leptons. The reconstructed leptons from such events are rarely isolated from other energetic particles, as required by our event selection, and seldom yield large missing transverse energy. We therefore calculate the number of non-W events in our selected sample by extrapolating from sideband regions (defined in the space of lepton energy isolation and missing transverse energy) into the signal region [45].

Small contributions from diboson backgrounds (WW, WZ, and ZZ) are estimated using the NLO theoretical cross section calculations [78] and $Z \to \tau\tau$ backgrounds are estimated using the CDF result [79], with acceptances calculated using fully simulated events from the PYTHIA Monte Carlo program.

The dominant systematic uncertainty in the W + heavy-flavor background is the correction factor for simulation derived from multi-jet data [45]. Different simulation inputs give different factors, and we find a 30% relative uncertainty on the background from heavy-flavor. The background from mistags has uncertainties on the rate correction due to particle interactions in detector material and on the NN rejection factor. Both are estimated to be 15% relative errors. Cross-checks of sideband data yield a 17% relative uncertainty on the non-W multi-jet estimate. The electroweak background estimates for diboson and single top are subject to uncertainties in the b-tagging efficiency and the cross section predictions.

The signal process in $\rho_T \to W\pi_T \to l\nu j_1 j_2$ is expected to show resonant peaks in both the di-jet and W + 2 jets mass spectra. We reconstruct the p_z of the neutrino by constraining the invariant mass of the lepton-neutrino pair to the W boson mass, which gives a two-fold ambiguity. We select the solution with the smaller $|p_z|$, since that is more probable given the production mechanism of this heavy state; if there is no real solution, we set the imaginary part of solution to zero. Figure A.2 shows the observed di-jet mass spectra in the double tagged (ST+ST and ST+JP) and one SECVTX with NN filter tagged 2 jets samples, along with the distributions expected from the background processes. Figure A.3 shows the Q-value distribution in each b-tagging category, the mass difference defined as $Q = m(\rho_T) - m(\pi_T) - m(W)$, which exploits the fact that the Q-value for the ρ_T decay is quite small and consequently the resolution of the mass difference is better than the mass of the ρ_T itself. The signal distributions from the charged and neutral technicolor particles with $m_{\rho_T} = 200\,\mathrm{GeV}/c^2$ and $m_{\pi_T} = 115\,\mathrm{GeV}/c^2$ are also shown for comparison. There is no significant excess observed in either the di-jet mass or Q-value distributions.

The acceptance for $\rho_T \to W\pi_T \to \ell\nu b\bar{b}, b\bar{c}, b\bar{u}$, including leptonic τ decays, is calculated from samples generated with the PYTHIA Monte Carlo program using ρ_T mass values between 180

Selection	ST+ST	ST+JP	ST+NNtag
$Wb\bar{b}$	37.9±16.9	31.2±14.0	215.6±92.3
$Wc\bar{c}$	2.9±1.2	7.9±3.4	167.0±62.1
Mistag	3.9±0.4	11.7±0.9	107.1±9.4
$t\bar{t}$	19.0±2.9	15.6±2.4	60.7±9.3
Single top	8.5±1.2	7.0±1.0	44.0±6.4
non-W	5.5±1.0	9.6±1.7	184.7±33.0
WW	0.17±0.02	0.9±0.1	15.4±1.9
WZ	2.41±0.26	1.8±0.2	7.6±0.8
ZZ	0.06±0.01	0.08±0.01	0.31±0.03
$Z \to \tau\tau$	0.25±0.04	1.3±0.2	7.3±1.1
Total Bkg.	80.6±18.8	87.0±18.0	809.6±159.4
m($\rho_T^{\pm}$,π_T^0)=(200,115) GeV/c^2	11.2±1.4	7.7±1.1	20.7 ± 1.7
m(ρ_T^0,$\pi_T^{\mp}$)=(200,115) GeV/c^2	1.5±0.3	2.8±0.6	23.0±2.0
Observed Events	83	90	805

Table A.1: Predicted sample composition and observed number of W + 2 jets in each b-tagging category, along with the expected signal events for a mass hypothesis of $m_{\rho_T} = 200\,\mathrm{GeV}/c^2$ and $m_{\pi_T} = 115\,\mathrm{GeV}/c^2$.

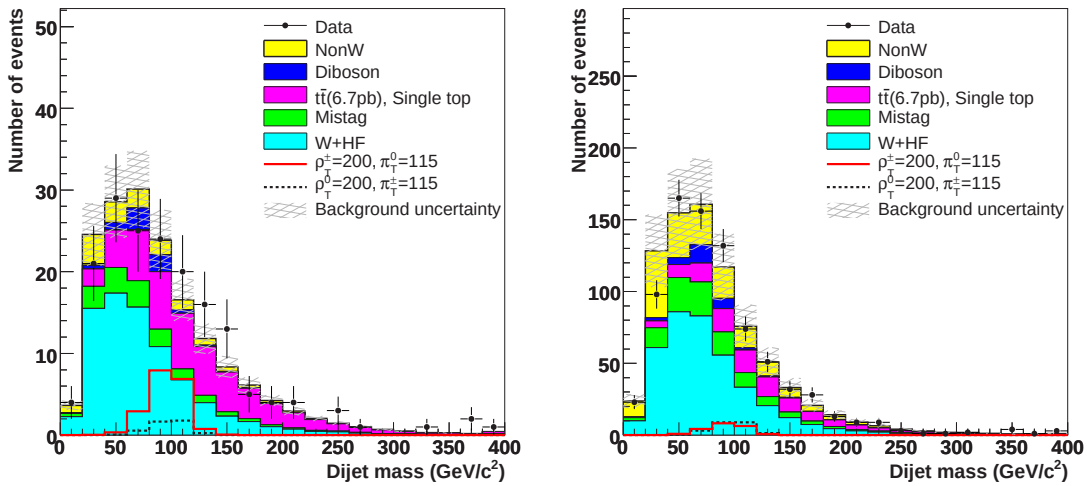

Figure A.2: Reconstructed di-jet mass distributions for W + 2 jets events. The left is for double tags (ST+ST and ST+JP) and the right is for single tag (ST+NNtag) events.

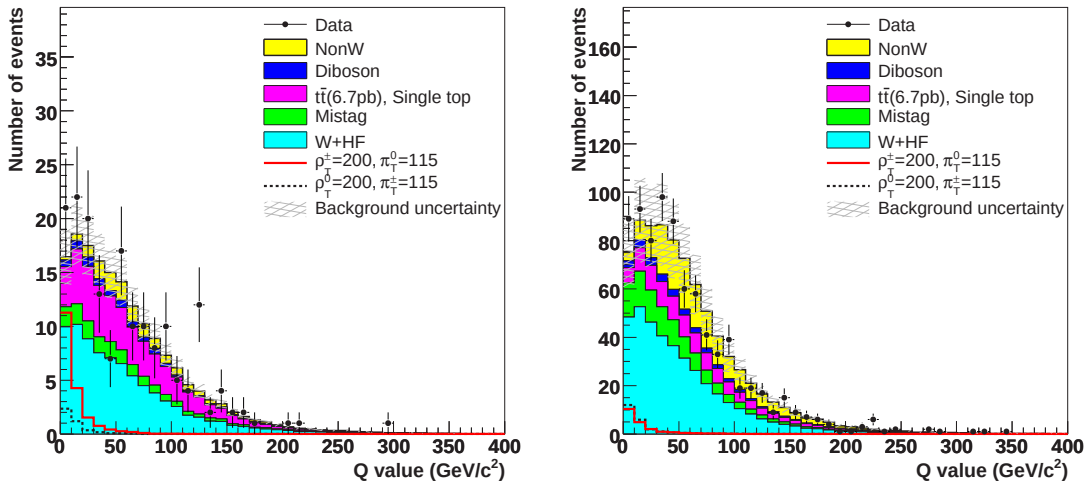

Figure A.3: Reconstructed Q-value distributions for W + 2 jets events, where $Q = m(\rho_T) - m(\pi_T) - m(W)$. The left is for double tags (ST+ST and ST+JP) and the right is for single tag (ST+NNtag) events.

and $250\,\mathrm{GeV}/c^2$ with a step of 10 GeV/c^2. We set the parameters in the TCSM as: $N_{TC} = 4$, $M_V = M_A = 200\,\mathrm{GeV}/c^2$, $Q_U = Q_D + 1$ and $\sin\chi = 1/3$, where N_{TC} is the number of technicolors, M_V is the vector technimeson decay parameter, M_A is the axial mass parameter for technivector decays to technipion, $Q_U(Q_D)$ is the charge of the up-type (down-type) technifermion, and $\sin\chi$ is the mixing angle between isotriplet technipion interaction and mass eigenstates. For this study, we consider the lightest technihadron masses in the $\rho_T - \pi_T$ mass plane $180 < m(\rho_T) < 250$ GeV/c^2 and $max(m(\rho_T)/2, m(W)) < m(\pi_T) < m(\rho_T) - m(W)$ where the decay $\rho_T \to W\pi_T$ dominates. The cut-off $m(\rho_T)$ at 250 GeV/c^2 is set by the search sensitivity.

The total acceptances for ST+ST, ST+JP and ST+NNtag events of $\pi_T^0 \to b\bar{b}$ ($\pi_T^\pm \to b\bar{c}, b\bar{u}$) are $0.40 \pm 0.05\%$ ($0.05 \pm 0.01\%$), $0.27 \pm 0.04\%$ ($0.10 \pm 0.02\%$), and $0.73 \pm 0.06\%$ ($0.81 \pm 0.07\%$), respectively, for $m_{\rho_T} = 200\,\mathrm{GeV}/c^2$ and $m_{\pi_T} = 115\,\mathrm{GeV}/c^2$. The dominant systematic uncertainty on the acceptance for the $\pi_T^0 \to b\bar{b}$ ($\pi_T^\pm \to b\bar{c}, b\bar{u}$) process originates from the uncertainty on the b-tagging efficiencies, which is a 8.4% (9.4%) relative error for ST+ST, a 9.2% (17.0%) relative error for ST+JP, and a 4.3% (4.3%) relative error for ST+NNtag. Additional sources of systematic error include the jet energy scale, the lepton identification efficiency, parton distribution functions, and the initial and final state radiation models [49]. The systematic uncertainties associated with the shape of di-jet invariant mass and Q-value are also studied by varying the jet energy scale and the initial and final state radiation, which are found to have a negligible impact on the final results.

Since there is no significant excess of events in the data compared to the predicted background, we set the 95% C.L. excluded region on technicolor production as a function of the technicolor particle mass. A 2-dimensional binned maximum-likelihood technique which assumes Poisson statistics is used on the 2-dimensional distribution of di-jet invariant mass vs Q-value by constraining the number of background events within the uncertainties. To calculate the 95% C.L. excluded region, we use neutral and charged π_T signals simultaneously. A Bayesian interval is constructed from the cumulative likelihood distributions and a prior probability density function

$m(\rho_T,\pi_T)$	Normalized Upper Limit		$m(\rho_T,\pi_T)$	Normalized Upper Limit	
GeV/c^2	Observed Limit	Expected Limit	GeV/c^2	Observed Limit	Expected Limit
(180,95)	0.30	$0.22^{+0.09}_{-0.11}$	(230,125)	0.60	$0.48^{+0.22}_{-0.18}$
(190,95)	0.27	$0.27^{+0.11}_{-0.13}$	(230,135)	0.72	$0.49^{+0.21}_{-0.19}$
(190,105)	0.44	$0.28^{+0.13}_{-0.13}$	(230,145)	1.61	$0.79^{+0.35}_{-0.29}$
(200,105)	0.37	$0.30^{+0.13}_{-0.13}$	(240,125)	0.71	$0.57^{+0.26}_{-0.20}$
(200,115)	0.59	$0.37^{+0.18}_{-0.14}$	(240,135)	0.65	$0.56^{+0.25}_{-0.21}$
(210,110)	0.36	$0.33^{+0.15}_{-0.15}$	(240,145)	0.86	$0.58^{+0.24}_{-0.24}$
(210,115)	0.42	$0.33^{+0.15}_{-0.13}$	(240,155)	1.94	$1.03^{+0.45}_{-0.37}$
(210,125)	0.88	$0.47^{+0.21}_{-0.17}$	(250,130)	0.75	$0.65^{+0.27}_{-0.25}$
(220,115)	0.59	$0.42^{+0.19}_{-0.17}$	(250,135)	0.76	$0.66^{+0.26}_{-0.26}$
(220,125)	0.52	$0.39^{+0.17}_{-0.15}$	(250,145)	0.69	$0.65^{+0.27}_{-0.25}$
(220,135)	1.22	$0.59^{+0.27}_{-0.23}$	(250,155)	1.02	$0.72^{+0.34}_{-0.26}$
(230,120)	0.67	$0.48^{+0.24}_{-0.18}$	(250,165)	2.01	$1.31^{+0.58}_{-0.44}$

Table A.2: Expected and observed upper limit on $\sigma(\rho_T \rightarrow \pi_T W^{\pm}) \times BR(\pi_T \rightarrow b\bar{q})/(\sigma_{\mathrm{theory}}(\rho_T \rightarrow \pi_T W^{\pm}) \times BR_{\mathrm{theory}}(\pi_T \rightarrow b\bar{q}))$ as a function of the $m(\rho_T)$ and $m(\pi_T)$ hypothesis.

uniform in the number of technicolor signal events. The 95% confidence level upper limit is defined to be the value s_{up} for which $\int_0^{s_{\mathrm{up}}} L(s)ds / \int_0^{\infty} L(s)ds = 0.95$. The number of signal events is then converted to a technicolor particle production cross section times branching fraction $\sigma(p\bar{p} \rightarrow W\pi_T^0(\pi_T^{\pm})) \cdot BR(\pi_T^0(\pi_T^{\pm}) \rightarrow b\bar{b}(b\bar{c}, b\bar{u}))$.

The expected limits determined from pseudo experiments and the observed limits relative to the theoretical production rate are listed in Table A.2. The expected and observed 95% confidence level excluded region in the ρ_T-π_T mass plane is shown in Fig. A.4. Almost the entire region we have looked at in this search is excluded at 95% confidence level, except the area near the $W\pi_T$ production threshold with $m(\rho_T) \geq 220\,\mathrm{GeV}/c^2$ and $m(\pi_T) \geq 125\,\mathrm{GeV}/c^2$.

In summary, we have performed a search for technicolor production $p\bar{p} \rightarrow \rho_T^{\pm/0} \rightarrow W^{\pm}\pi_T^{0/\mp} \rightarrow \ell\nu b\bar{b}$, $\ell\nu b\bar{c}$, or $\ell\nu b\bar{u}$ using $1.9\,\mathrm{fb}^{-1}$ of integrated luminosity accumulated by the CDF II detector. A large fraction of the region of $m(\rho_T) = 180$ - $250\,\mathrm{GeV}/c^2$ and $m(\pi_T) = 95$ - $145\,\mathrm{GeV}/c^2$ is excluded at 95% confidence level, based on the technicolor Straw Man model. This measurement excludes a much larger region than the previous Tevatron searches [70, 71].

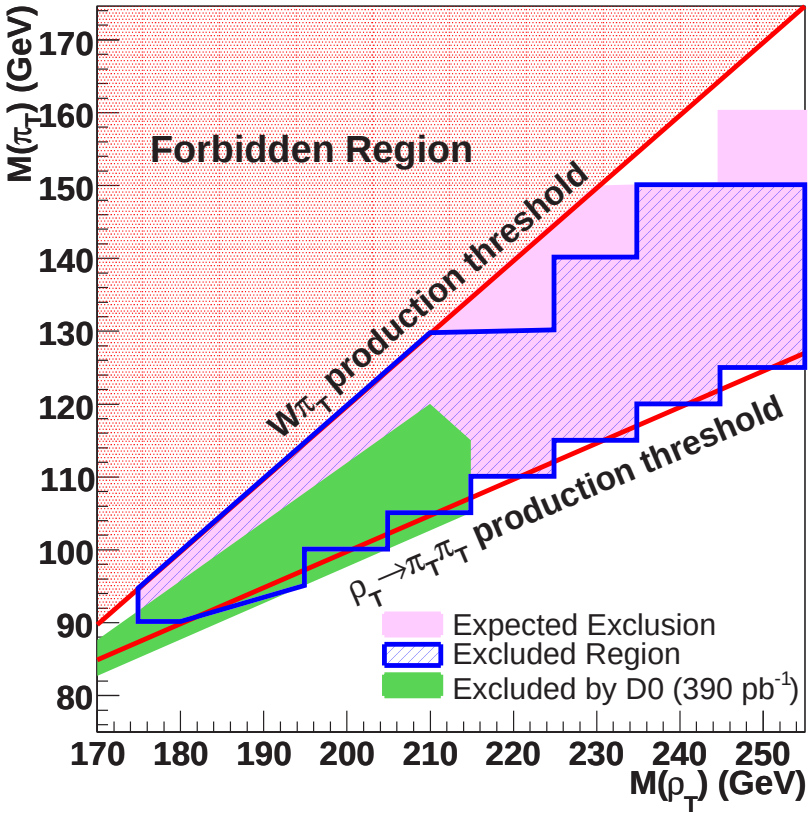

Figure A.4: 95% confidence level excluded region on technicolor particles production cross section times branching fraction as a function of $m(\rho_T)$ and $m(\pi_T)$ mass hypothesis. The expected excluded region from background-only pseudo-experiments are shown with the observed results from this analysis and D0 searches.

Appendix B

Background Modeling Validation

This chapter shows the validation plots between data and our background modeling. The kinematic distribution for basic observable variables has been thoroughly examined using the high statistic control region. Here, we use the pretag samples to examine the background modeling.

The kinematic variables examined are:

- 1st leading jet E_T, η, and ϕ
- 2nd leading jet E_T, η, and ϕ
- Lepton p_T, η, and ϕ
- Missing transverse energy ($\not\!\!E_T$) and ϕ
- Transverse mass of W boson
- $\Delta\phi$ and ΔR between leading two jets
- $\Delta\phi$ between $\vec{\not\!\!E}_T$ and lepton
- $\Delta\phi$ between lepton and 1st leading jet
- $\Delta\phi$ between lepton and 2nd leading jet
- Di-jet invariant mass before applying NN b-jet energy correction

The validation plots for the central lepton category are shown in Figure B.1–B.3. Figure B.4–B.6 are for the plug lepton category, and Figure B.7–B.9 are for the isolated track category.

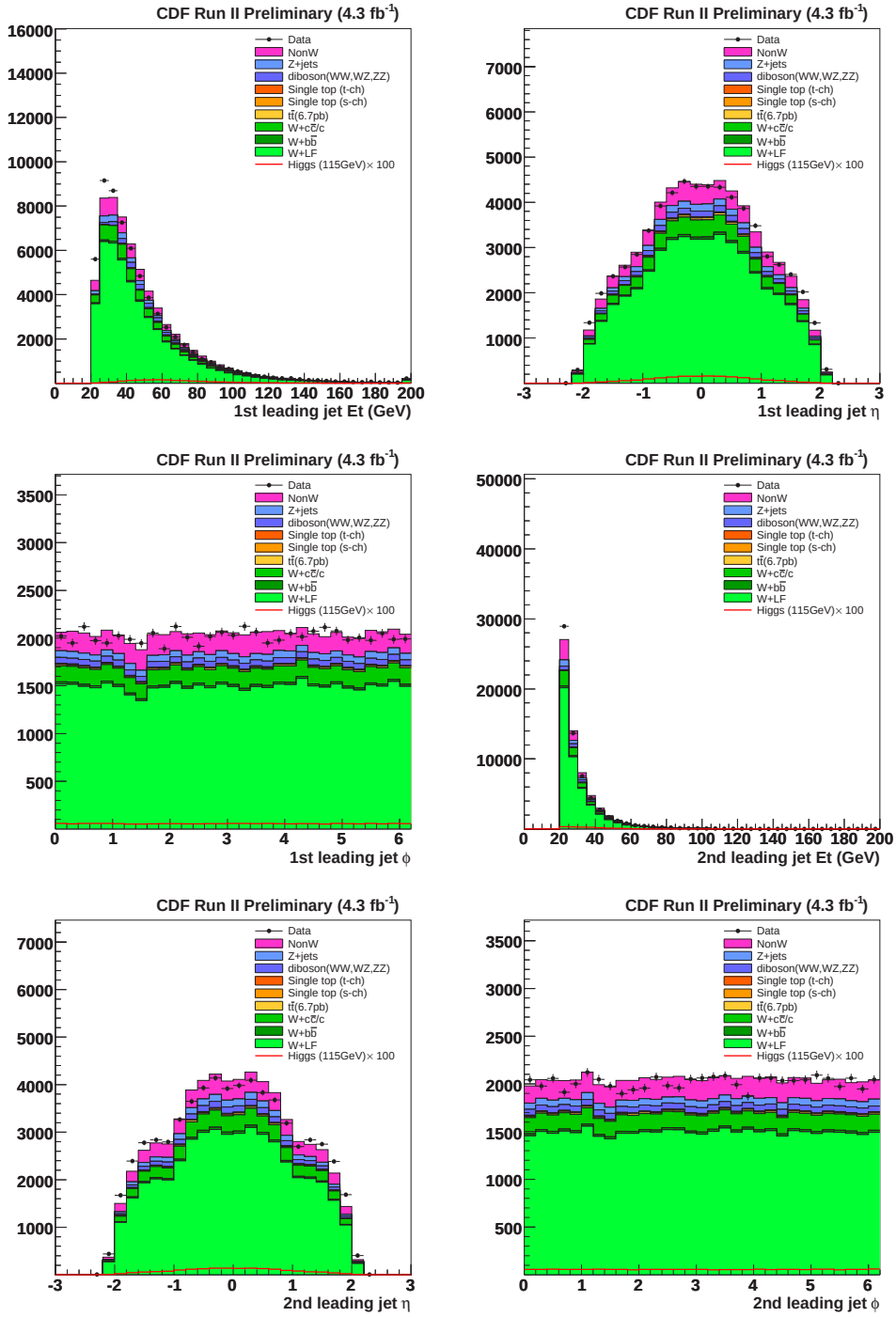

Figure B.1: Central lepton pretag basic kinematics (1)

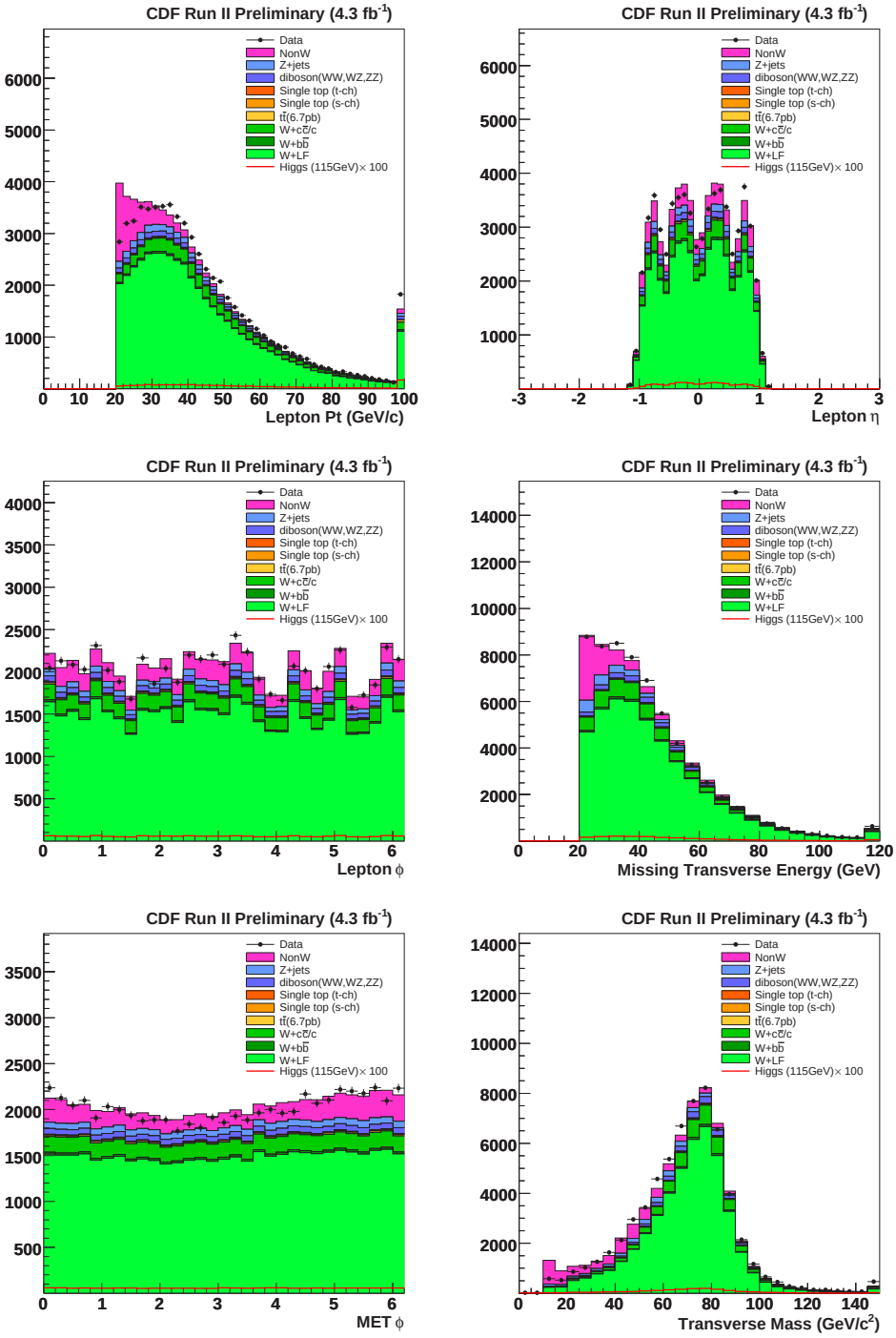

Figure B.2: Central lepton pretag basic kinematics (2)

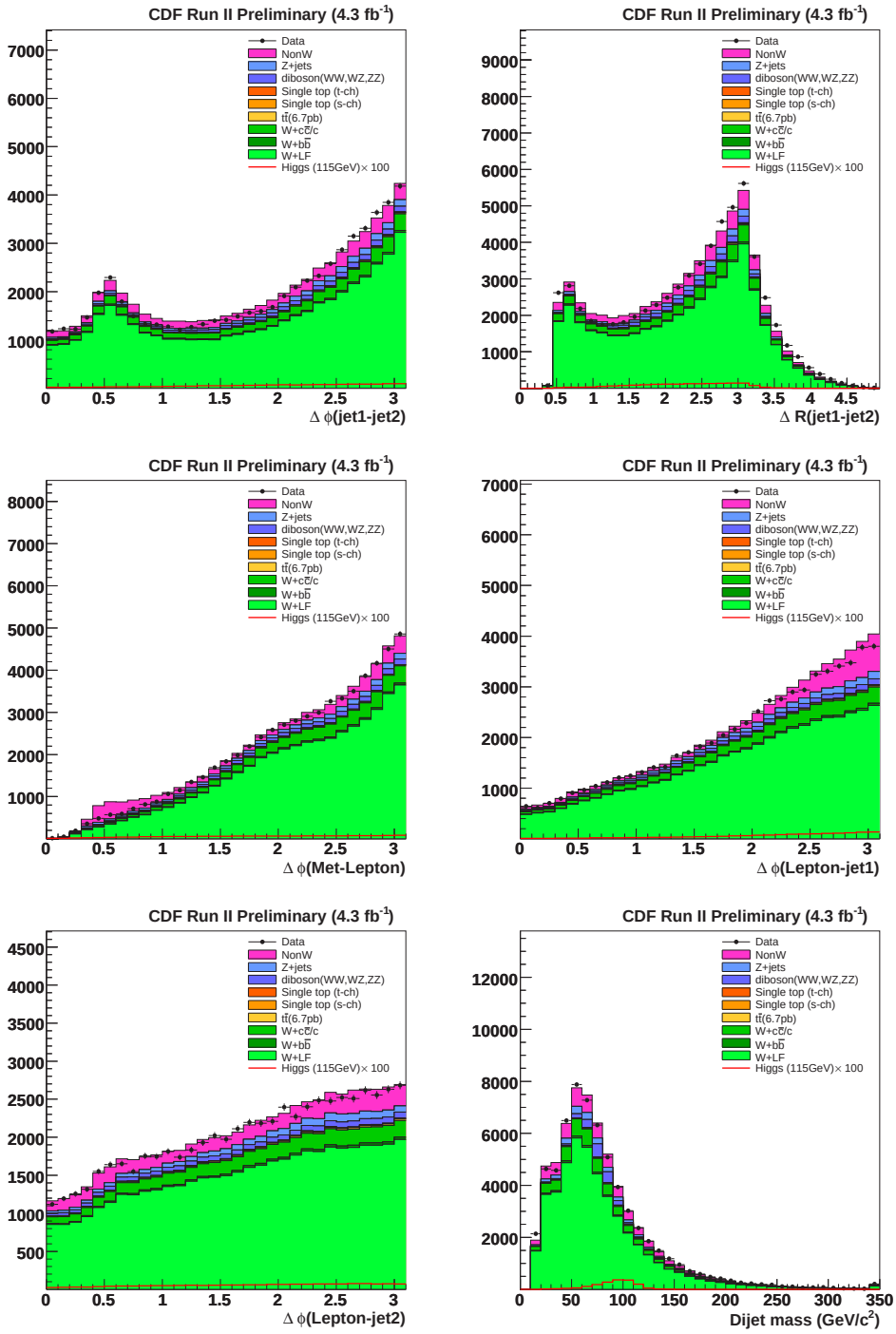

Figure B.3: Central lepton pretag basic kinematics (3)

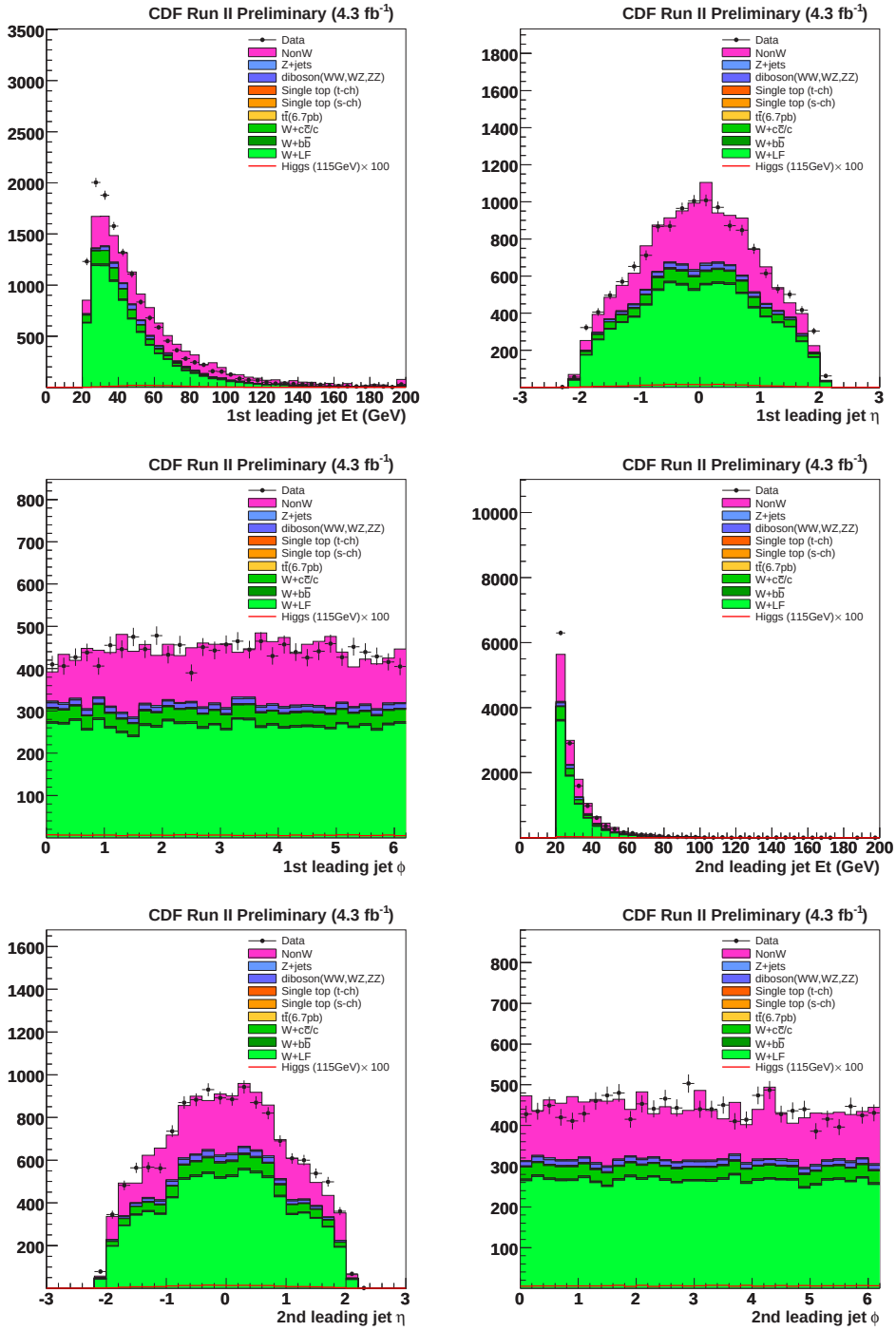

Figure B.4: Plug electron pretag basic kinematics (1)

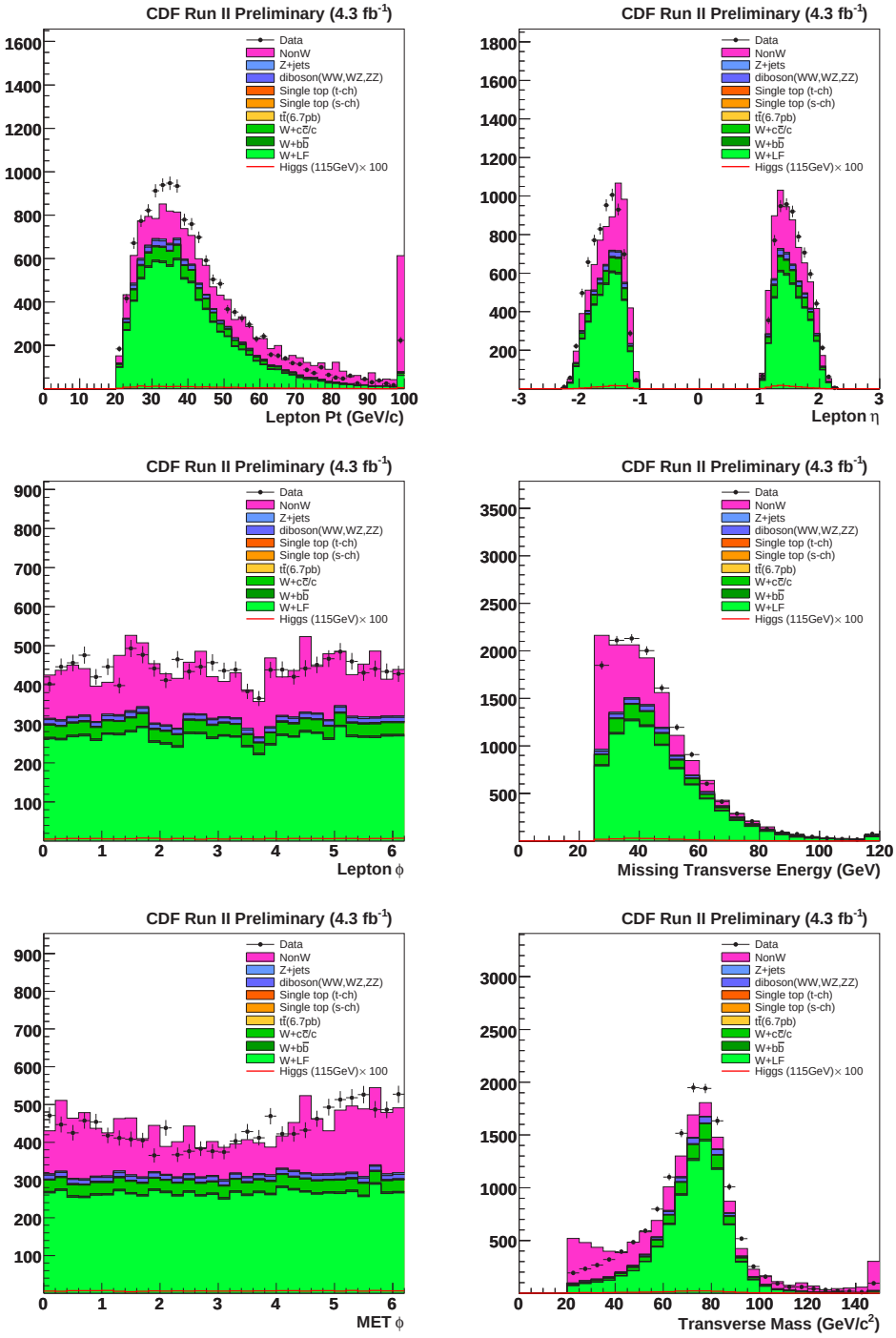

Figure B.5: Plug electron pretag basic kinematics (2)

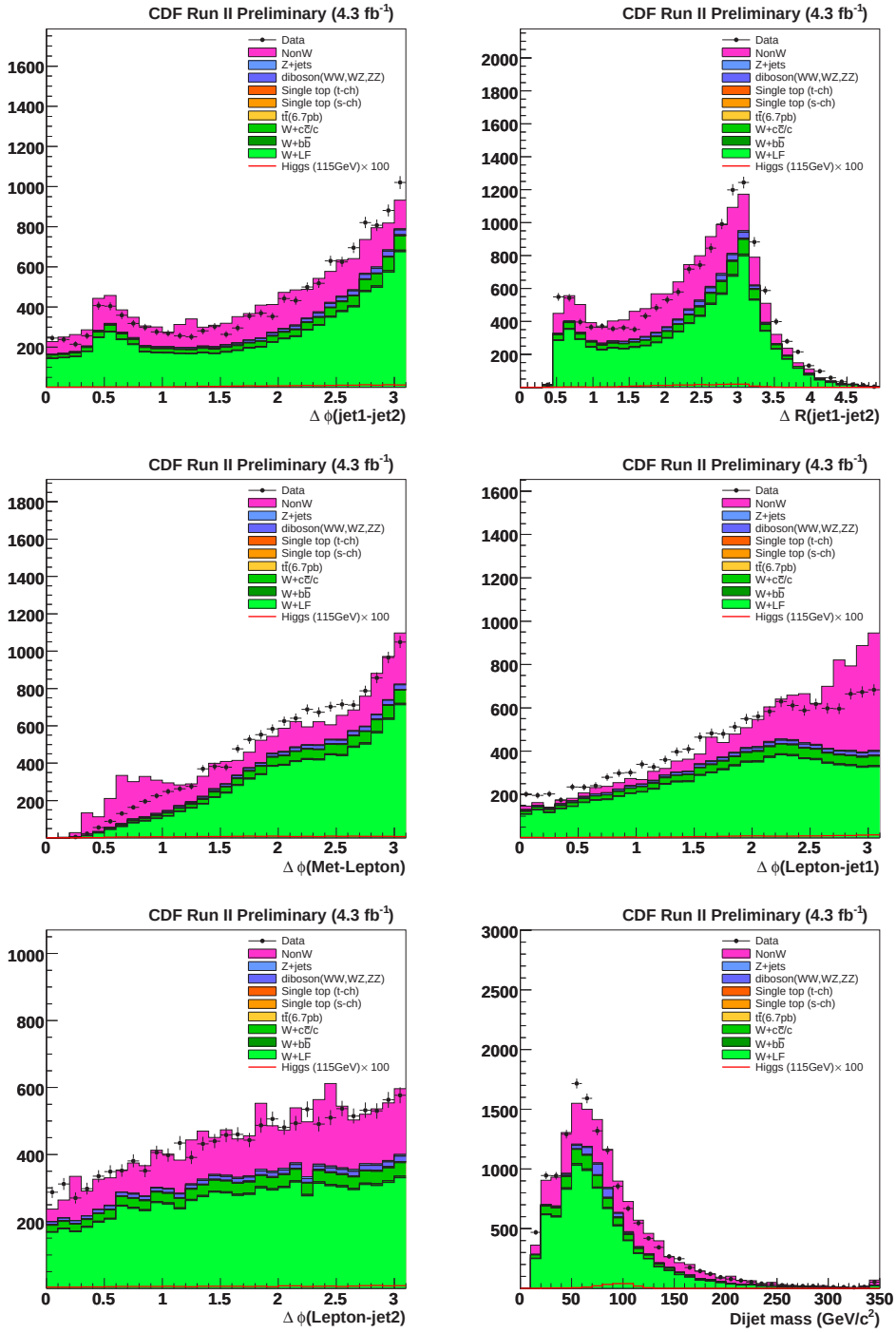

Figure B.6: Plug electron pretag basic kinematics (3)

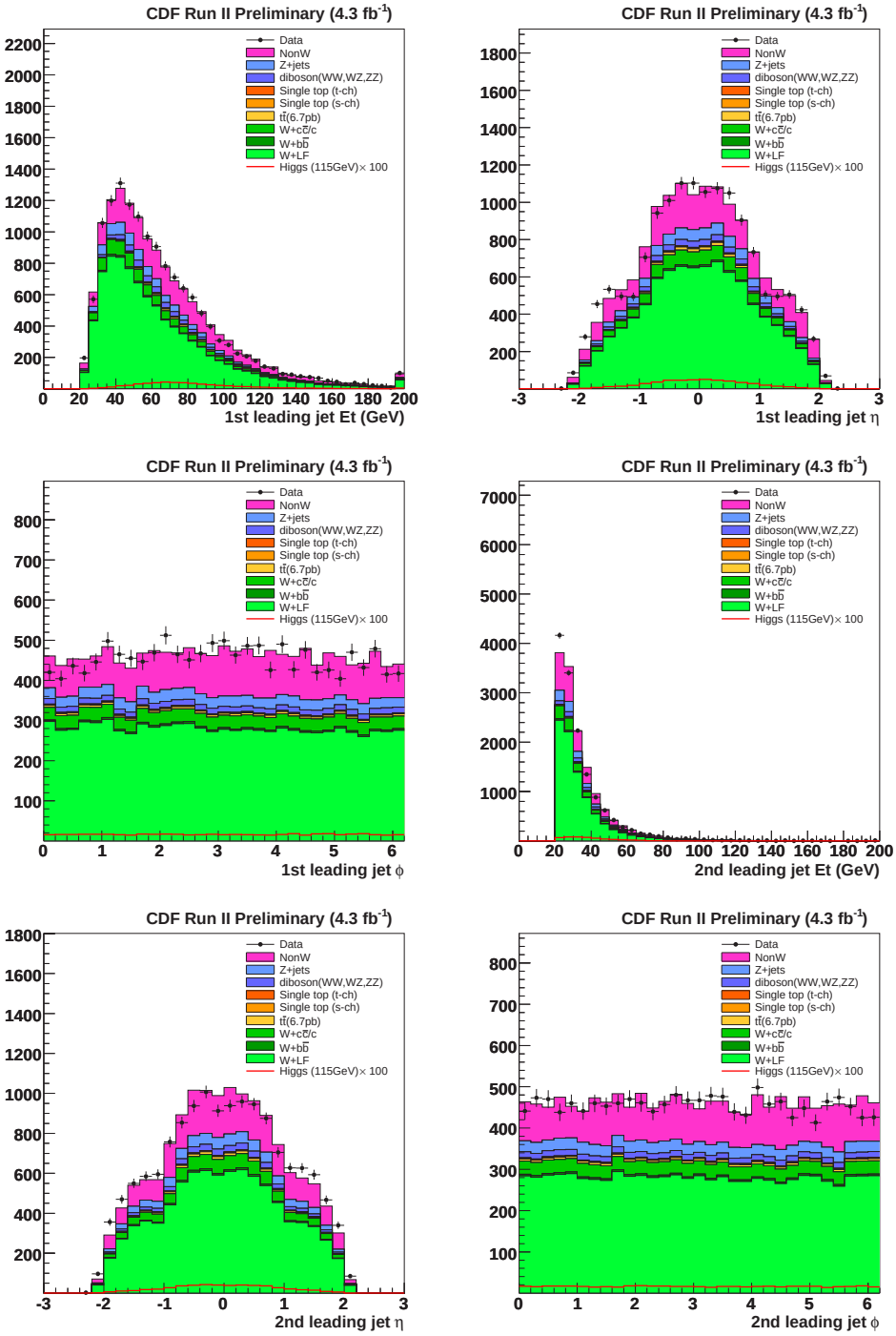

Figure B.7: Isolated track pretag basic kinematics (1)

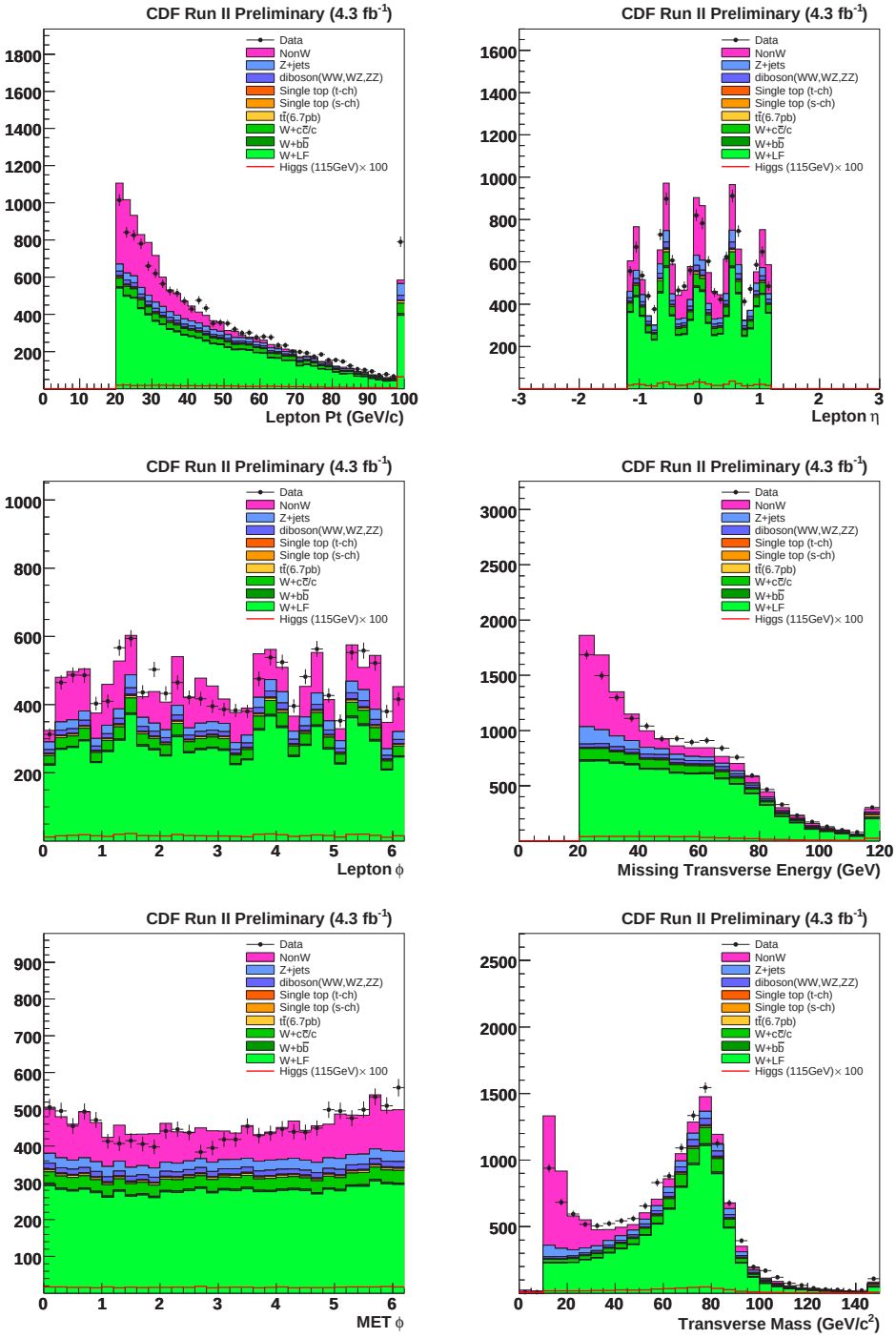

Figure B.8: Isolated track pretag basic kinematics (2)

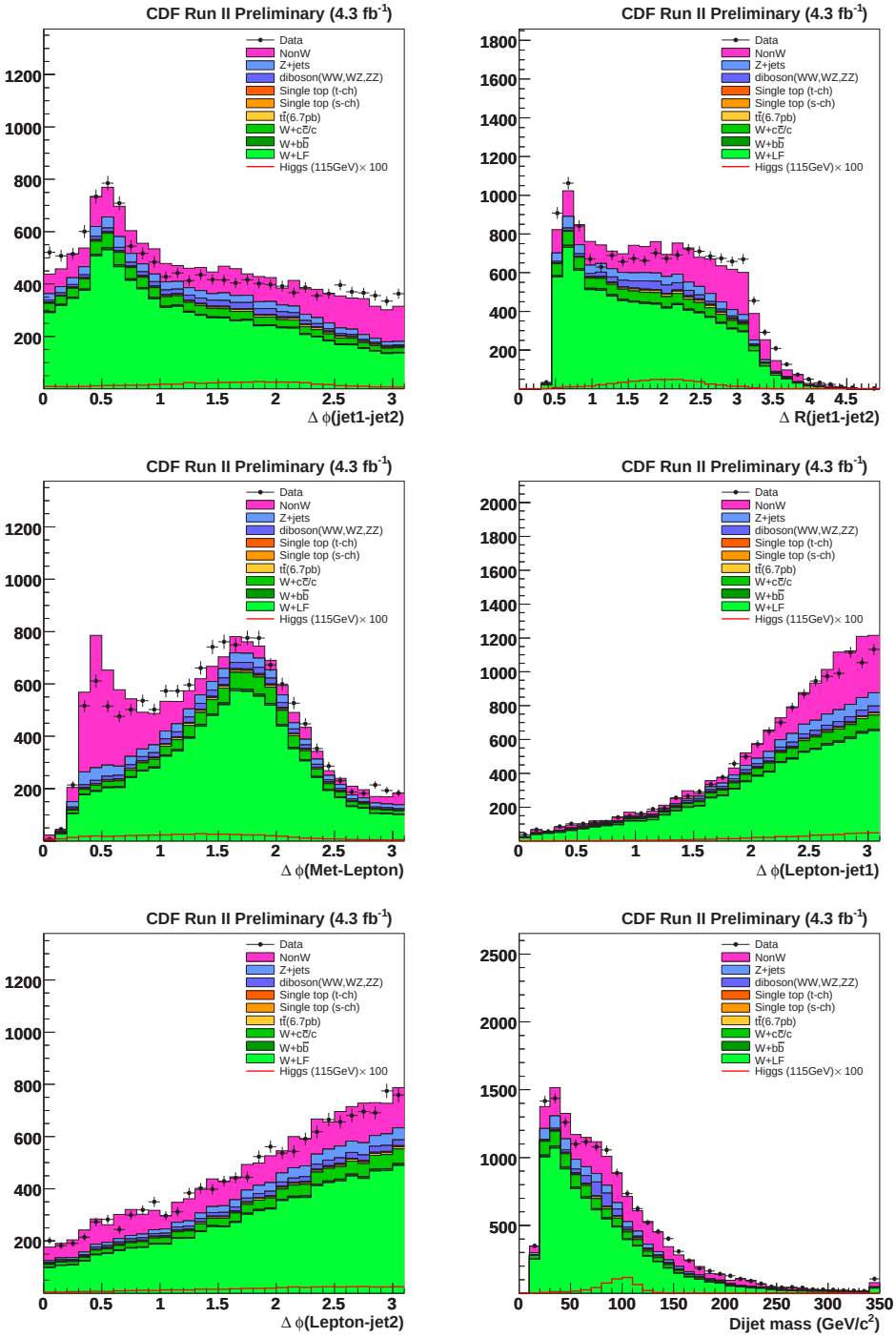

Figure B.9: Isolated track pretag basic kinematics (3)

Bibliography

[1] M. Gell-Mann, Phys. Lett. **8**, 214 (1964).

[2] G. Altarelli, Phys. Rept. **81**, 1 (1982).

[3] S. L. Glashow, Nucl. Phys. **22**, 579 (1961).

[4] A. Salam and J. C. Ward, Phys. Lett. **13**, 168 (1964).

[5] S. Weinberg, Phys. Rev. Lett. **19**, 1264 (1967).

[6] N. Cabibbo, Phys. Rev. Lett. **10**, 531 (1963).

[7] M. Kobayashi and T. Maskawa, Prog. Theor. Phys. **49**, 652 (1973).

[8] P. W. Higgs, Phys. Lett. **12**, 132 (1964).

[9] P. W. Higgs, Phys. Rev. Lett. **13**, 508 (1964).

[10] A. Djouadi, J. Kalinowski, and M. Spira, Comput. Phys. Commun. **108**, 56 (1998), arXiv:hep-ph/9704448.

[11] LEP Working Group for Higgs boson searches, R. Barate *et al.*, Phys. Lett. **B565**, 61 (2003), arXiv:hep-ex/0306033.

[12] CDF, T. Aaltonen *et al.*, Phys. Rev. Lett. **103**, 101802 (2009), arXiv:0906.5613.

[13] D0, V. M. Abazov *et al.*, Phys. Rev. Lett. **102**, 051803 (2009), arXiv:0808.1970.

[14] CDF, T. Aaltonen *et al.*, Phys. Rev. **D80**, 071101 (2009), arXiv:0908.3534.

[15] D0, V. M. Abazov *et al.*, Phys. Lett. **B655**, 209 (2007), arXiv:0704.2000.

[16] CDF, T. Aaltonen *et al.*, Phys. Rev. Lett. **100**, 211801 (2008), arXiv:0802.0432.

[17] D0, V. M. Abazov *et al.*, Phys. Rev. Lett. **101**, 251802 (2008), arXiv:0808.1266.

[18] CDF, T. Aaltonen *et al.*, Phys. Rev. Lett. **103**, 221801 (2009), arXiv:0907.0810.

[19] CDF, T. Aaltonen *et al.*, CDF Public Note **9248** (2008).

[20] D0, V. M. Abazov *et al.*, Phys. Rev. Lett. **102**, 251801 (2009), arXiv:0903.4800.

[21] D0, V. M. Abazov *et al.*, Phys. Rev. Lett. **102**, 231801 (2009), arXiv:0901.1887.

[22] CDF, T. Aaltonen *et al.*, Phys. Rev. Lett. **102**, 021802 (2009), arXiv:0809.3930.

[23] D0, V. M. Abazov *et al.*, Phys. Rev. Lett. **96**, 011801 (2006), arXiv:hep-ex/0508054.

[24] CDF, T. Aaltonen *et al.*, CDF Public Note **7307** (2009).

[25] D0, V. M. Abazov *et al.*, Phys. Rev. Lett. **97**, 151804 (2006), arXiv:hep-ex/0607032.

[26] The LEP Electroweak Working Group, http://lepewwg.web.cern.ch/LEPEWWG/.

[27] Tevatron Electroweak Working Group, (2009), arXiv:0903.2503.

[28] Tevatron Electroweak Working Group, (2009), arXiv:0908.1374.

[29] E. W. J. Cockroft, Proc. of the Royal Soc. of London **A137**, 229 (1932).

[30] J. Marriner, Nucl. Instrum. Meth. **A532**, 11 (2004), arXiv:physics/0308044.

[31] S. Nagaitsev *et al.*, Phys. Rev. Lett. **96**, 044801 (2006).

[32] On behalf of the CDF, C. S. Hill, Nucl. Instrum. Meth. **A530**, 1 (2004).

[33] CDF, A. Sill, Nucl. Instrum. Meth. **A447**, 1 (2000).

[34] CDF, A. A. Affolder *et al.*, Nucl. Instrum. Meth. **A453**, 84 (2000).

[35] CDF, A. A. Affolder *et al.*, Nucl. Instrum. Meth. **A526**, 249 (2004).

[36] CDF-II, D. Acosta *et al.*, Nucl. Instrum. Meth. **A518**, 605 (2004).

[37] CDF, L. Balka *et al.*, Nucl. Instrum. Meth. **A267**, 272 (1988).

[38] CDF, M. G. Albrow *et al.*, Nucl. Instrum. Meth. **A480**, 524 (2002).

[39] G. Apollinari, K. Goulianos, P. Melese, and M. Lindgren, Nucl. Instrum. Meth. **A412**, 515 (1998).

[40] CDF, S. Bertolucci *et al.*, Nucl. Instrum. Meth. **A267**, 301 (1988).

[41] G. Ascoli *et al.*, Nucl. Instrum. Meth. **A268**, 33 (1988).

[42] D. Acosta *et al.*, Nucl. Instrum. Meth. **A494**, 57 (2002).

[43] E. J. Thomson *et al.*, IEEE Trans. Nucl. Sci. **49**, 1063 (2002).

[44] CDF-II, B. Ashmanskas *et al.*, Nucl. Instrum. Meth. **A518**, 532 (2004), arXiv:physics/0306169.

[45] CDF, D. E. Acosta *et al.*, Phys. Rev. **D71**, 052003 (2005), arXiv:hep-ex/0410041.

[46] CDF, A. Abulencia *et al.*, J. Phys. **G34**, 2457 (2007), arXiv:hep-ex/0508029.

[47] CDF, T. Aaltonen *et al.*, Phys. Rev. **D79**, 112007 (2009), arXiv:0903.5263.

[48] CDF, F. Abe *et al.*, Phys. Rev. **D45**, 1448 (1992).

[49] A. Bhatti *et al.*, Nucl. Instrum. Meth. **A566**, 375 (2006), arXiv:hep-ex/0510047.

[50] CDF, A. Abulencia *et al.*, Phys. Rev. **D74**, 072006 (2006), arXiv:hep-ex/0607035.

[51] CDF, D. E. Acosta *et al.,* Phys. Rev. **D72**, 032002 (2005), arXiv:hep-ex/0506001.

[52] M. Feindt and U. Kerzel, Nucl. Instrum. Meth. **A559**, 190 (2006).

[53] J. Marriner, CDF Public Note **1996** (1993).

[54] http://root.cern.ch/root/html/TMultiLayerPerceptron.html.

[55] T. Sjostrand *et al.,* Comput. Phys. Commun. **135**, 238 (2001), arXiv:hep-ph/0010017.

[56] F. Maltoni and T. Stelzer, JHEP **02**, 027 (2003), arXiv:hep-ph/0208156.

[57] M. L. Mangano, M. Moretti, F. Piccinini, R. Pittau, and A. D. Polosa, JHEP **07**, 001 (2003), arXiv:hep-ph/0206293.

[58] R. M. Neal, http://www.cs.toronto.edu/%7Eradford/fbm.software.html .

[59] R. M. Neal, *Bayesian Learning for Neural Networks* (Springer, 1996).

[60] J. Pumplin *et al.,* JHEP **07**, 012 (2002), arXiv:hep-ph/0201195.

[61] S. Kretzer, H. L. Lai, F. I. Olness, and W. K. Tung, Phys. Rev. **D69**, 114005 (2004), arXiv:hep-ph/0307022.

[62] A. D. Martin, R. G. Roberts, W. J. Stirling, and R. S. Thorne, Eur. Phys. J. **C39**, 155 (2005), arXiv:hep-ph/0411040.

[63] CDF, CDF Note **9999** (2009).

[64] The CDF Collaboration, the D0 Collaboration, the Tevatron New Physics, Higgs Working Group, (2009), arXiv:0911.3930.

[65] The CDF, T. Aaltonen *et al.,* (2009), arXiv:0912.2059.

[66] K. Lane and S. Mrenna, Phys. Rev. **D67**, 115011 (2003), arXiv:hep-ph/0210299.

[67] S. Weinberg, Phys. Rev. **D19**, 1277 (1979).

[68] L. Susskind, Phys. Rev. **D20**, 2619 (1979).

[69] C. T. Hill and E. H. Simmons, Phys. Rept. **381**, 235 (2003), arXiv:hep-ph/0203079.

[70] CDF, A. A. Affolder *et al.,* Phys. Rev. Lett. **84**, 1110 (2000).

[71] D0, V. M. Abazov *et al.,* Phys. Rev. Lett. **98**, 221801 (2007), arXiv:hep-ex/0612013.

[72] CDF, T. Aaltonen *et al.,* Phys. Rev. **D80**, 012002 (2009), arXiv:0905.3155.

[73] DELPHI, J. Abdallah *et al.,* Eur. Phys. J. **C22**, 17 (2001), arXiv:hep-ex/0110056.

[74] CDF, T. Aaltonen *et al.,* Phys. Rev. Lett. **100**, 041801 (2008), arXiv:0710.4363.

[75] CDF, T. Aaltonen *et al.,* Phys. Rev. **D78**, 032008 (2008), arXiv:0803.3493.

[76] M. Cacciari, S. Frixione, M. L. Mangano, P. Nason, and G. Ridolfi, JHEP **04**, 068 (2004), arXiv:hep-ph/0303085.

[77] B. W. Harris, E. Laenen, L. Phaf, Z. Sullivan, and S. Weinzierl, Phys. Rev. **D66**, 054024 (2002), arXiv:hep-ph/0207055.

[78] J. M. Campbell and R. K. Ellis, Phys. Rev. **D60**, 113006 (1999), arXiv:hep-ph/9905386.

[79] CDF, A. Abulencia *et al.*, Phys. Rev. **D75**, 092004 (2007).